3-6-2018

Fabrication and Analysis of Multifunctional Carbon Nanotube Electrical Conductors

Andrew Robert Bucossi
arb8102@rit.edu

Recommended Citation

Bucossi, Andrew Robert, "Fabrication and Analysis of Multifunctional Carbon Nanotube Electrical Conductors" (2018). Thesis. Rochester Institute of Technology. Accessed from

R·I·T

Fabrication and Analysis of Multifunctional Carbon Nanotube Electrical Conductors

by

Andrew Robert Bucossi

A dissertation submitted in partial fulfillment of the requirements
for the degree of Doctorate of Philosophy in Microsystems Engineering

Microsystems Engineering Program
Kate Gleason College of Engineering

Rochester Institute of Technology
Rochester, New York
March 6th, 2018

Fabrication and Analysis of Multifunctional Carbon Nanotube Conductors
by
Andrew Robert Bucossi

Committee Approval:

We, the undersigned committee members, certify that we have advised and/or supervised the candidate on the work described in this dissertation. We further certify that we have reviewed the dissertation manuscript and approve it in partial fulfillment of the requirements of the degree of Doctor of Philosophy in Microsystems Engineering.

Dr. Brian J. Landi Date
Associate Professor, Chemical Engineering

Dr. Stefan F. Preble Date
Associate Professor, Microsystems Engineering

Dr. Reginald E. Rogers Date
Assistant Professor, Chemical Engineering

Dr. Steven J. Weinstein Date
Professor and Department Head, Chemical Engineering

Certified by:

Dr. Bruce Smith Date
Director, Microsystems Engineering Program

Dr. Doreen D. Edwards Date
Dean, Kate Gleason College of Engineering

ABSTRACT

Kate Gleason College of Engineering
Rochester Institute of Technology

Degree: Doctor of Philosophy **Program**: Microsystems Engineering

Authors Name: Andrew R. Bucossi

Advisors Name: Brian J. Landi

Dissertation Title: Fabrication and Analysis of Multifunctional Carbon Nanotube Conductors

Carbon nanotube (CNT) bulk conductors have been proposed as an alternative material to metals for power and data transmission applications due to their light weight, flexure tolerance, and chemical stability. However, current fabrication technologies prevent bulk CNT wires from matching the electrical properties of individual CNTs, providing opportunity for researchers to improve CNT wire fabrication.

In this work, CNT conductors have been advanced using high-purity laser-vaporized single wall carbon nanotubes (SWCNTs). Acid dispersion and extrusion of SWCNTs into a coagulant bath was used to fabricate wires and systematic modification of the process has determined that coagulation dynamics govern the resulting wire properties. Extrusion of highly aligned and dense, acid-doped SWCNT wires yielded wires with record-setting electrical conductivities of 5.1 MS/m. An extrusion apparatus has been designed and built to scale up the fabrication process and has reduced variability in wire conductivity from 30% to 6% for samples 10's of meters long. The high-current behavior of extruded SWCNT wires and commercially available CNT yarns has been investigated in a variety of ambient conditions. Comparison of electrical testing scenarios has determined that voltage-controlled testing is the proper method of characterizing CNT wires at high currents. Maximum current densities of 420 MA/m2 for extruded SWCNT wires were reached in helium, 10x greater than that reached in helium by commercial CNT yarns and exceeding fuse-law behavior for aluminum wires of equivalent diameter.

Further work to enhance CNT electrical conductivity was conducted using IBr chemical doping. Electrical enhancement of commercial CNT sheets and dopant adsorption were correlated and determined to be solvent dependent. A mechanism is proposed where low-dipole moment solvent systems favor the IBr-CNT interaction over the IBr-solvent and the solvent-CNT interactions. The optimal IBr doping conditions from the work were applied to commercial CNT yarns leading to an improvement in conductivity of 13.4x to a value of 1.4 MS/m. High voltage testing in air shows a 36% increase in maximum current, compared to as-received commercial CNT yarns. This dissertation research demonstrates the importance of SWCNT purity and selection of coagulation conditions to promote high-density, aligned SWCNT wires. Delivery of chemical dopants with high electrochemical potential through solvents which favor dopant-CNT interactions enhances electrical conductivity and maximum current density, achieving CNT wires capable of competing with metal conductors for electrical transmission applications.

ACKNOWLEDGMENTS

There are many people who have helped me become the researcher I am today. I will do my best to acknowledge as many of you as I can, but my apologies go to those I've missed in naming here. Know that I am thankful for your support.

I would like to thank Dr. Brian Landi, without his guidance this work would not have been possible. Brian has believed in me when others in his position would not, and my gratitude for this cannot be understated. My abilities as a scientist and engineer have grown a tremendous amount thanks to his guidance.

I would like to thank my committee: Dr. Stefan Preble, Dr. Reginald Rogers, and Dr. Steven Weinstein, and the Microsystems Engineering Department Head, Dr. Bruce Smith. I would specifically like to acknowledge Reggie for his guidance and friendship from my first day at RIT. Dr. Robert Parody and Dr. Cory Cress have also been great teachers and have aided in the development of this work. Thanks is also owed to the many professors and teachers that I have had at RIT, Boston University, Lehigh, and New Providence for all they have taught and dedicated to me.

I would like to thank my entire family, including my parents, my grandparents, my sisters and their families, all my aunts and uncles and cousins, and my friends Jake, Julia, Brittany, John, Rob, Steve, Dan, and my incredible girlfriend Erin for their love, support, and understanding. It has been invaluable and has motivated me my whole way here. I cannot express how lucky or how grateful I am to have such family and friends.

I would like to thank all my co-workers and fellow students at RIT, in no particular order, who have all become great friends: Jim Smith, Elaine Lewis, Stephanie Hart, Lisa Zimmerman, Ivan Puchades, Jason Staub, Jamie Rossi, Martin Dann, Dylan McIntyre, Anthony Leggiero, Nathanael Cox, Chris Schauerman, Matt Ganter, Kyle Crompton, Karen Soule, Alex Tomkiewicz, Paul Thomas, Aaron Rape, Andrew Merrill, Steven Polly, Elisabeth McClure, Cory Cress, Mohad Baboli, Nicholas Conn, Ankit Kalani, and Masoud Golshadi. You have all directly aided me in my education and research. Thanks to you, I have learned more than I ever could have imagined and you have made my time at RIT a pleasure.

I would like to specifically acknowledge Dr. Christopher Schauerman, Jamie Rossi, Dr. Nate Cox, Dr. Steven Polly, Dr. Ivan Puchades, and Dr. Matthew Ganter who have been outstanding researchers, role-models, and friends, and who have inspired me with their kindness, intelligence, and dedication. Extra thanks are due to Chris for his instruction and friendship from the very beginning of my time at RIT.

I would like to thank all the students I have worked with, especially Anthony Sammarco, Colleen Lawlor, Quintina Frink, Nick Schaake, Michael Hladky, and Gavin Lewis. You kept me on my toes and working with you has been one of my favorite parts and greatest privileges of working in this lab. I wish you the best in your endeavors and can't wait to see your future accomplishments.

Table of Contents

Table of Contents v
List of Figures viii
Chapter 1. Introduction...1
1.1 Carbon Nanotube Fundamentals...1
1.2 Carbon Nanotube Network Conduction...5
1.3 Carbon Nanotube Wire Fabrication 8
1.4 Research Opportunities and Dissertation Objectives.........................20
Chapter 2. Characterization of Carbon Nanotube Wires.......................................22
2.1 Measurements on CNT Wires...22
2.1.1 Resistance...22
2.1.2 Length..23
2.1.3 Cross Section...23
2.1.4 Mass 24
2.1.5 Breaking Force 24
2.2 Standard Material Metrics..25
2.2.1 Electrical Conductivity..25
2.2.2 Specific Conductivity..26
2.2.3 Tensile Strength...27
2.3 Carbon Nanotube Characterization Techniques 27
2.3.1 Thermogravimetric Analysis (TGA).................................27
2.3.2 Raman Spectroscopy..28
2.3.3 Purity Assessment 30
Chapter 3. Extrusion of Laser Vaporized Single Wall Carbon Nanotubes...............32
3.1 Laser Vaporization and Purification of Single Wall Carbon Nanotubes 33
3.1.1 Synthesis of Laser Vaporized SWCNT Materials...............33
3.1.2 Purification of SWCNT Materials......................................34
3.2 Influence of Impurity Presence in Extruded Laser SWCNT Wires...................35
3.3 Coagulation in Various Solvents 40
3.3.1 Single-Solvent Approach 40
3.3.2 Design of Experiments Approach 46
3.4 Mechanical Tension Processing...49
3.4.1 Strain Induced During Wire Coagulation..........................50

3.4.2 Post-Extrusion Wire Straining 52
3.5 Extruded Laser-Vaporized SWCNT Wire Conclusions 54
Chapter 4. Engineering Factors Influencing Extruded Wire Fabrication 56
4.1 Introduction to Additional Factors Available 56
4.2 Carbon Nanotube Types for Extruded Wires....................58
4.2.1 Commercially-Sourced Carbon Nanotube Materials 58
4.2.2 Modified Laser Synthesis Parameters 64
4.3 Extrusion Process Factors Influencing Dispersion Coagulation....................70
4.4 Extrusion of SWCNT Wires using Best-Practices....................85
4.5 Extrusion Automation and Apparatus Construction 89
4.6 Extruded Wire Fabrication Conclusions....................93
Chapter 5. High-Current Behavior of Carbon Nanotube Yarns and Wires....................95
5.1 Introduction to High Current Conditions....................95
5.2 Current Carrying Capacity Test Conditions 97
5.3 Ambient Gas Dependence of CNT Yarn and SWCNT Wire Failure 104
5.4 High-Current Wire and Yarn Conclusions 119
Chapter 6. Doping of Carbon Nanotube Wires for Enhanced Conductivity 121
6.1 Chapter Abstract 121
6.2 Introduction to Chemical Doping of CNTs 122
6.3 Experimental....................124
6.3.1 Doping Solution and CNT Preparation 124
6.3.2 Electrical Conductivity and Optical Absorption Characterization....................125
6.3.3 IBr Time-Dependent Conductivity Study 127
6.3.4 Tensile and High-Current Characterization of CNT Yarns 128
6.4 Results of IBr Doping Studies 128
6.5 Additional Considerations for the Study of IBr Doping....................142
6.6 IBr Doping Conclusions 147
Chapter 7. Influence of Purification and Doping in Radial Densification of CNT Sheet Material 149
7.1 Purification of Commercially Sourced CNT Sheet Material....................149
7.2 Influence of Purity on Electrical and Mechanical Properties 151
7.3 Radial Densification of Carbon Nanotube Wires 151
Chapter 8. Dissertation Conclusions and Impact 158

Appendix A: Dissertation Contribution Acknowledgments 162
Appendix B: Wire Extrusion Standard Operating Procedure 163
Bibliography 167

List of Figures

Figure 1. (left) Schematic structure of graphene. (right) The dispersion relation of graphene, reproduced from [2]. 2

Figure 3. Experimental phase diagram of volume fraction of SWCNTs in increasingly acidic solvent [47], [48]. 17

Figure 4. Review of wire and fiber properties from the literature review as of 2015. 19

Figure 5. TGA data from a sample of arc-synthesized SWCNTs....................28

Figure 6. Raman spectrum of a purified bulk laser-vaporized SWCNT paper with several features labeled. 30

Figure 7. Process diagram of factors influencing CNT wire extrusion, with the factors investigated in the chapter highlighted in red. 32

Figure 8. (a) SEM image of AP laser SWCNT material which includes carbonaceous and metal catalyst impurities. (b) SEM micrograph of laser SWCNTs after a purification procedure described in section 3.1.2....................34

Figure 9. (a) Extruded wire made from a SWCNT-CSA dispersion of AP laser SWCNT material. (b) Extruded wire made from a SWCNT-CSA dispersion of purified SWCNT material. (c) and (d) are higher magnification images of the surfaces of the wires in (a) and (b) respectively. 40

Figure 10. SEM images of wires extruded from purified laser SWCNT dispersions into (a) acetone, (b) acetonitrile, (c) N,N-dimethylacetamide, (d) chloroform, (e) dimethyl sulfoxide, and (f) ethanol. Insets are higher magnification of each wire....................43

Figure 11. Properties of SWCNT wires extruded into various composition coagulant baths analyzed by (a) specific conductivity and specific tensile strength and (b) electrical conductivity and tensile strength. 45

Figure 12. Specific conductivity data from Figure 11 plotted vs (a) boiling point, (b) dipole moment, (c) density, (d) viscosity, (e) molar mass, and (f) surface tension. 46

Figure 13. Experimental results from conducting a combined mixture-process designed experiment which varied both mixtures of acetone, ethanol, and chloroform; and temperature. Results are listed as specific conductivity in units of S m^2 kg^{-1}. 47

Figure 14. Modeled response surface resulting from regression analysis of the experimental data in Figure 13. 49

Figure 15. Schematic of the extrusion process and the method which will be used to induce increasing degrees of tension on the coagulating SWCNT-CSA dispersion. 51

Figure 16. Specific conductivity and specific tensile strength of SWCNT wires extruded into coagulant baths of varying depths. Error bars are the standard deviation in 5 replicate samples. 52

Figure 17. (a) SEM image of wire extruded into 30 cm deep, room temperature acetone bath and then mechanically strained while drying which yielded a conductivity of 4.1-5.0×10^6 S/m. (b) Higher magnification SEM image showing the aligned nature of SWCNT bundles on the surface of the wire in (a). (c) Spool of several continuous meters of wire in (a). (d) Comparison of the electrical and mechanical properties of wires extruded from purified laser SWCNTs to other CNT wires produced from similar wet-spinning techniques used in [47], [52], [53]. 53

Figure 18. Process diagram of factors impacting extruded wire performance, with factors investigated in this chapter highlighted in blue, and factors investigated in Chapter 3 highlighted in red. 58

Figure 19. SEM images of (a) extruded wire made from purified laser SWCNT-CSA dispersion, and (b) extruded wire made from purified HiPco SWCNT-CSA dispersion under the same extrusion conditions. (c) higher magnification image of the surface of the wire in (b). 59

Figure 20. (a) Boxplot of 5 specific conductivity measurements from laser and HiPco SWCNT extruded wires. (b) Boxplot of 5 tensile strength measurements from laser and HiPco SWCNT extruded wires. (c) Representative Stress-Strain curves for HiPco and laser SWCNT extruded wires. 60

Figure 21. (a) and (b) SEM images of extruded wires made from a dispersion containing both purified laser SWCNTs and purified NCTI CNTs. (c) Specific conductivity measurements on these wires and extruded wires of only purified laser SWCNTs as a control. (d) Specific tensile strength measurements on these wires and extruded wires of only purified laser SWCNTs as a control. 61

Figure 22. Characterization of DWCNTs and DWCNT extruded wires. a. SEM image of powdered, as-purchased DWCNTs. b. SEM image of DWCNTs after 560 °C thermal oxidation, HCl treatment, a second 560 °C thermal oxidation, and a second HCl treatment. c. Multiple SEM images stitched together of an extruded wire made from purified DWCNTs. d. High-magnification SEM image of DWCNT extruded wire with the wire axis mounted vertically. e and f. Cross-sectional SEM images of two laser-cut DWCNT extruded wire segments. 63

Figure 23. a. Raman spectroscopy of products of SWCNT synthesis run at 1150 (black) and 900 °C (blue) in nitrogen (top) and 1150 (black) and 900 °C (blue) in helium (bottom). b. plot of SWCNT diameter and the conductivity of an ideal bundle of SWCNTs with that diameter (red data points). Inset diagrams demonstrate the effect of SWCNT diameter on bundle size. Blue and green bands demonstrate the diameter ranges

possible from SWCNT synthesis under nitrogen at 900-1150 °C and Argon at 1150 °C, respectively. 65

Figure 24. a, b, and c. SEM images of SWCNTs synthesized under nitrogen carrier gas at each of the labeled temperatures in a sheet format after acid refluxing. d. Derivative weight (change in mass per degree Celsius) as a function of temperature from thermogravimetric analysis of refluxed SWCNTs in sheet format synthesized under nitrogen at various temperatures. e. Raman spectroscopy of the radial breathing modes of refluxed SWCNTs in sheet format synthesized under nitrogen at various temperatures. .67

Figure 25. Characterization of wires extruded from 45 mg/mL dispersions of either purified SWCNTs synthesized under 1000 °C nitrogen or 1125 °C. a and b. Side-on SEM images with the wires mounted horizontally and with a slight twist to show all sides. c and f. High-magnification SEM images of the surfaces of both wires with the wire axis oriented vertically. d and e. Cross-sectional SEMs of laser-cut sections of each wire. 69

Figure 26. Dependence of wire specific conductivity on syringe diameter with cross-section SEMs of laser-cut samples from each extrusion. 72

Figure 27. Specific conductivity of extruded SWCNT wires while varying the extrusion rate....73

Figure 28. Characterization of wires extruded through 22 Ga syringe needles cut to various lengths. a. Resistance per length (left axis and red circle data points) and linear mass density (right axis and blue diamond data points) of wires extruded from various length syringe needles. b. specific conductivity of the same samples. d. Tensile force as a function of applied strain from 3 replicate samples extruded from each length syringe needle. 75

Figure 29. a. Photograph of a glass syringe with a 22 Ga stainless steel syringe needle inserted into 8 cm of PTFE tubing. b and c. Optical microscopy images of two replicate samples extruded using the syringe in panel a. d-g. Cross-sectional SEM images of laser-cut wire segments extruded using the syringe in panel a. 77

Figure 30. a. Schematics of the standard extrusion setup which involves a syringe needle with the tip submerged into the coagulant bath, the desired goal scenario of an air-gap extrusion in which the syringe needle is elevated above the surface of the coagulant bath and the stream of extruded dispersion uniformly thins before entering the coagulant bath, and the observed air-gap scenario in which droplets form in the air gap and prevent the resulting wire from having a high degree of uniformity. b. optical microscopy images of a wire extruded with a submerged syringe needle (left) and of a wire extruded with a dehumidified air-gap (right). c. Specific conductivities of wires extruded using the standard setup (blue circle data points) and with a dehumidified air-gap (red square data points) as a function of their linear mass density....79

Figure 31. a. Schematic of the opening of a coaxial syringe needle. b. Specific conductivity (left axis and red circle data points) and conductivity (right axis and green square data points) of wires extruded using a 18/22 Ga coaxial syringe needle with various rates of coagulant flow through the outer (18 Ga) syringe opening. 81

Figure 32. Characterization of wires extruded using coaxial syringes. a. Optical microscopy images of two replicate wire segments extruded from the 14/18 Ga coaxial syringe needle. b. Optical microscopy images of two replicate wire segments extruded from the 18/22 Ga coaxial syringe needle. c. Cross-sectional SEM of a wire extruded through the 14/18 Ga coaxial syringe needle. d. Cross-sectional SEM of a wire extruded through the 18/22 Ga coaxial syringe needle...83

Figure 33. Specific conductivities of extruded SWCNT wires extruded into acetone baths of various temperatures..85

Figure 34. Characterization of wires extruded into a -10 °C, 66 cm deep acetone bath from a 61 mg/mL weight loading dispersion. a. Optical microscopy image. b and c. Side-on SEM images of the wire, with the wire axis oriented vertically. d-g. Cross-sectional SEM images of wire segments cut with a laser cutter. h. Side-on SEM image of a wire mounted with a slight twist. Width and thickness measurements are superimposed. 87

Figure 35. a. and b. SEM images of two replicate segments of extruded SWCNT wires that were calendered and then laser-cut...89

Figure 36. The extrusion apparatus and characterization of wires produced using it. a. Photograph of the extrusion apparatus. b. Close-up photograph of the coagulant bath in the extrusion apparatus, in which the submerged syringe and extruded wire can be seen on the left, and the two PTFE spools can be seen on the right. The first (leftmost) PTFE spool has extruded wire winding around it. c. Photograph of the extrusion apparatus control panel, which at this time consists of two potentiometers and two numeric display panels. d. The Arduino Uno R3 and wiring which connects and controls the components of the control panel and the spooling motors. e and f. Optical microscopy images of two replicate wire segments extruded from the extrusion apparatus. g-j. Four replicate cross-sectional SEMs of laser-cut wire segments produced using the extrusion apparatus........92

Figure 37. Photograph of 4 electrical probes mounted inside the glass cylinder test chamber...98

Figure 38. a. Comparision of the current-voltage characteristics of two different lots of yarn with 3 replicates from lot 60027 and two replicates from lot 60025, all tested under nitrogen flowing at 0.5 SCFH with voltage increases of 150 mV every 5 sec. b. Plot of max current (left axis, black circle datapoints) and the voltage at which maximum current was reached (right axis, red square datapoints) of nine samples of CNT yarn lot 60027 for three different flow rates of air in the test fixtrure. c. Measured current as a function of

applied voltage for three segments of CNT yarn lot 60027 under 0.5 SCFH of nitrogen with the applied voltage increasing by 100 mV every 60, 30, or 15 seconds.................101

Figure 39. a. Measured current as a function of applied voltage of six CNT yarns with either a current-controlled test with 5 mA increases every thirty seconds or a voltage controlled test with 110 mV increases every 30 seconds. b. The measured current of the samples from panel a, plotted as a function of the test time. c. The applied voltage on the samples from panel a, plotted as a function of test time. d. Measured tensile force as a function of applied strain for CNT yarns with either a force-controlled test where force in increased by 0.233 N/min or a strain-controlled test where strain is increased by 0.2 %/min. e. The measured tensile force from both samples in panel d, as a function of test time. f. The applied strain from both samples in panel d, as a function of test time. 104

Figure 40. Measured current as a function of the applied voltage on nine CNT yarn samples in 0.5 SCFH of the specified ambient gas..106

Figure 41. Cross-sectional SEM images of both sides of 4 laser-cut CNT yarn lot 60027 samples and the accompanying area measurements recorded from each image. 107

Figure 42. Optical microscopy images of CNT yarns after failure. a. ~7 mm from failure point in air. b. Failure point in air. c. ~0.5 mm from failure point in air, same scale bar as panel a. d. Failure point in nitrogen. e. Failure point in helium. 108

Figure 43. Top Row: SEM images of high-current failure point of a CNT yarn in: a. Air, b. Nitrogen. c. Helium. Bottom Row: SEM image of CNT yarn approximately 1 mm from high-current failure point in: d. Air, e. Nitrogen, f. Helium. 110

Figure 44. Measured current as a function of applied voltage for three segments of extruded SWCNT wire under three different ambient gasses. 112

Figure 45. Instantaneous resistance (applied voltage divided by measured current) calculated from the data in Figure 44 as a function of the applied voltage. 114

Figure 46. a. Applied voltage plotted as a function of the instantaneous resistance of extruded SWCNT wires tested in different ambient gases derived from the data in Figure 44 and Figure 45, which derive from a voltage-controlled test. b. Plot of current density as a function of relative resistance change of an extruded CNT yarn in vacuum from current-controlled testing in which repeated cycles of current were applied with each cycle reaching a new maximum value, adapted from [83]. 115

Figure 47. Top Row: SEM images of high-current failure point of extruded SWCNT wires in: a. Air, b. Nitrogen. c. Helium. Bottom Row: SEM images of extruded SWCNT wires <80 µm from their high-current failure point in: d. Air, e. Nitrogen, f. Helium....117

Figure 48. Raman D/G ratios as a function of distance from the high-current failure point. a. measured on a CNT yarn brought to high-current failure in air. b. Measured on

extruded SWCNT wires brought to failure in air (red circle data points) and in nitrogen (green square data points). 119

Figure 49. Schematic of optical absorbance spectroscopy experimental set up, where a solid CNT sample is present in the dopant solution within the cuvette. $\Delta\boldsymbol{A}$ is the change in optical absorbance at a given wavelength between a control doping solution sample and a doping solution sample with CNTs present at a given time after solution preparation , and $\Delta\boldsymbol{C}$ is the change in doping solution concentration between its as-prepared concentration and its concentration at a given time...127

Figure 50. (a.) Conductivity of CNT samples doped with 5 mM I_2 in ethanol and hexanes for 60 min. Inset shows an example of a purified CNT sample (7 mm square) used in all following studies. (b.) Optical absorbance spectra of I_2 in ethanol at specified times after introducing a CNT sample into the cuvette. Inset shows photograph of 1 mM IBr in ethanol. (c.) Optical absorbance spectra of I_2 in hexanes at specified times after introducing a CNT sample into the cuvette. Inset shows photograph of 1 mM IBr in hexanes. (d.) Normalized absorbance intensity at peak wavelengths over time for I_2 in ethanol and hexanes after solution preparation with and without CNTs present in the cuvette. (e.) Mass of I_2 dopant absorbed per mass of CNT sample during doping in ethanol and hexane solutions. 130

Figure 51. (a.) Time-dependent doping studies using 0.2 g/L (1 mM) IBr in ethanol. (b.) Optical absorbance of 0.2 g/L (1 mM) IBr in ethanol solution (data collected every 10 minutes but shown every 20 minutes for clarity) after introducing a CNT sample into the cuvette. Inset shows photograph of the 0.2 g/L (1 mM) IBr in ethanol solution. (c.) Optical absorbance values at 390 nm for a solution of 0.2 g/L (1 mM) IBr in ethanol both with (black diamond markers) and without (black circle markers) CNTs present in the cuvette over time. Optical absorbance data is normalized to absorbance at 0 min. Calculated values of the amount of IBr adsorbed onto the CNT sample are shown as blue square markers and plotted on the right y-axis over time. 134

Figure 52. (a.) Optical absorbance of IBr in hexanes solution (data collected every 10 minutes but shown every 20 minutes for clarity) after introducing a CNT sample into the cuvette. Inset shows photograph of the 0.2 g/L (1 mM) IBr in hexanes solution. (b.) Optical absorbance values at 503 nm of an IBr solution in hexanes both with (black diamond markers) and without (black circle markers) CNTs present in the cuvette over time. Optical absorbance data is normalized to absorbance at 0 min. Calculated values of the amount of IBr adsorbed onto the CNT sample are shown as blue square markers and plotted on the right y-axis over time. 135

Figure 53. (a.) Conductivity of CNT samples after exposure to 2.1 g/L (10 mM) IBr for 60 min in the specified solvent versus that solvent's dipole moment. [119] (b.) Conductivity of CNT samples doped with various solution loadings of IBr in hexanes for 60 min. 139

Figure 54. (a.) Stress-strain characteristics of CNT yarns with and without IBr solution doping. (b.) Current-voltage characteristics of CNT yarns with and without IBr solution doping. 141

Figure 55. Optical absorption spectra of a 1 mM solution of Br_2 in chloroform (red), a 1 mM solution of I_2 in chloroform (blue), a mixture of the two previous solutions mixed in equal volumes (black) and a 1 mM solution of IBr in chloroform. 143

Figure 56. a. Optical absorbance (left axis) at 279 nm of a solution of IBr in hexanes (black circle datapoints) as a function of time after mixing the solution, and of a solution of IBr in hexanes with CNTs as a function of time after solution mixture and CNT addition (black diamond data points). The amount of IBr adsorbed onto the CNTs (blue square data points, right axis) calculated from the optical absorption data in this plot and equation (7). b. Optical absorbance (left axis) at 503 nm of a solution of IBr in hexanes (black circle datapoints) as a function of time after mixing the solution, and of a solution of IBr in hexanes with CNTs as a function of time after solution mixture and CNT addition (black diamond data points). The amount of IBr adsorbed onto the CNTs (blue square data points, right axis) calculated from the optical absorption data in this plot and equation (7). 144

Figure 57. a. optical absorption spectra of 1 mM IBr solution in chloriform with CNTs present in the cuvette at several times after mixing. b. optical absorbance intensity at 503 and 256 nm, with and without CNTs in present in the cuvette as a function of time after mixing or mixing and CNT addition, normalized to the optical absorbance intensity at 0 min. c. optical absorption spectra of 1 mM IBr solution in DMSO with CNTs present in the cuvette at several times after mixing. d. Optical absorbance intensity at 414 nm of 1 mM IBr solutions with and without CNTs present in the cuvette as a function of time after mixing or mixing and CNT addition, normalized to the optical absorbance intensity at 0 min. 146

Figure 58. (left) Flow diagram of how dipole moment governs the interactions between the solvent and IBr, and the solvent and the CNTs, and how these combined interactions affect doped CNT conductivity. (right) pictoral representations of the favored interactions in the IBr-solvent-CNT system for a solvent that promoted low CNT conductivity enhancement (DMA) and a solvent which promoted high CNT conductivty (hexanes). The favored interactions are those that the arrows point to. 148

Figure 59. (a) SEM of AR NCTI CNT sheet material. (b) TGA data from oxidizing AR NCTI sheet material..150

Figure 60. (left) Cross section schematic of the radial densification of CNT wires. (right) Photo of a CNT wire being densified. [98]..152

Figure 61. (a) tensile and (b) mass-normalized tensile properties of densified NCTI CNT wires made from materials with varying treatments and doped with either $KAuBr_4$ in water or IBr in hexanes. 154

Figure 62. (a) L/R and (b) specific conductivity of densified NCTI CNT wires made from materials with varying treatments and doped with either $KAuBr_4$ in water or IBr in hexanes.....155

Figure 63. (a) Raman spectra of NCTI materials used to create the samples Figure 61 and Figure 62. (b) D/G and D/G’ ratios calculated from the spectra in (a).....156

Figure 64. Electrical conductivities of densified CNT wires which have been densified to various densities and thermally oxidized at different temperatures.....157

Chapter 1. Introduction

1.1 Carbon Nanotube Fundamentals

The term carbon nanotube (CNT) is broadly used to refer to nano- to microscale tubes of predominantly sp^2 hybridized carbon. Depending on the specific synthesis parameters, CNTs have been classified into two categories based on the number of concentric carbon layers which form the CNT. Those which can be described as a single graphene sheet rolled into a cylinder are termed single-wall carbon nanotubes (SWCNTs). Those with multiple layers – sometimes discrete and sometimes covalently bonded to each other – are called multi walled carbon nanotubes (MWCNTs).

Due to their simple structure, individual SWCNTs have been theoretically studied extensively. The basis of their electrical properties is derived from graphene sheets (Figure 1, left panel) due to their similar structure. Near the fermi level of graphene (see Figure 1, right panel), the shape of the dispersion relation takes on that of a straight-sided cone (called a Dirac-cone) and thus can be approximated linearly, in contrast to traditional direct-bandgap semiconductors whose dispersion relation can be approximated parabolically. The linear dispersion relation of graphene leads to relativistic effects in the effective motion of charge carriers due to their zero effective mass. Electrical conduction in graphene was first described theoretically by Wallace in 1946 [1].

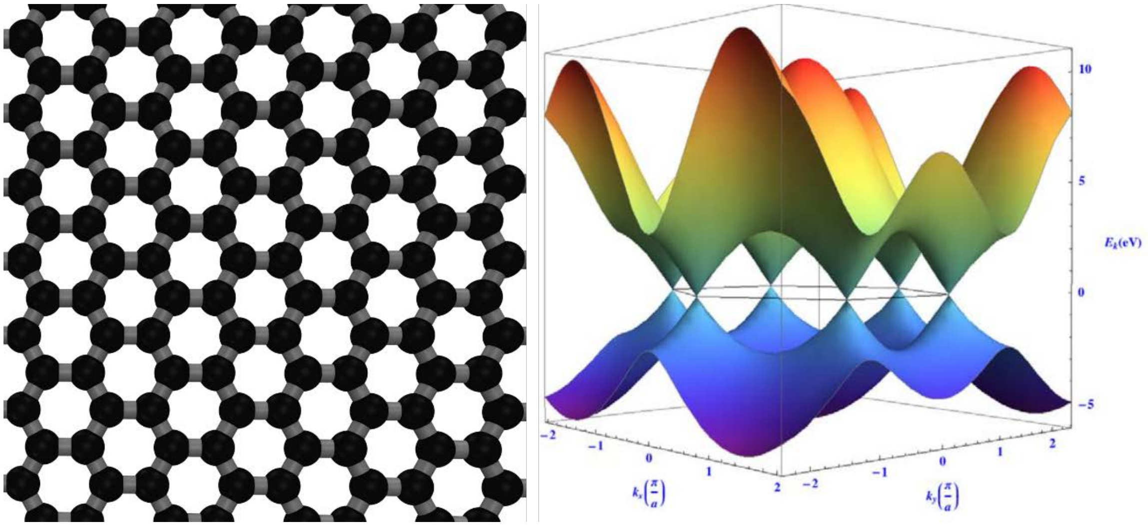

Figure 1. (left) Schematic structure of graphene. (right) The dispersion relation of graphene, reproduced from [2].

Early approximations of the electronic structure of SWCNTs relied on applying periodic boundary conditions to the structure of graphene, mimicking the circular nature of the of the SWCNT wall. This technique is referred to as the zone-folding approximation. This approximation predicts that the dispersion relation for a SWCNT will be multiple 2D ‘slices’ of that of graphene. Depending on diameter, some SWCNTs will cut the Dirac-cone through its center, and thus will have zero band gap. These SWCNTs are classified as metallic, while those with a non-zero band gap under the zone-folding approximation are classified as semiconducting. The shortcoming of the zone-folding approximation is that it does not account for the curvature in a SWCNT wall, ignoring the strain in the C-C bonds. Thus the approximation predicts the electronic energies with greater accuracy for SWCNTs with larger diameters [3]. When taking the curvature of a SWCNT into account, a bandgap inversely proportional to the square of the SWCNT diameter is found for some metallic SWCNTs and has been corroborated experimentally using scanning tunneling microscopy [4]. This observation segregates the electronic properties of SWCNTs based on their chirality, or the angle at which a graphene ribbon would be rolled to form the SWCNT. SWCNTs that maintain their zero-bandgap and are truly metallic are known as ‘armchair’ SWCNTs.

When the fermi energy of a CNT lies within the valence or conduction band, SWCNTs are predicted to have a quantized conductance of $4e^2/h$ = 150 µS (where e is the electron charge and h is planks constant) which is derived from the Landauer formula for conductance of quasi-one dimensional system [5]. This conductance should in theory be realized in armchair SWCNTs at room temperature due to their zero-bandgap nature [3]. Indeed, values close to this conductance have been measured experimentally [6] and SWCNTs with experimentally common diameters are theorized to have ballistic transport (long mean free paths) [7]. The conductance prediction of 150 µS is independent of length or diameter of a SWCNT, necessitating an assumption of the physical dimensions of a synthesized SWCNT in order to convert into a value of conductivity in S/m. The conductivity predicted for a 1 nm diameter and 1 µm long SWCNT in this manner is then 1.9×10^8 S/m, exceeding that of copper (5.9×10^7 S/m [8]), a metal commonly used for electrical transport. Other estimates for the conductivity of individual metallic SWCNTs predict a resistance of 4.2 kΩ/µm per CNT using a tight-binding model [9]. Assuming a 1 nm diameter and 1 µm length leads to a 3.0×10^8 S/m conductivity.

Experimental measurements of the electrical conductivity of individual SWCNTs place their conductivity on the same order of magnitude as copper. Kong et al. [10] measured a 250 kΩ resistance at room temperature of a SWCNT deposited over electrical contacts 5 μm apart. Assuming a diameter of 1.5 nm (typical of the SWCNTs synthesized for this paper) the conductivity is 1.3x10^7 S/m. Resistances as low as 30 kΩ were measured in this experiment. Assuming the same dimensions, that equates to a high conductivity of 9.4x10^7 S/m. When limiting their measurements to SWCNTs which did not show a gate effect (presumably metallic SWCNTs), Yao et al. [11] found a minimum resistance of 17 kΩ for a SWCNT 1 nm in diameter over a length of 250 nm, which converts to a conductivity of 1.9x10^7 S/m.

There is little debate then that individual CNTs can reach conductivities competitive with metals for electrical transport applications. However, an important aspect of conductivity or resistivity is that a bulk structure's overall conductance can be scaled using its dimensions, as given b:

$$C = \sigma \frac{A}{L}$$

Where C is conductance, σ is conductivity, A is the cross-sectional area of the conductor, and L is the length of the conductor. This law holds well for metal conductors larger than nanoscale. For individual SWCNTs however, electrical properties are strongly dependent on their diameter which influences the bandgap, and conductance is independent of length for CNTs shorter than the mean free path of charge carriers. At the bulk scale (> 10 μm), CNT conductors made from large numbers of individual CNTs cannot be scaled in cross-sectional area easily without changing their morphology or density and thus influencing their electrical transport properties, making the connection between conductance and conductivity difficult. This will be discussed further in the section on measuring electrical properties, and throughout this proposal.

Experimental measurements of the tensile strength of individual CNTs was conducted on arc synthesized MWCNTs attached individually to AFM tips inside an SEM, which were tensile loaded until failure [12]. Applied force in this study was calculated by measuring the deflection of one of the AFM tips. Several of the MWCNTs broke without becoming detached at the AFM tips, breaking in their outermost layers with inner layers “pulling out.” The authors of [12] claim the strength of this outer layer is then 11 to 63 GPa, accounting for only that layer’s thickness. This yields approximately 2 MPa using the CNT’s entire cross section.

1.2 Carbon Nanotube Network Conduction

The high aspect ratio and delocalized orbitals of CNTs lead to strong van der Waals forces between CNTs, even of differing diameters [13], [14], causing CNTs to agglomerate into nano- or microscale bundles and bulk structures that can be kilometers in scale. Bundling affects the electrical properties of the bulk material since the symmetry of the individual CNTs is impacted by their environment. Theoretical work has shown that a bandgap of 0.1 eV is induced in armchair SWCNTs (which have an otherwise zero bandgap) when bundled in perfect alignment with other armchair SWCNTs of the same diameter [15], [16].

The electronic properties of CNTs are also affected by the presence of other species. In CNT research, ‘doping’ refers to atoms, ions, or molecules that are non-covalently bound (physisorbed) into CNT networks or to the surface of individual CNTs.

The mechanism of conductivity change in CNT networks due to doping is still largely unknown, and chemical doping effects are somewhat unpredictable.

An important dopant of CNTs is O_2 since most CNT samples have been handled in an oxygen rich environment, unless exposure to air has been specifically controlled. The sensitivity of CNT electrical properties to oxygen (and difficulty of deoxygenation) was first noted in 2000 [17]. In this study, SWCNT bundles and films were mounted in a vacuum test chamber while the electrical resistivity was measured. The SWCNT samples were exposed to pure oxygen, air, or vacuum. At room temperature, high concentrations of oxygen yielded a lower SWCNT sample resistance, and the initial resistance was recovered when returning to an air environment. The difference in sample resistance between vacuum and oxygen-rich environments was dependent on temperature. The researchers found that oxygen was not fully desorbed from a sample under vacuum until temperatures were in excess of 110 °C. Ultraviolet light exposure under vacuum has also been demonstrated to remove oxygen adsorbates and increase sample resistance [18].

Simulation work has shown that N_2 and O_2 adsorb onto SWCNTs with similar adsorption energies and separations (0.2 eV and 2.3 – 2.8 Å respectively). At crossed (90°) SWCNT junctions, adsorbed O_2 molecules contribute to improved inter-SWCNT conduction more so than adsorbed N_2 molecules. The effect is stronger for junctions of semiconducting SWCNTs than metallic SWCNTs. The researchers also find that neither adsorbed O_2 or N_2 have a strong effect on intra-CNT electrical transmission [19]. Similarly, water has been shown through simulation experiments to have a very weak effect on individual SWCNT electrical properties but that water's weak but long ranged effect on SWCNT networks may enhance the conductivity of the network [20].

In chemical vapor deposition (CVD) synthesis, a carbon containing gas is flowed into a furnace which contains a metal catalyst. There are several ways of introducing the catalyst, and the one of interest here is to have the catalyst in a solid form on a silicon substrate which simply sits in the furnace with the gas passing over it. Commonly used temperatures range from 700 °C to 1100 °C. After the carbonaceous gas is fed into the reaction chamber at the chosen temperature, the catalyst substrate is collected and if synthesis was successful, there will be a layer of CNT material loosely bound to the side of the substrate which contained catalyst. Thin films of the catalyst are deposited on the silicon substrate and then annealed to break the film into small droplets. This annealing step was shown to be necessary – CNTs will not grow directly from the catalyst film, implying the geometry of the catalyst plays an important role [21].

In laser synthesis, the catalyst is vaporized along with the carbon and so it is impossible to control the geometry of the metal which the CNTs grow on. Only the production of SWCNTs is observed. In this method, a target is made from pressing mixed graphite powder with powdered metal catalyst. The target is placed in a furnace in a flowing inert atmosphere, and a laser, often pulsed, is fired at the target [22]. The heat generated by the laser is enough to vaporize the carbon and the metal. Downstream of the target a cold metal collector allows the synthesis products to condense for collection. CNT growth occurs when the carbon and metal condense out of the vapor phase. Condensation of carbon without catalyst can yield a variety of structures as demonstrated from fullerene synthesis. The preferred structure is graphene sheets since there is minimal strain on the bonds. Nucleation of metal particles during condensation is slow, and so it is much preferred for existing particles to grow rather than new ones form. Once several particles have grown in size, their coalescence begins to occur. When both carbon and metal are present in the vapor, the nucleation of carbon structures is much faster than that of the metal and so the metal atoms condense onto the carbonaceous nuclei rather than form their own. Coalescence of the metal particles becomes unlikely since they are attached to much larger carbon structures which block their interaction. This is what prevents growth of the catalyst particle. As carbons condense on the metal and diffuse through to the site of CNT formation, the tube grows. Once this tube is initially formed, it is possible for the catalyst particle to grow from condensation of additional metal atoms without catalyzing the growth of additional CNT walls. This is because the lowest energy state for carbons diffusing though the metal is joined with the pre-existing graphitic cylinder, and not beginning a new shell. This explains why it is possible to find catalyst particles in the synthesis products which are large enough to catalyze MWCNTs even though only SWCNTs have been synthesized. [23]

1.3 Carbon Nanotube Wire Fabrication

CNT wire fabrication techniques can be grouped into three categories: dry spinning, wet spinning, and densification. Dry spun fibers can be produced from two common methods which depend upon the synthesis method of the constituent CNTs.

The first dry spinning method is a single-step method and uses the CNT aerogel produced from a floating catalyst CVD method. The aerogel is a sparse network of CNTs which is low density enough to flow with the carrier gas out of the synthesis furnace where it can be increased in density mechanically by spinning. This is the method utilized by Nanocomp Technologies to produce their commercially available CNT fibers [24]. Continuous fiber drawing from this method was first demonstrated by Li et al. from Cambridge University in 2004 [25]. In this study, CNT synthesis took place at 1050 to 1200 °C using a hydrogen carrier gas, ethanol carbon source, ferrocene iron catalyst source, and thiophene as a sulfur source to increase catalyst activation. By controlling the H_2 flow rate and thiophene concentration, the authors were able to control the distribution of the number of carbon layers in the CNTs. Fibers were capable of being spun under many different conditions, including other oxygen containing carbon feedstock gases. The maximum conductivity measured was 8.3×10^5 S/m and maximum tensile strength was 1 GPa. These measurements assumed a fiber density of 2 g/cm^3.

Later research by the same group, using similar synthesis conditions, applied an acetone vapor to the fibers which densified them upon evaporation, likely due to the capillary forces present. The winding rate (rate at which the fiber was pulled from the synthesis furnace) was also modified in this study. Increased winding rate resulted in lower linear density (mass per length of fiber) but higher density (i.e., the fiber decreased in volume and increased in density), greater strength, and better alignment as measured by polarized Raman spectroscopy. The authors note a bimodal distribution in the specific strength of these yarns, where longer gauge length samples have lower strengths while shorter samples often obtained specific strengths as high as 6.5 N/tex (tex is a unity of linear mass density equivalent to 1 g/km). This is likely due to a nonuniform process which produces fibers with weak points. [26]

Fibers were also fabricated by researchers at Tianjin University using similar synthesis conditions [27]. A mixed acetone and ethanol carbon feedstock allowed for a higher yield rate of CNT fiber, while the H_2 carrier gas, thiophene and ferrocene catalysts were also used. The fibers produced in this study were densified by submersing them in a water bath and then mechanically rolled (calendered) instead of using an acetone spray. Fiber production took place at a rate of 5-20 m/min. The resulting fibers had a conductivity of 5×10^5 S/m and tensile strength of 1.25 GPa.

Vilatela and Windle argued in a perspective [28] that their direct spun CNT fibers (those in [25], [26]) are best characterized and compared to fibrous materials, rather than solid metals. They adopt linear-density based measurements (specific tensile strength and conductivity) to characterize their fibers. The yarn-like characteristics include splaying behavior when cut, kinking, and a fibrous pull-out failure. The CNT yarns have 100 % knot efficiency, meaning that unlike other fibers, the tensile strength is the same when tested with or without an overhand knot incorporated into the fiber.

By changing the sulfur source from thiophene to carbon disulfide, the Cambridge group was able to directly spin fibers with smaller diameters and fewer impurities [29]. Using Raman spectroscopy, the authors predict that the constituent CNTs are single-walled and of metallic electronic type. However, the authors do not give any fiber mechanical or electrical characterization in this work.

Commercially available direct-spun fibers were characterized by Wu et al. [24]. NCTI 1 tex yarns were measured on a mechanical analyzer with in-situ 4 point electrical measurements. Fiber diameters were taken as the average of 10 widths measured via SEM. The resistance of a yarn segment increased during tensile loading. Yarns had a strength of 190 MPa. During cyclic loading below the elastic limit of the yarns, an irreversible resistance increase was measured on the initial loading, then the resistance cycles with loading without hysteresis. Some fibers were found to recoil upon failure.

By synthesizing CNTs for direct spinning using butanol, ferrocene, and thiophene in hydrogen at 1250 °C and altering the thiophene percentage of the precursor mixture, different numbers of CNT walls can be targeted [30]. In this study, an aerogel of CNTs forms in the carrier gas which can be pulled from the reactor at a higher speed than the carrier gas flow. This pulling action aligns the CNTs and condenses them into fibers. By increasing carrier gas flow or decreasing precursor feed rate, the CNT aerogel is made sparser and the fiber drawing induces increased alignment. Fibers with improved alignment has specific tensile strengths of ~0.9 N/tex, greater than those with poor alignment. Once oriented, both SWCNT and MWCNT targeted precursor ratios had roughly equal tensile strengths, while the non-oriented SWCNT fibers were stronger than non-oriented MWCNT fibers. A diameter reduction factor of ~11x was achieved though volatile liquid densification which did not affect alignment or resistance, and slightly improved tensile strength.

Another group of researchers from Shanghai [31] have produced fibers and films from a direct-spinning method using an ethanol carbon feedstock, nitrogen carrier gas, ferrocene catalyst source, and thiophene for catalyst activation. Formation of the cylindrical CNT film was sensitive to the composition and flow rate of the carrier gas and feedstock solution. Acetone spray was not used to condense the film into a fiber, which was instead submerged in water or ethanol and removed for condensation. An unquantified force was required to submerge the gaseous CNT film which may have stretched it simultaneously. Water condensed fibers had a rectangular cross section of 160 µm X 5-9 µm (800 – 1440 µm^2). Ethanol condensed fibers had a rectangular cross section of ~ 45 µm X 20 µm (900 µm^2). Ultimate tensile strength (UTS) is 362 MPa with an elongation of 20-30 % for these fibers. The water condensed fibers were densified by rolling (calendaring) which changed the fiber dimensions to 220 µm X 500 nm (110 µm^2) with approximate densities of 1.3 – 1.8 g cm^{-3}. The thickness was determined by SEM, which can be ambiguous. In figure 4 of [31], we can see that this determination is somewhat subjective. Wide angle X ray diffraction measured an alignment of ~81 %. After densification, the ultimate tensile load was only increased by 1.2x, but the tensile strength was increased 12x to 3.7 – 5.3 (avg 4.3) GPa (independent of gauge length) due to the cross section reduction. Elongation at failure was gauge length dependent, but for a fixed gauge length, densification reduced elongation from 20 % to 10 %. Highest conductivity obtained was 2.27x10^6 S/m.

In additional work by the same group [32], films were not pulled through a bath but instead condensed on an Al foil wetted with ethanol wrapped around a collection drum. An HCl soak was used to remove the film from the drum. Raman G/D ratio was 2.74. Increased winding rate improved CNT alignment (quantified for different collection rates by polarized Raman). The well aligned samples had average tensile strength of 2.8 GPa at strains of 6 – 10 %. The well-aligned sample was subjected to densification by rolling (with ~0 gap between rollers), and the thickness of this sample reduced from 550 nm to 120 nm while the width increased ~20 %. UTS increased to 8.0 – 10.8 GPa with an average 9.6 GPa. From figure 5 of [32], the strain at failure for these samples appears to be 6 – 11 %. From figure S3 of [32], it appears that the actual breaking force of the densified samples is lower than it is prior to densification. It is important to note that the structures in [32] were not cylindrical fibers but flat ribbons, and that they may retain some HCl doping from their processing.

Direct spun fibers have been processed and characterized in a variety of ways. Their stability in aqueous, saline, and acid environments has been studied where they were found to be highly corrosion resistant [33]. They have been hybridized with silver nanoparticles by depositing a silver nanoparticle suspension on the fibers and allowing the solvent to evaporate [34]. The Ag-CNT hybrids had greater conductance than the raw fibers and demonstrated a decrease in conductance at lower temperatures [35]. Fibers soaked in 1,5-Hexadiene and exposed to UV radiation improved in tensile strength due to the incorporated polymer [36].

The second method of dry spinning CNT wires and fibers is a two-step process in which CNTs are grown by CVD onto a substrate to form a vertically aligned array. In certain conditions, such as specific lengths, densities, and entanglements, of the array, a wire can be pulled from the array as depicted by figures in reference [37]. When the areal density (number of CNTs per area) and length of the CNTs allows for it, drawing can be done continuously due to the attractive inter-CNT van der Waals forces. In the first example of this process [38], the authors report that running a current through the wire under vacuum increases the conductivity and tensile strength of the fibers, but do not quantify either. In the first quantitative report on this type of CNT fiber [37], yarns were spun from aligned arrays of MWCNTs approximately 10 nm in diameter. The resulting yarns were between 1 and 10 µm in diameter with tensile strengths as high as 300 MPa and maximum conductivity of 3×10^4 S/m. The authors demonstrate that these yarns can be twisted and braided at the microscale.

The effect of different yarn twisting rates has been studied and found that higher degrees of twist act to densify the yarns when analyzed by focused ion beam cutting and imaging with scanning electron microscopy (SEM) [39]. The researchers in this study found that there was an optimal twist density for high tensile strength, above which CNTs in the fiber were not well aligned enough to contribute positively to the fiber strength. The maximum strength reported was 560 MPa.

Another study drew fibers from aligned arrays of 35 nm MWCNTs grown on a substrate at lower temperatures by using a ferrocene catalyst instead of a deposited catalyst [40]. The resulting yarns were densified by including a twist after fiber spinning, yielding a 300 MPa tensile strength. The authors found that arrays which contained wavy (not straight) CNTs were not capable of being spun into fibers. In another study using fibers spun from aligned arrays, researchers were obtained a conductivity of 7×10^4 S/m by using acetone immersion and evaporation to densify the fibers [41]. These fibers were also submerged in a suspension of silver nanoparticles which deposited on the fiber surface, increasing conductivity to 4.3×10^6 S/m after multiple treatments. 600 MPa strengths were also obtained from fibers produced from this method using ethanol for solvent densification, and in this work, the authors noted that a heat treatment under argon caused the wires to retain the shape in which they were heated [42]. The properties of aligned array spun fibers are sensitive to the CNT synthesis conditions and the fiber spinning and densification conditions.

The second major method of CNT fiber or wire production is often referred to as ‘wet spun’ or ‘extruded’ because these wires are made from a fluid suspension of CNTs and extruded through an orifice (or ‘spinneret’) into a material which causes the CNTs in the suspension to coagulate into a solid. The first demonstration of wires made using this technique was in 2000 [43], when researchers dispersed SWCNTs in water using surfactants to stabilize the dispersion. This dispersion was then extruded through a syringe needle into a co-flowing stream of polymer solution containing 5 wt % polyvinylalcohol. Solid fibers were formed containing both SWCNTs and polymer. The diameter of fibers was close to that of the syringe needle but also depended on the injection rate of the SWCNT dispersion and flow rate of the polymer coagulant bath. The tensile strength of these fibers was 150 MPa and the electrical conductivity was 1×10^4 S/m, which are likely influenced by the presence of polymer in the fiber. Later work by the same group studied the kinetics of the fiber coagulation under the same conditions [44]. To probe the kinetics of this process, wires were extruded into glass tubes with flowing coagulant. Each tube has a section of reduced diameter to cause increased flow rate at varying distances from the extrusion tip. The increased flow rate caused incompletely coagulated sections of the fiber to fracture due to shear stress. It is possible that a similar set-up could be used to induce controlled tensioning of extruded wires to improve their properties.

CNT fibers can also be extruded from polyelectrolyte dispersions and coagulated in water, HCl, or NaI_3 [45]. The highest conductivity wires from these dispersions were coagulated in NaI_3 and had a conductivity of 2.1×10^4 S/m and a tensile strength of 100 MPa. However, the most commonly reported dispersant for forming wet spun wires is chlorosulfonic acid (CSA). CSA and other high-acidity acids have been shown to non-covalently protonate CNTs in solution, overcoming their van der Waals forces and dissolving the CNTs [46]. It is important to note that CSA dispersion of CNTs is thermodynamically favorable and does not require sonication. This enables dispersions of CNTs to be obtained at much higher concentrations than previously discovered. Depending on the acidity of the solvent and the volume fraction of CNTs, different phases are spontaneously favorable (see Figure 2).

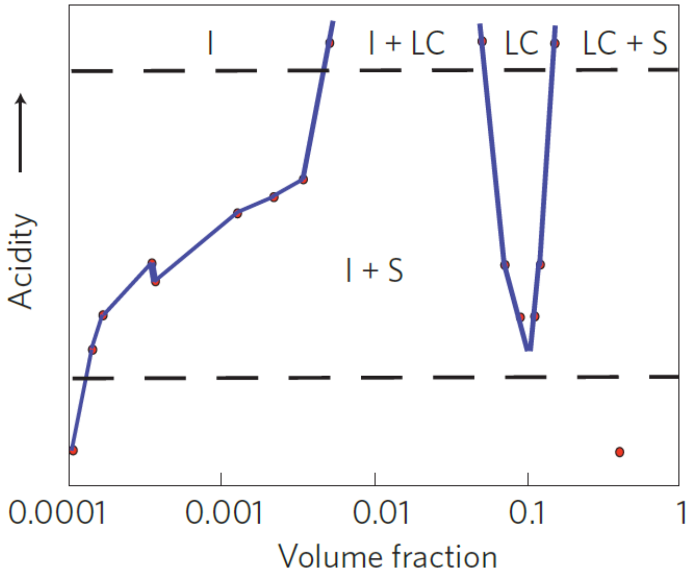

Figure 2. Experimental phase diagram of volume fraction of SWCNTs in increasingly acidic solvent [47], [48].

From this figure we can see where isotropic (I – dispersed CNTs), solid (S – aggregated bundles of CNTs), and liquid crystal (LC – aligned CNTs in the liquid phase) are thermodynamically favorable. The isotropic phase requires very low concentrations (volume fractions) due to high aspect ratios of the CNTs which causes collisions. As we can see from the phase diagram, increasing acidity aids in formation of isotropic and liquid crystalline dispersions. This makes highly acidic solvents favorable. These high concentration dispersions form liquid crystals of CNTs [49]. The alignment and crystallinity of CNTs in these dispersions allows for greater control over the alignment of CNTs in solid structures when the acid is passivated or removed [50]. The solids produced in this method are also not contaminated with surfactants, which can be difficult to remove.

HiPco SWCNTs dispersed in sulfuric acid have been coagulated in water yielding fibers with 4.2x10^5 S/m conductivity [51]. Fibers have been formed from acid dispersions under several conditions. The first were made from HiPco SWCNTs coagulated dispersed in concentrated sulfuric acid and extruded into dilute sulfuric acid and had conductivities as high as 5.0x10^5 S/m and tensile strengths up to 126 MPa [52]. Later improvements on the wet spinning process included co-flowing sulfuric acid coagulant and CSA used as the dispersant. These factors increased the wire conductivity to 8.3x10^5 S/m and tensile strength to 150 MPa [47]. Further improvements in wire performance were made by using double walled CNTs dispersed in CSA and extruded into acetone [53]. After extrusion, the wires contained residual CSA, which acted as a dopant. This was determined by an increase in resistance after a thermal anneal. Doping with iodine reversed, and further decreased, the fiber resistivity. As-extruded fibers (prior to anneal) had an average conductivity of 2.9x10^6 S/m and a tensile strength of 1.0 GPa. This substantial improvement in conductivity is largely due to the selection of CNT type in the starting dispersion, which motivates the study of CNT wires extruded from dispersions of other CNT types as discussed throughout this proposal.

The final method of wire fabrication is radial densification. This technique involves pulling material through a funnel-shaped drawing die to form it into a cylinder or reduce its diameter. Drawing dies have been used on as-synthesized CVD CNT material to form wires (without reported electrical or mechanical properties) [54]. When radial densification has been applied to rolled sheets of CNT material, conductivities of 1.3x10^6 S/m when doped and 2x10^5 S/m without $KAuBr_4$ doping.

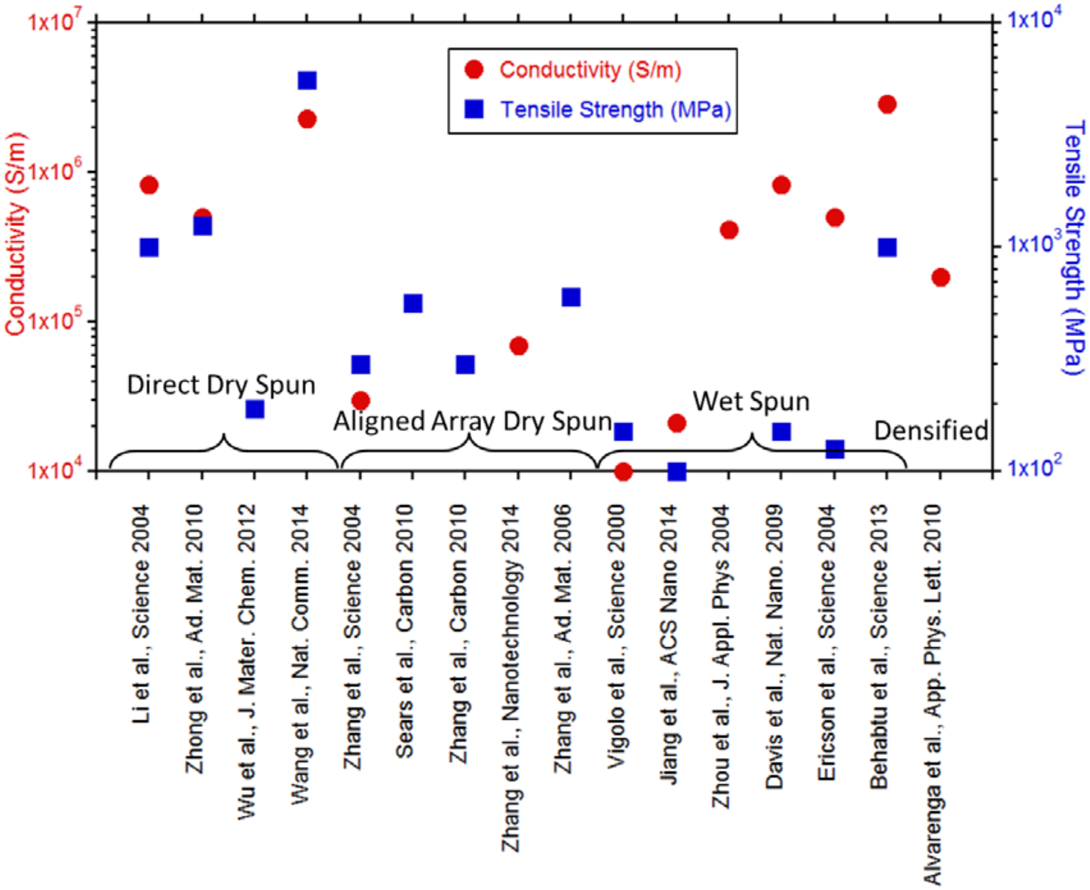

Figure 3. Review of wire and fiber properties from the literature review as of 2015.

1.4 Research Opportunities and Dissertation Objectives

Research Opportunities

- Develop understanding of the coagulation of CNT dispersion and its effects on extruded wire properties.
- Engineer high conductivity CNT wires with high current carrying capabilities

Dissertation Objectives

- Enhance the conductivity of extruded CNT wires through the use of high-conductivity, laser vaporized SWCNTs and optimized processing parameters.
- Develop control over extruded wire properties through systematic modification of factors which influence CNT dispersion coagulation.
- Improve the use of chemical dopants on CNT networks through developing understanding of the doping delivery mechanism.
- Determine proper high-current characterization techniques and use failure analysis to determine the relevant factors in enhancing the maximum current of CN wires.

As the previous section has demonstrated, substantial gaps in our understanding of electrical conduction in CNT networks exist due to the complexity of electrical and morphological factors. The contribution of network morphology, CNT type, and chemical doping on electrical conduction cannot be predicted. This lack of theoretical understanding of CNT networks prohibits the design of optimal CNT conductors and opens opportunities for experimental work to modify and measure the performance of such conductors. Furthermore, while research has been done on the behavior of CNTs and other rod-like molecules in dispersion, little quantitative work has been done on the coagulation of these dispersions. This leaves another area of CNT behavior without scientific understanding to guide the development of optimal CNT wires. With these two areas of CNT theory unsatisfactorily developed, there is further opportunity to engineer and construct CNT wire production and treatment techniques which create CNT constructs with improved electrical and mechanical properties.

These gaps in scientific understanding and CNT conductor performance combined with the resources available at RIT create the opportunity to conduct novel research in four related areas, each with their own objectives. Fabricating high conductivity wires through CSA dispersion and extrusion could benefit from the use of high conductivity laser vaporized SWCNTs. An objective of the dissertation is to develop control over properties of these extruded wires through systematic modification of factors such as the coagulant temperature and properties and CNT type, which influence CNT dispersion coagulation. Chemical doping techniques will be improved by identifying novel dopants of interest and quantifying their interactions with CNT conductors and the electronic doping mechanism.

Chapter 2. Characterization of Carbon Nanotube Wires

CNT wires are non-uniform, anisotropic structures. This makes their comparison to bulk metals and polymers through material-specific metrics such as conductivity and tensile strength difficult. The following sections elaborate on experimental techniques and frequently-used measurements used in quantifying CNT and CNT bulk structure properties.

2.1 Measurements on CNT Wires

2.1.1 Resistance

Electrical measurements on CNT wires are conducted using a 4-pt method to eliminate the effect of contact resistance [55]. In this method, the probes are frequently non-uniformly spaced but inline, with the outer two probes inducing a set current and the inner two probes measuring the voltage drop. The set current is swept over a range of values to ensure that the material is ohmic and the resistance of the wire is calculated from the slope of the resulting line using Ohm's law.

Electrical measurements on CNT papers and films are conducted using the van der Pauw method for flat, simply connected structures of arbitrary shape [56], [57]. In short, this technique involves placing four electrical probes (A, B, C, and D) around the perimeter of the paper or film in order. A current is induced from A to B and the voltage drop is measured from C to D and a resistance (denoted R_H) is calculated. Then the current is induced from A to D and the voltage measured between B and C, and a second resistance value calculated (denoted R_V). The sheet resistance is then related to these resistances by the van der Pauw equation:

$$e^{\frac{-\pi R_H}{R_S}} + e^{\frac{-\pi R_V}{R_S}} = 1$$

where R_S is the sheet resistance. The sheet resistance is calculated numerically. This method relies on several assumptions: that the device measured is thin (no conduction occurs normal to the plane of the probes), that the probes are infinitely small, the device is simply connected (no holes), and that the device is isotropic and homogeneous. The first two assumptions are reasonably valid for thin films and large CNT papers where the thickness is several orders of magnitude less than the surface area and the probe tips are small. However, many CNT papers and films are not homogeneous and isotropic, and the fibrous nature of their composition cannot preclude any holes in their structure.

2.1.2 Length

Many wire metrics are normalized on a per-length basis. This simply requires measuring the length of a wire sample using calipers, rulers, or calibrated microscopy. Error in these measurements comes from wires which are not pulled taught or over-strained during length measurement. Since most samples characterized are typically 3-10 cm in length, the error in this metric is often insignificant.

2.1.3 Cross Section

The cross-sectional area of a sample is used in calculating the electrical conductivity and tensile strength of a material. Some wires and papers are assumed to have a specific cross-sectional geometry, for example densified CNT wires and commercial Cu wires are assumed to have a circular cross section, and the cross-sectional area is extrinsically measured by measuring a diameter, thickness, etc. For fibrous materials, the cross section can be irregular, requiring estimation from multiple images, or a cut and image technique. Cut-and- image techniques must to cut perpendicular to the major axis of the conductor and try to preserve the original geometry of the conductor, which often relies on embedding in a hard material such as epoxy, focused ion beam milling, or laser cutting. Imaging can then be done by SEM or optical microscopy with extra care taken to be sure the cross section is mounted perpendicular to the optical axis.

2.1.4 Mass

Thin filaments of CNT wires such as those produced from extrusion and dry spinning can weigh less than 1 g/m. Thus to determine the mass of small samples used for evaluating wire properties requires the use of a high resolution microbalance. These types of thin, flexible CNT wires are often compared to yarns rather than wires. Yarns in the textile industry are characterized by their linear mass density (mass per length) and a commonly used unit is the tex, which is equivalent to 1 g/km or 1 mg/m.

2.1.5 Breaking Force

Breaking force is defined as the maximum amount of tensile force which can be applied to a test structure. This is measured by a load cell in a dynamic mechanical analyzer (DMA). NPRL has a TA Q800 DMA with a maximum applied force of 18 N and a resolution of 10 μN, and an Instron 5944 Mechanical Analyzer with a load cell maximum of 2 kN and a resolution of 1 μN.

2.2 Standard Material Metrics

2.2.1 Electrical Conductivity

Conductivity (σ) is a metric used to describe the ability of an isotropic, uniform metal, semiconductor, or conductive polymer to conduct electricity. In these materials, it can be determined from a sample by measuring the resistance and accounting for the sample's geometry as described in equation (1):

$$\sigma = \frac{L}{RA} \tag{1}$$

Where L is the sample length, R is the sample resistance, and A is the cross-sectional area. Due to the anisotropic, nonhomogeneous nature of bulk CNTs, the more general, vector based definition should be applied:

$$\vec{J} = \sigma\vec{E} \tag{2}$$

Where $\vec{J}$ is current density and $\vec{E}$ is the applied electric field. In scenarios where current density depends on the location within the sample (nonhomogeneous) and the direction of the applied electric field (anisotropic), conductivity becomes a 9-dimensional tensor value. This fact, coupled with the difficulties associated with measuring the cross-sectional area of a carbon nanotube wire make conductivity a difficult metric for use in comparing CNT wires. However, often in wire applications engineering requirements will specify maximum volumes and resistances for interconnects. Therefore, using the definition in equation (1) with an approximate CNT wire cross section can make the engineering conductivity of a given CNT wire a useful design metric.

In wire densification, a given mass of CNT material constitutes a conductor which is pulled through radial densification dies. While the diameter of the conductor is reduced due to removal of void space, its resistance stays the same. An improvement in conductivity is then demonstrated, which can be useful for engineering design specifications, but the ability of the CNTs to conduct electricity has not been influenced, as it would have been with chemical doping or CNT type modification. Therefore, engineering conductivity measurements are not useful in comparing the ability of CNT wires fabricated using different materials and processing techniques. For these types of comparisons, it is more instructive to use specific conductivity which is defined in the following section.

2.2.2 Specific Conductivity

The electrical performance of the wires was quantitatively compared by measuring the resistance per length (R/L) which is related to electrical conductivity by cross-sectional area, and to specific conductivity by the wire's mass per length (M/L), as described in equation (3):

$$\sigma_s = \frac{\sigma}{D} = \frac{\left(\frac{L}{R}\right)\left(\frac{1}{A}\right)}{\left(\frac{M}{L}\right)\left(\frac{1}{A}\right)} = \frac{L^2}{RM} \qquad \textbf{(3)}$$

where σ_s is the specific conductivity in S m^2 kg^{-1}, σ is the electrical conductivity in S/m, D is the density in kg m^{-3}, L is the wire length in m, R is the wire end-to-end resistance in Ω, A is the wire cross-sectional area in m^2, and M is the wire mass in kg.

2.2.3 Tensile Strength

Specific tensile strength (also known as breaking tenacity) is a measurement that does not require cross-sectional area measurement, is related to the wire's breaking force by its mass per length (M/L) and is defined as shown in equation (4):

$$T_s = \frac{T}{D} = \frac{F\left(\frac{1}{A}\right)}{\left(\frac{M}{L}\right)\left(\frac{1}{A}\right)} = \frac{FL}{M} \tag{4}$$

where T_s is the specific tensile strength in N m kg^{-1}, T is the tensile strength in Pa, F is the ultimate force applied to the wire before breaking in N, and M is the wire mass in kg.

2.3 Carbon Nanotube Characterization Techniques

2.3.1 Thermogravimetric Analysis (TGA)

Thermogravimetric analysis (TGA) has been widely applied to CNT samples as a measure of purity, quality, and temperature stability [58], [59]. TGA involves heating a sample in a controlled manner while simultaneously measuring the mass of the sample. For carbonaceous samples in air, oxidation often causes mass loss. Results are plotted with mass as a percentage of the initial sample mass before heating as a function of temperature (Figure 4). Often, the derivate mass percent (%/°C) is given as a function of temperature to better visualize points of maximum decomposition rate. In a CNT sample, distinct peaks in the derivate mass percent indicate oxidation of carbonaceous impurities and oxidation of CNTs at different temperatures, while the residual mass (weight % at highest temperature) is used to indicate the mass of oxidized metals in the sample. Presence of chemical dopants can alter the TGA spectra of CNT samples [60].

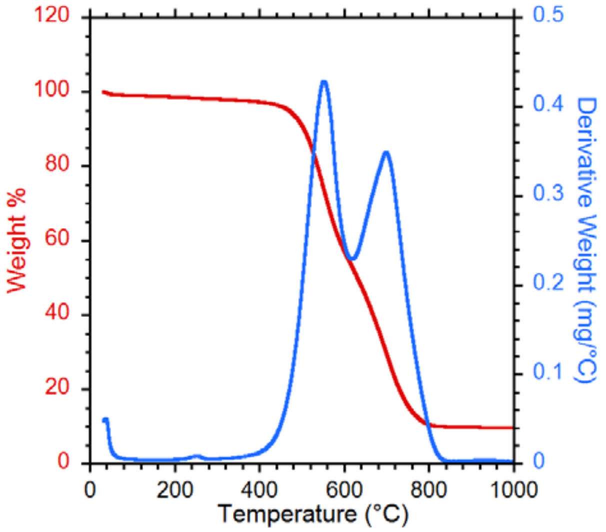

Figure 4. TGA data from a sample of arc-synthesized SWCNTs.

2.3.2 Raman Spectroscopy

Due to their optical and electronic properties, CNTs lend themselves to study via Raman spectroscopy. Raman scattering occurs when light is scattered by a molecule and energy is either lost to or gained from the molecule, resulting in scattered photons of a different energy than the incident light. This energy is lost or gained from allowed vibrational modes (phonons) in the sample. Raman spectroscopy typically uses monochromatic light to irradiate a sample and measures the intensity of light scattered as a function of the Raman shift (the difference in wavelength between incident and scattered light). Several resonant Raman effects take place in CNTs and their intensity and Raman shift are influenced by the CNT's environment, making Raman spectroscopy a useful characterization tool.

A typical Raman spectrum of a bulk SWCNT sample is shown in Figure 5. Several of the features in this spectrum can be instructive. The first is a set of peaks at

100 – 300 cm^{-1}, known as the radial breathing modes (RBM). This name comes from the resonant vibrational mode that consists of expansion and contraction of the SWCNT in the radial direction. The wavenumber of the peaks in the RBMs is correlated to the diameter of the SWCNT [61], [62], and these peaks are suppressed for samples of MWCNTs [63].

Next, the feature at ~1300 cm^{-1} is known as the D band (for Defect or Disorder). The intensity of this feature is dependent on the amount of symmetry-breaking defects in a CNT including sp^3 bonding, substitutional atoms, vacancies, etc. The largest feature at ~1500 cm^{-1} is the G-band (for Graphitic), which originates from the carbon-carbon bond stretching in graphitic materials and is split into G- and G+ features in CNTs due to differences in bond stretching axially and circumferentially. The G-band lineshape is dependent on the semiconducting and metallic SWCNT content of a sample [64]. Finally, the G' band at ~2700 cm^{-1} is also a signature of sp^2 bonded carbons. Its exact Raman shift location is dependent on the frequency of the incident laser light and is sensitive to the presence of p- and n-type dopants in a CNT sample [65]. A quantitative measure of defect density in a CNT sample can be given by the ratios of the D/G band intensities [66].

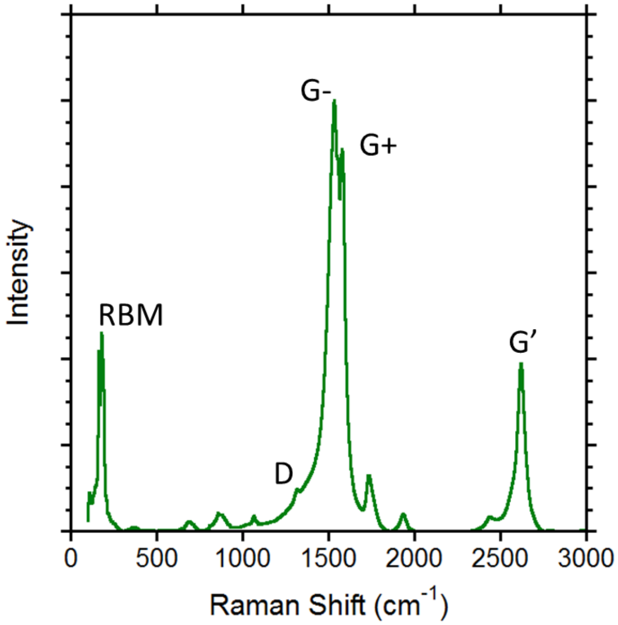

Figure 5. Raman spectrum of a purified bulk laser-vaporized SWCNT paper with several features labeled.

2.3.3 Purity Assessment

Carbonaceous purity assessment of a SWCNT sample is best determined by the methods described in [67], [68]. This method involves dispersion of a purified standard sample in an organic solvent and calculation of the optical absorption extinction coefficients corresponding to the second semiconducting and first metallic transitions in the sample through a dilution series. Extinction coefficients of the carbonaceous impurities are determined at the same wavelengths by using a dilution series on synthesis products from the SWCNT precursors without catalyst present. The ratio of SWCNT concentration C_{SWCNT} to carbonaceous impurity concentration C_{CI} for a SWCNT sample is then:

$$\frac{C_{SWCNT}}{C_{CI}} = \frac{A(M) \cdot \epsilon_{CI}(S) - A(S) \cdot \epsilon_{CI}(M)}{A(S) \cdot \epsilon(M) - A(M) \cdot \epsilon(S)} \tag{5}$$

Where $A(M)$ is the absorbance of at the metallic peak wavelength, $A(S)$ is the absorbance of at the semiconducting peak wavelength, $\epsilon(M)$ is the metallic peak extinction coefficient, $\epsilon(S)$ is the semiconducting peak extinction coefficient, $\epsilon_{CI}(M)$ is the extinction coefficient of the carbonaceous impurities at the metallic peak wavelength, and $\epsilon_{CI}(S)$ is the extinction coefficient of the carbonaceous impurities at the semiconducting peak wavelength [68].

Chapter 3. Extrusion of Laser Vaporized Single Wall Carbon Nanotubes

Typically, the CNT starting material for extruded CNT wires has been either HiPco SWCNTs or few-walled 5 µm long CNTs [47], [52], [53]. High conductivities have been measured on papers of SWCNTs produced by laser vaporization [69], making them a desirable and unexplored material of choice for wet spinning SWCNT wires. Established methods also provide a high degree of control over LV-SWCNT purity [67], [68]. The use of a new starting material motivates examination of the *in-situ* and post processing parameters of wire extrusion. Wires will be fabricated from CSA dispersions of both as-produced and purified SWCNT starting materials. The *in-situ* parameters of coagulant composition and coagulant bath depth will be evaluated for their impact on the resulting wire tensile strength and electrical conductivity. Post processing will also explored using mechanical strain during drying to realize SWCNT wires with high room temperature electrical conductivity.

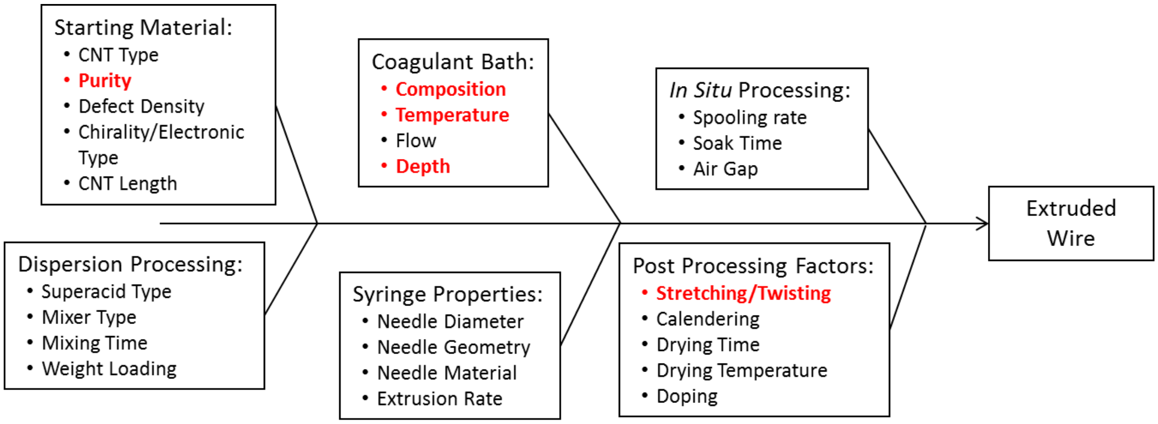

Figure 6. Process diagram of factors influencing CNT wire extrusion, with the factors investigated in the chapter highlighted in red.

3.1 Laser Vaporization and Purification of Single Wall Carbon Nanotubes

3.1.1 Synthesis of Laser Vaporized SWCNT Materials

Laser vaporization is a CNT synthesis method which does not produce any MWCNTs. During the synthesis process, a graphite target is placed in a furnace with a flowing inert carrier gas ambient. The graphite target consists of high purity graphite flake mixed with metal catalyst particles and is formed by compressing this mixture into a cylinder. Laser pulses are rastered over the surface of the target. The heat generated in the target by these pulses is enough to vaporize both the carbon from the graphite, and the metal from the catalyst particles. Downstream of the target is a cool zone or cold trap. As the carrier gas moves towards these areas, it cools and allows for condensation of the vaporized carbon and metal. Condensation of carbon from the vapor to the solid phase without catalyst interaction yields various amorphous and nanostructured carbon species. Through interaction with condensing metal particles, carbon atoms will diffuse though the metal-carbide eutectic and either form a shell or a protruding tube of sp^2 hybridized carbon that grows as more carbon condenses onto the catalyst particle. This latter scenario describes the growth of a CNT. The resulting material is called as-produced (AP) laser SWCNT material and contains CNTs, amorphous and nanostructured carbon impurities, and condensed metal catalyst particles. The AP laser SWCNT material can be approximately 25% SWCNT content by carbonaceous mass as determined by the purity assessment technique described in section 2.3.3.

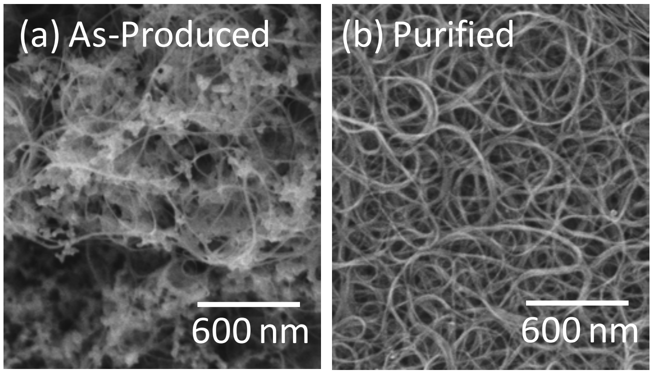

Figure 7. (a) SEM image of AP laser SWCNT material which includes carbonaceous and metal catalyst impurities. (b) SEM micrograph of laser SWCNTs after a purification procedure described in section 3.1.2

3.1.2 Purification of SWCNT Materials

To obtain high-purity laser SWCNTs, the AP laser SWCNT material undergoes a multiple-step purification process. This process begins with refluxing the material in an acidic medium to functionalize the carbonaceous impurities in the sample, increasing their solubility, and dissolve residual metal catalyst particles. The remaining solids are then filtered out and rinsed with water and organic solvents, which removes the water- and organic-soluble carbonaceous impurities. The resulting refluxed and filtered material is then thermally oxidized at a temperature below that of the oxidation point of SWCNTs to remove additional carbonaceous impurities. This oxidation of carbon exposes metal catalyst particles which had been encased in carbon during synthesis. These exposed metal particles can now be dissolved by soaking in an acid such as HCl. Typically, soaking CNT materials in acid can contaminate the material with residual acid or functionalized CNTs, so an additional oxidation or anneal is used to remove them. Following this procedure, SWCNT samples have been created with > 99% SWCNT content by carbonaceous mass as determined by the purity assessment technique described in section 2.3.3.

3.2 Influence of Impurity Presence in Extruded Laser SWCNT Wires

Carbonaceous and metal catalyst particles are two types of impurities commonly found in SWCNT samples which result from their synthesis [67]. Carbonaceous impurities include small, amorphous carbon molecules, and nanostructured carbon molecules such as grapheme and fullerenes which do not include SWCNTs. Carbonaceous impurities are often electrically conductive, but usually not to the same degree as SWCNTs. Metal catalyst particles include nanoparticles of Ni and Co which result from the condensation of vaporized metal catalyst during synthesis. It is unknown if the presence of impurities could improve wire conductivity due to their ability to fill voids in the wires with conductive materials, or detract from wire conductivity because these materials are less conductive than SWCNTs and may inhibit the ability of SWCNTs to form liquid crystals in dispersion.

Two sets of wires were extruded for comparison to determine the effects of impurities in a SWCNT dispersion on the electrical conductivity of the resulting wires. One set of wires will be extruded from AP laser vaporized SWCNTs which have been dispersed in CSA. The other set was be extruded from an equal mass of purified SWCNT material dispersed in CSA. Comparing these two sets of wires by conductivity and specific conductivity will allow for the determination of the effect of impurities in the CSA dispersion on the conductivity of the resulting extruded wires.

SWCNT soot was synthesized using the laser vaporization technique [70], [71]. Graphite targets pressed at 20,000 psi and containing 3 wt % Ni (submicron diameter) and 3 wt % Co (<2 µm diameter) were placed in a 1150 °C tube furnace under flowing Ar. Laser pulses from a Light Age model RD-C Epicare 755 nm laser were rastered over the surface of the graphite target at a 2 Hz pulse rate. A portion of the resulting as-produced SWCNTs (AP-SWCNTs) was purified to remove residual catalyst and carbonaceous impurities using a previously published technique [72]. In short, 300 mg batches of soot were refluxed in 300 mL deionized (DI) water, 72 mL nitric acid, and 30 mL hydrochloric acid for 16 hours before filtration over 90 mm Pall Zefluor polytetrafluoroethylene filter membranes (1 µm pore size) and rinsing with DI water. The resulting SWCNT paper was rinsed with alternating washes of acetone and DI water until the effluent was colorless before removal from the filter membrane. SWCNT papers were subsequently thermally oxidized by ramp-stop to 560 °C at 10 °C/min from room temperature under flowing air and then soaked in concentrated hydrochloric acid for 1 hr. Purified SWCNT papers were dried for 16 hrs in a vacuum oven at ~100 °C before being dispersed.

Dispersions were fabricated by combining the appropriate mass of AP-SWCNTs or purified SWCNTs (weighed on an Ohaus EP214C Explorer Pro Analytical Balance) with chlorosulfonic acid (CSA), (Sigma-Aldrich) in a glove box. Dispersions were mixed by five alternating cycles of 10 min in a Resodyne LabRAM acoustic mixer at 50% power and 20 min in a Thinky AR-100 planetary centrifugal mixer. The SWCNTs-CSA dispersions were transferred to glass syringes with stainless steel hubs and 24 gauge stainless steel syringe needles (Cadence) for extrusion. The dispersion was extruded through the syringe tip, which was submerged < 5 mm into the surface of a coagulant bath consisting of a single liquid (various grades, Sigma-Aldrich), and the coagulating wire was allowed to sink to the bottom of the coagulant vessel. The depth of each coagulant bath was varied by using glass vessels of different heights. The length of the extruded wires was greater than three times the depth of the coagulant bath, and the middle third of each segment was cut and mounted on glass slides for characterization. A standard operating procedure for extruded wire production can be found in Appendix B.

Electrical resistance was measured using an inline four-point probe connected to a National Instruments NI PXI-5652 source/measure unit and NI PXI-4071 digital multi meter at room temperature (~20 °C). The wire mass and length were measured using a Mettler-Toledo XP2U microbalance with 0.1 µg resolution and a Fowler caliper with a resolution of 0.01 mm respectively. SEM images of SWCNT materials prior to dispersion and extruded wires were taken on a field emission Hitachi S900 with an accelerating voltage of 2 kV and an emission current of 10 µA. Wire cross sections were determined using image analysis of multiple SEM images from each segment of wire. Tensile testing of wire segments was conducted on a TA Instruments Q800 dynamic mechanical analyzer using a film tension clamp by applying a constant force ramp rate of 0.01 N/min at 20 °C to determine the ultimate tensile strength at failure.

Laser-synthesized SWCNTs were selected for this study due to the established control over purity [71], [72], high reported intrinsic conductivity [69], and for their unexplored potential for wet spun CNT wires. Carbonaceous and metal catalyst particles are two types of impurities commonly found in SWCNT samples which result from their synthesis [72]. Two sets of wires were extruded for comparison to determine the effects of impurities in a SWCNT dispersion on the electrical conductivity of the resulting wires. The first set of wires was extruded from a dispersion containing 38.3 mg AP-SWCNTs per mL CSA (*i.e.*, 2.1 wt % AP-SWCNT material in dispersion). An SEM of the AP-SWCNTs used to create this dispersion is presented in Figure 7a. AP-SWCNT samples contain 20-30% SWCNTs by carbonaceous mass [71]. Small bundles of SWCNTs can be seen in the SEM image as well as a large volume fraction of impurities. The second set of wires was extruded from a dispersion containing 40.0 mg purified SWCNTs per mL CSA (*i.e.*, 2.2 wt % purified SWCNT material in dispersion). An SEM image of the purified SWCNTs used to create the second dispersion is shown in Figure 7b, demonstrating excellent SWCNT quality and a dramatic reduction in the amount of impurities over the AP-SWCNT sample. Purified SWCNT samples contain > 99% SWCNTs by carbonaceous mass [71]. Wires were extruded from both dispersions into 20 °C acetone coagulant baths which had a depth of 4.5 cm. SEM images of wires extruded from AP-SWCNTs and purified SWCNTs are shown in panels a and b of Figure 8, respectively. The presence of carbonaceous impurities in the wires extruded from the AP-SWCNT dispersion is evident in the high magnification SEM images (Figure 8c) since bundles of SWCNTs cannot be seen on the wire surface. In comparison, well resolved bundles of SWCNTs are observed on the wires extruded from the purified SWCNT dispersion (Figure 8d).

The average specific conductivity of wires produced from the AP-SWCNT dispersion was 40 S m^2 kg^{-1} while those produced from the purified SWCNT dispersion was 1000 S m^2 kg^{-1}. The masses of the 4-5 cm SWCNT wire samples that were electrically characterized were accurately measured in the range of 20-200 µg using an ultramicrobalance with resolution of 0.1 µg. Increased specific conductivity in wires extruded from the purified SWCNT dispersion is attributed to larger mass and volume fractions of highly conductive SWCNTs. Thus, the presence of residual impurities from synthesis has negatively impacted conductivity by preventing SWCNTs from forming dense, aligned bundles upon coagulation. Therefore in the following studies, all wires are extruded from dispersions of purified SWCNTs in order to study the coagulation dynamics of wires with the highest possible conductivity.

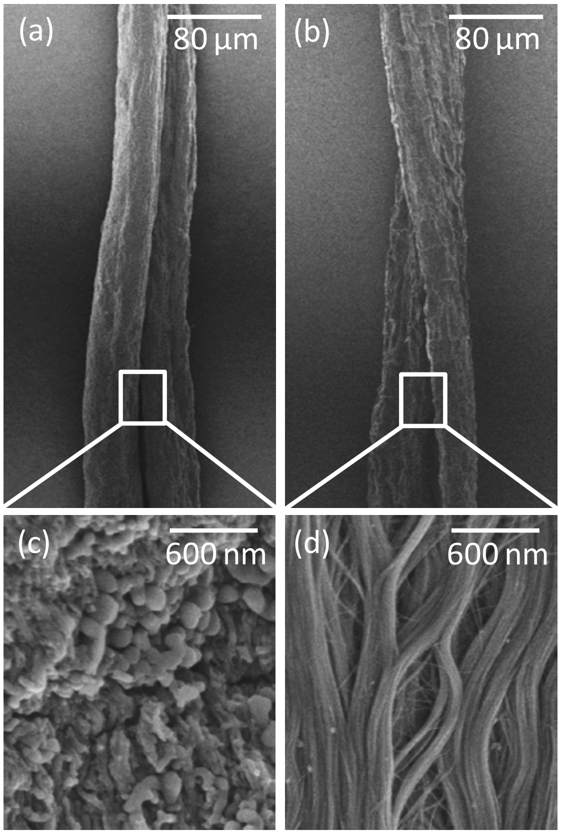

Figure 8. (a) Extruded wire made from a SWCNT-CSA dispersion of AP laser SWCNT material. (b) Extruded wire made from a SWCNT-CSA dispersion of purified SWCNT material. (c) and (d) are higher magnification images of the surfaces of the wires in (a) and (b) respectively.

3.3 Coagulation in Various Solvents

3.3.1 Single-Solvent Approach

Previous work has demonstrated several successful coagulants for CNT wire extrusion, including water, acetone, diethyl ether, and sulfuric acid [52], [53]. However, a direct and controlled comparison of the electrical and mechanical properties of the wires into these and other various liquids does not yet exist. The selection of liquid used as a coagulant influences the rate of diffusion of CSA from the SWCNT liquid crystals into the liquid, thus influencing the act of coagulation. Coagulation dynamics are a factor heavily responsible for a wire's morphology and microstructure, which influence its bulk properties. Therefore, selection of the liquid or liquids which comprise the coagulant bath is an aspect of wire extrusion which can be engineered to produce higher conductivity wires and is of interest for further investigation.

Previous work has demonstrated several successful coagulants for CNT wire extrusion, including water, acetone, diethyl ether, and sulfuric acid [52], [53]. In the present work, extrusions are conducted into eight liquids (acetone, acetonitrile, chloroform, N,N-Dimethylacetamide (DMA), deionized water, dimethyl sulfoxide (DMSO), ethanol and hexanes) at room temperature in vials with a height of 8 cm to compare the effects of coagulant bath composition on the extruded wire properties. SEM images of the resulting wires from six of these solvents are presented in Figure 9. Data from attempted extrusions into hexanes and water is not available since these solvents did not produce coherent wires. In the case of hexanes, the SWCNT-CSA dispersion formed droplets which remained fluid in the liquid hexanes rather than coagulating into a solid. When water is used as a coagulant bath, the dispersion solidified but underwent a violent reaction that results in bubbling and a non-coherent wire. Wires extruded into acetone (Figure 9a) were ribbon-like rather than cylindrical and the acetone bath exhibited a color change following extrusion with shades of yellow and orange, indicating a reaction between CSA and acetone. The SWCNT wires that were coagulated in an acetone bath displayed a high degree of uniformity along the wire axis, as well as large, aligned bundles of SWCNTs on their surface (Figure 9a inset). Wires that were coagulated in either acetonitrile Figure 9b) or DMA (Figure 9c) baths are also highly uniform, but exhibit less surface bundle alignment than those extruded into acetone (based on the high magnification SEM insets in Figure 9 for each). Wires that were coagulated in chloroform (Figure 9d) or DMA both have smaller diameters than wires from other coagulant baths, likely due to a slow rate of coagulation which allows the wire to become thinner and elongated while solidifying due the vertical extrusion setup. Dispersions extruded into chloroform baths which were greater than 8 cm in height have been observed to break into segments before completely coagulating. This also indicates a low coagulation rate since the uncoagulated wire does not possess the tensile strength to support longer segments of itself. Wires extruded into DMSO were larger in diameter and possessed greater void space in between SWCNT bundles on their surfaces (Figure 9e). The increased void space may be attributed to the high boiling point of DMSO resulting in slow drying of the wire with residual DMSO remaining between SWCNT bundles. Wires extruded into ethanol display very poor uniformity and a low degree of surface bundle alignment (Figure 9f). During extrusion in ethanol, bubbling on the surface of the extruded wire can be observed, indicating a reaction between CSA and either ethanol or trace water present in the bath. Thus any bubbling from a coagulant bath reaction with CSA disrupts coagulation and causes wire blistering, leading to non-uniform wire morphologies and poorly aligned SWCNT bundles. The SEM comparison in Figure 9 indicates that there are marked differences in the morphology of wires due to the coagulant composition. These differences are attributed to varying interactions between the coagulant and CSA, including reactions and diffusion rates, which influence coagulation of the dispersion into a solid.

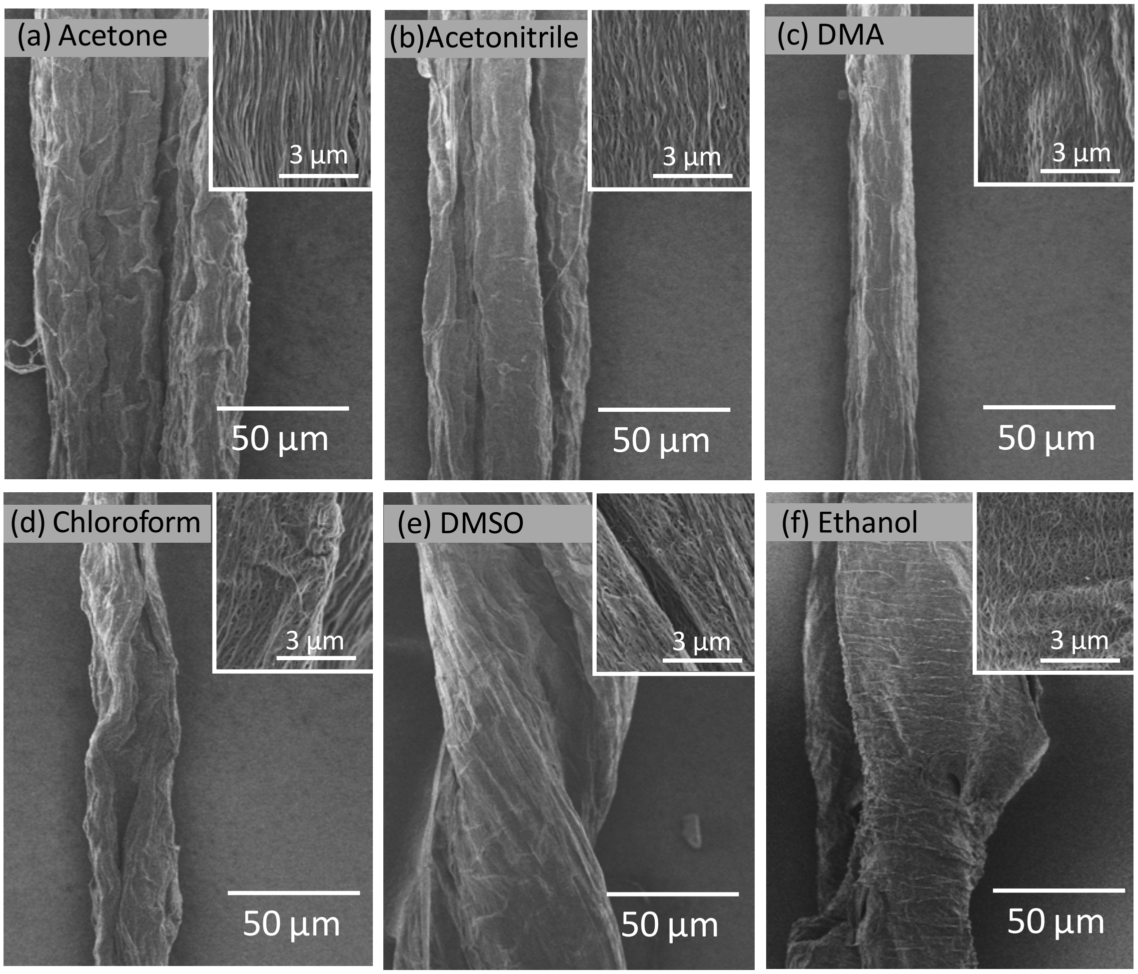

Figure 9. SEM images of wires extruded from purified laser SWCNT dispersions into (a) acetone, (b) acetonitrile, (c) N,N-dimethylacetamide, (d) chloroform, (e) dimethyl sulfoxide, and (f) ethanol. Insets are higher magnification of each wire.

The mechanical and electrical properties of the SWCNT wires, represented in Figure 10, have been measured in order to determine how coagulant selection influences the resulting wire properties. The specific conductivity and specific tensile strength results from this analysis are shown in Figure 10a.

Electrical conductivity and tensile strength for these wires are presented in Figure 10b using cross-sectional areas determined from SEM images. Improved electrical performance correlates well with tensile strength when normalized to either wire mass/length or cross-sectional area. Qualitatively, wires with a high degree of uniformity and alignment, as seen in in Figure 9, were those with the best electrical and mechanical properties. This observation indicates that improved wire performance is attained through the use of coagulation parameters that favor highly uniform and ordered wires. The subtle differences between Figure 10a and b are due to variations in wire density between wires extruded into different coagulant baths, likely due to the coagulation dynamics and residual solvent present. The coagulant liquid can be removed at higher temperatures, but annealing was determined to decrease wire electrical properties due to the removal of residual CSA which acts as a chemical dopant. Thus, in the following optimization experiments, acetone is used as the liquid coagulant due to its ability to form highly conductive, strong, and uniform wires with minimal residual solvent.

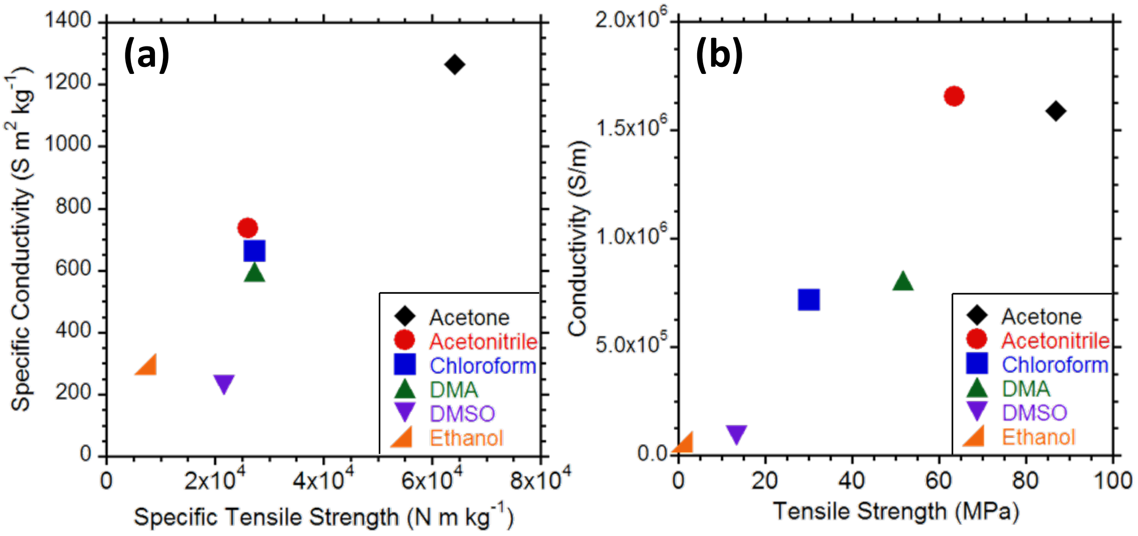

Figure 10. Properties of SWCNT wires extruded into various composition coagulant baths analyzed by (a) specific conductivity and specific tensile strength and (b) electrical conductivity and tensile strength.

In addition to the empirical model obtained from DoE techniques, a scientific understanding of the fluid properties which promote favorable wire coagulation is desirable to inform better coagulant selection. After conducting a survey of liquids for use as coagulant baths, the specific conductivities from the study in Figure 10 have been compared by several quantitative parameters of each coagulant, such as boiling point, polarity, viscosity, density, molecular weight, and surface tension. The results are shown in Figure 11. In many of these cases, there is only a weak trend, but low-boiling point, low-viscosity solvents may be ideal for high specific conductivity. Future work in this area may be improved by selecting a solvent which is available with varying functional groups and side-chain lengths which can lead to more direct correlations between solvent properties and specific conductivity with minimal changes in confounding factors such as reactivity. This comparison may elucidate trends which lead to improved specific conductivity, aiding in the selection of possibly desirable coagulants which have not been previously explored. This may also provide insight into the mechanism of SWCNT dispersion coagulation.

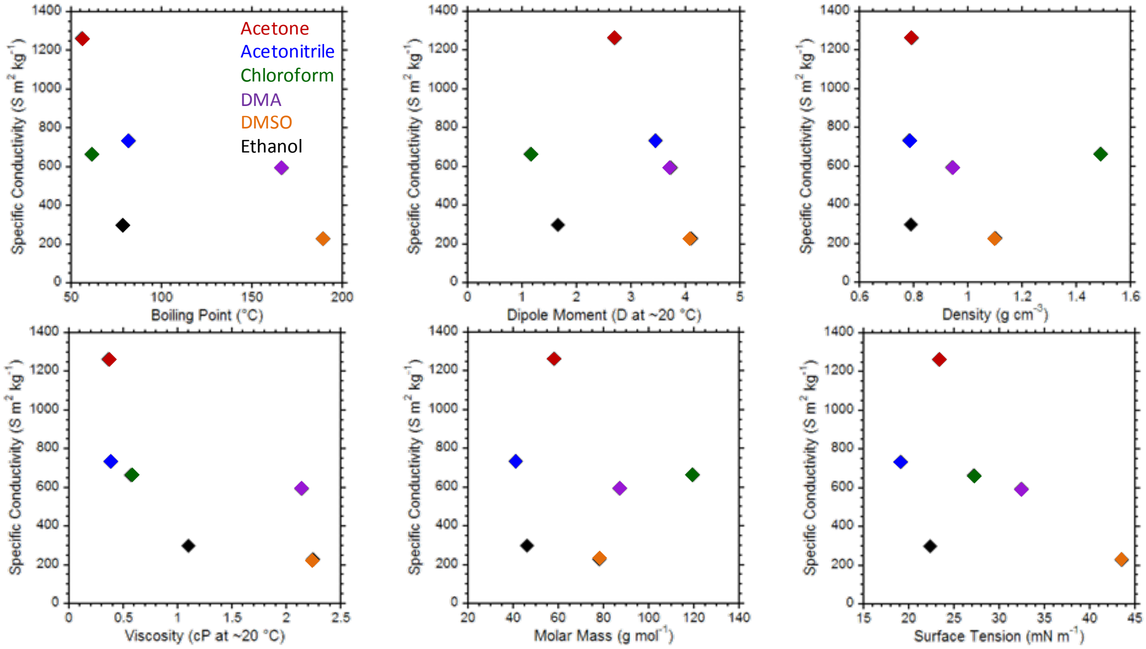

Figure 11. Specific conductivity data from Figure 10 plotted vs (a) boiling point, (b) dipole moment, (c) density, (d) viscosity, (e) molar mass, and (f) surface tension.

3.3.2 Design of Experiments Approach

Due to the large number of factors available for optimization in the extrusion process, methodologies from Design of experiments (DoE) have been employed to reduce the number of samples required and to resolve the interactions between factors. A combined mixture-process DoE study was conducted which enables determination of the effect on specific conductivity of blends of solvents for the coagulant bath and the temperature of the coagulant bath. Coagulant bath temperature had previously been unexplored. To construct the experimental sample space, eight points on a ternary mixture plot were selected. Acetone and ethanol were selected from the study in Figure 10 to represent high and low performance coagulant baths. Chloroform was also used in the blends as a middle performance coagulant. The ternary mixture designs were then replicated at 0 °C, 25 °C, and 50 °C to determine the effect of coagulant temperature and if there is curvature (a temperature squared term) in this effect. This design is depicted in Figure 12, where each red rectangle and grey point represents the experimental conditions under which an extrusion was conducted. The grey points indicate that the resulting wire was too non-uniform to measure a specific conductivity. The numbers inside the red boxes are the specific conductivities of the wire extruded under those conditions in S m^2 kg^{-1}.

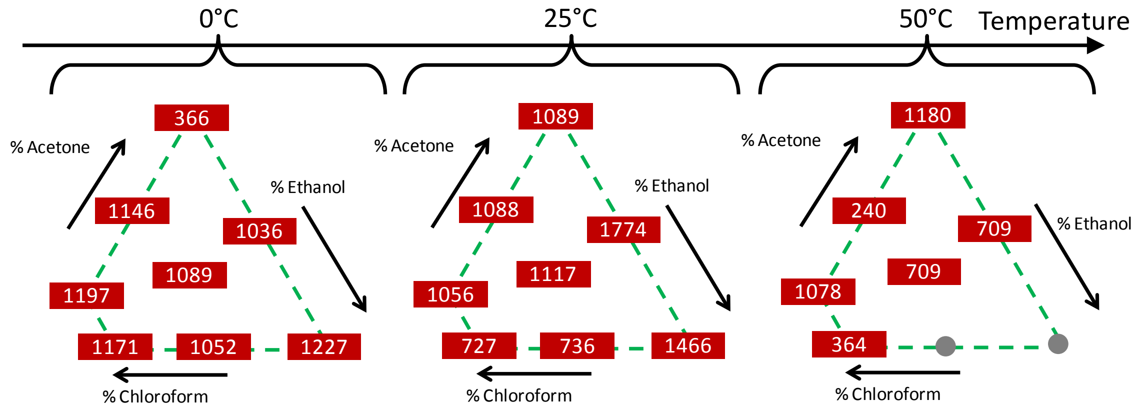

Figure 12. Experimental results from conducting a combined mixture-process designed experiment which varied both mixtures of acetone, ethanol, and chloroform; and temperature. Results are listed as specific conductivity in units of S m^2 kg^{-1}.

The resulting data was analyzed by transforming the three mixture components (which are not linearly independent due to the constraint that the sum of their volume fractions must be 1) into two linearly independent terms. These two terms, along with the temperature term, were analyzed using a regression model with the three factors, their squares, and their products (for a total of 9 terms plus a constant) as predictors. None of the factors were found to be statistically significant, indicating that the best predictor of specific conductivity for an extruded wire within this sample space is the average specific conductivity of the entire sample set. Regardless, the resulting regression model was used to predict operating parameters which might lead to the highest specific conductivity extruded wires. The regression model predicted highest specific conductivity at 13 °C, and the model predictions at this temperature are available in Figure 13. The optimal combination of coagulants is 14 % acetone in 85 % ethanol at 13 °C with a predicted specific conductivity of 1400 S m^2 kg^{-1}. An extrusion was conducted under these conditions and had a measured specific conductivity of 1600 S m^2 kg^{-1}, outside the prediction interval but higher than any other specific conductivity measured in this study. This indicates that the DoE methodology was useful in this context for determining regions of interest in this design space, but that the extrusion process has too many noise factors at this time for accurate prediction by regression modeling.

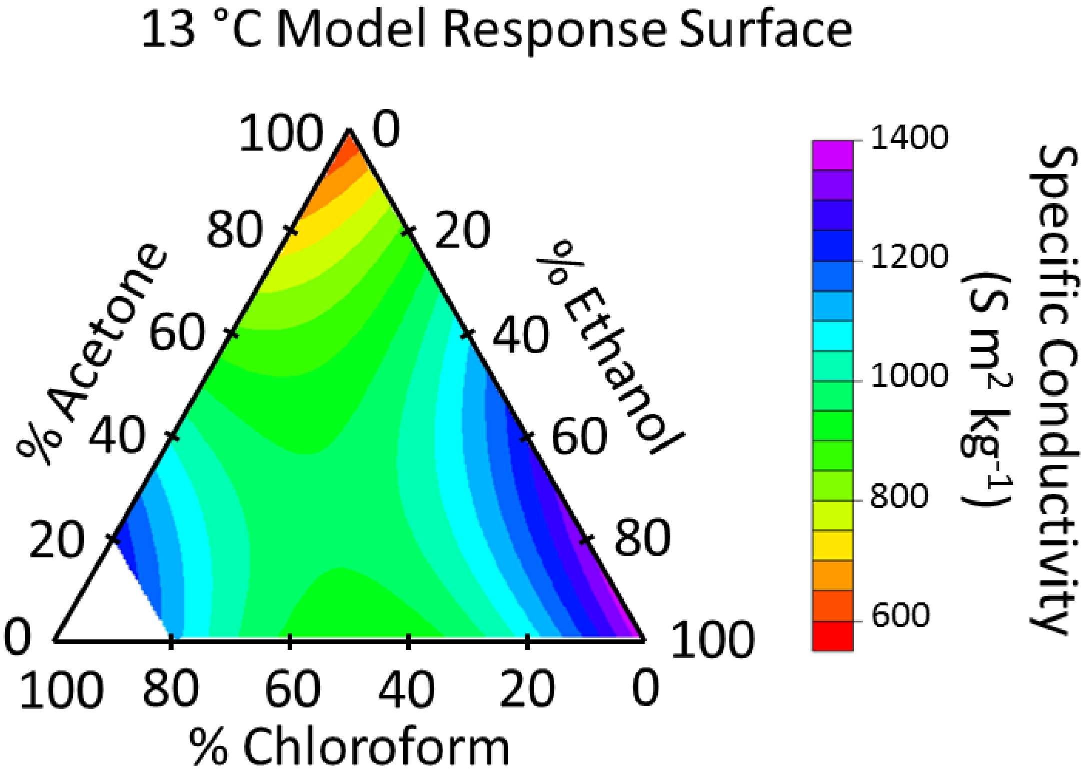

Figure 13. Modeled response surface resulting from regression analysis of the experimental data in Figure 12.

3.4 Mechanical Tension Processing

Mechanical tensioning, or physical stretching, is a technique employed in both metallurgy and polymer processing to induce alignment and ordering at the molecular and nanoscale level. Since CNT wires elongate under stress before breaking, mechanical tensioning of extruded SWCNT wires can be used to alter wire morphology, possibly reducing diameter and mass per length, changing wire uniformity, and altering electrical and mechanical properties by influencing inter-tube contacts and alignment. The mechanical tension used to strain extruded SWCNT wires can be induced at several points during the wire fabrication process as described in the following sections. Exploring the potential of mechanical tension processing to alter and improve wire performance is a goal of the proposed research.

3.4.1 Strain Induced During Wire Coagulation

SWCNT wires can be extruded vertically, with the extrusion tip fixed at the top of a coagulant bath several cm in depth. The extruded SWCNT-CSA dispersion then sinks from the extrusion tip to the bottom of the coagulant bath and comes to a rest on the surface of the containing vessel. The weight of the sinking coagulating wire induces mechanical tension on the SWCNT-CSA dispersion as it exits the extrusion tip. The amount of tension induced in this manner can then be controlled by varying the depth of the coagulant bath used (Figure 14). Wires were extruded into several coagulant baths from 4-30 cm deep and characterized by specific conductivity to determine a trend or optimal coagulant bath depth.

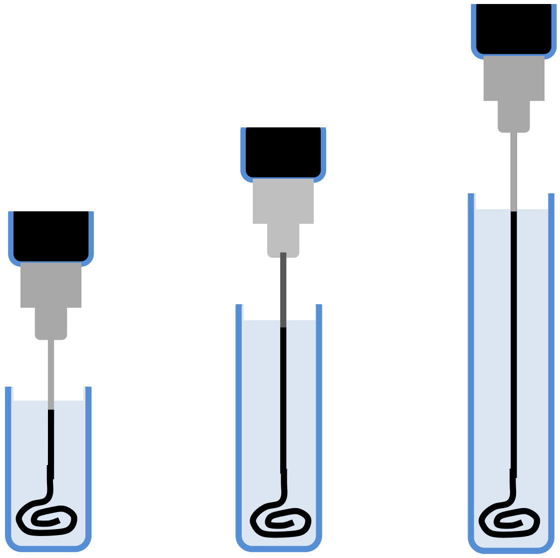

Figure 14. Schematic of the extrusion process and the method which will be used to induce increasing degrees of tension on the coagulating SWCNT-CSA dispersion.

The results from extrusions conducted from the top of coagulant vessels of varying depths, shown in Figure 15, demonstrate a positive correlation between coagulant bath depth and improved wire mechanical and electrical properties with a 25.5 cm increase in the depth of the coagulant bath resulting in a 35% increase in specific conductivity. Vertical extrusion allows for the weight of the coagulating wire to induce mechanical tension on the SWCNT dispersion as it exits the syringe needle. Extrusion into deeper coagulant baths promotes a longer segment of coagulated wire to contribute to this weight, thus inducing greater mechanical tension. The additional tensioning of the coagulating wire causes the wire to solidify in a highly uniform and crystalline structure, improving both mechanical and electrical properties.

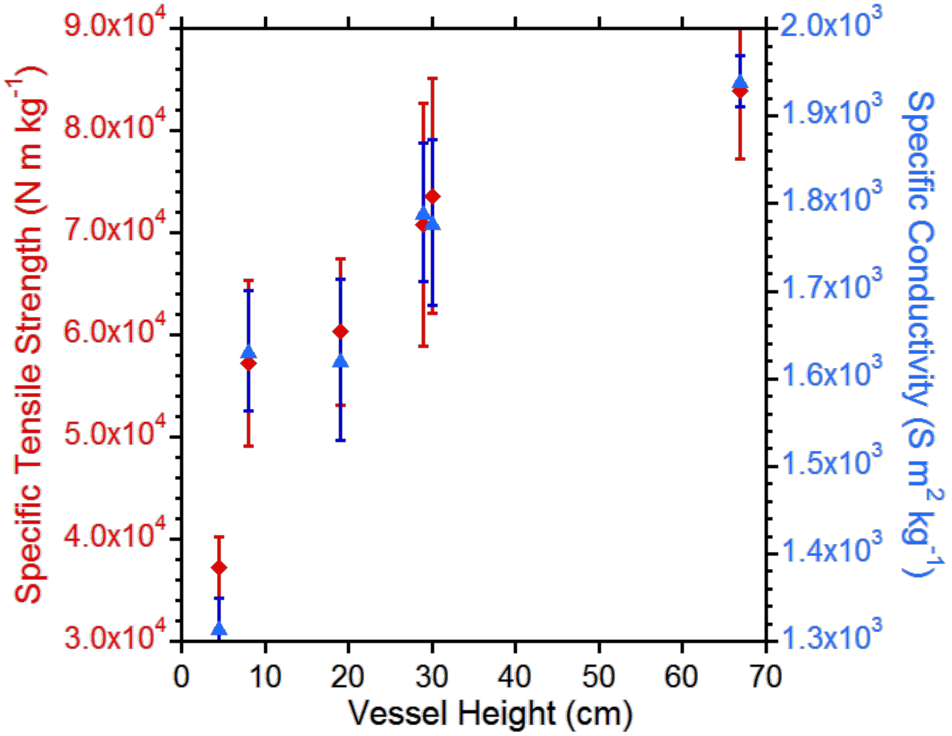

Figure 15. Specific conductivity and specific tensile strength of SWCNT wires extruded into coagulant baths of varying depths. Error bars are the standard deviation in 5 replicate samples.

3.4.2 Post-Extrusion Wire Straining

In addition to the coagulant bath optimization, an *ex situ* post processing technique utilizing a fixed mechanical strain of 5% prior to and during the drying process was employed at room temperature for 15 min on wires extruded from purified SWCNT-CSA dispersions into acetone coagulant baths with a depth of 30 cm. After drying, the wires do not contract to their original lengths. The *ex situ* mechanically strained segments have higher maximum specific conductivity (2200 S m^2 kg^{-1}) than those extruded into shallower acetone baths without mechanical straining (1300 S m^2 kg^{-1}). The highest specific conductivity segments have been analyzed *via* SEM and exhibit a ribbon-like morphology (see Figure 16a). The cross-section is estimated to be rectangular in geometry, and results in a calculated area ranging from 1200 - 1500 μm^2 (Figure 16a). Based upon this cross-section and the measured electrical resistance, the conductivity of the post-processed SWCNT wires ranges from $4.1\text{-}5.0\times10^6$ S/m with a tensile strength ranging from 210-250 MPa. The combination of both *in situ* and *ex situ* mechanical tensioning has created SWCNT wires that exhibit highly aligned and dense bundles on their surfaces (Figure 16b). Several continuous meters of wire have been extruded under these conditions with consistent wire properties (Figure 16c). Figure 5d compares the electrical conductivity and tensile strength range for the wires in the present study to recently published extruded CNT wires at room temperature [52], [53], [73]. Thus, the use of high purity laser-synthesized SWCNTs in CSA extruded wires, based upon optimized extrusion and post-processing conditions, leads to marked improvement in bulk SWCNT conductivity. The tensile strength is lower in the present wires than those in reference [53], which may be attributed to the shorter lengths of laser vaporization synthesized SWCNTs than the few-walled CNTs used in that study. The coagulation dynamics based on coagulant selection and coagulant bath depth are a critical aspect affecting CNT wire crystallinity and multi-functionality performance, and may be further improved with additional understanding of the interactions between extrusion factors.

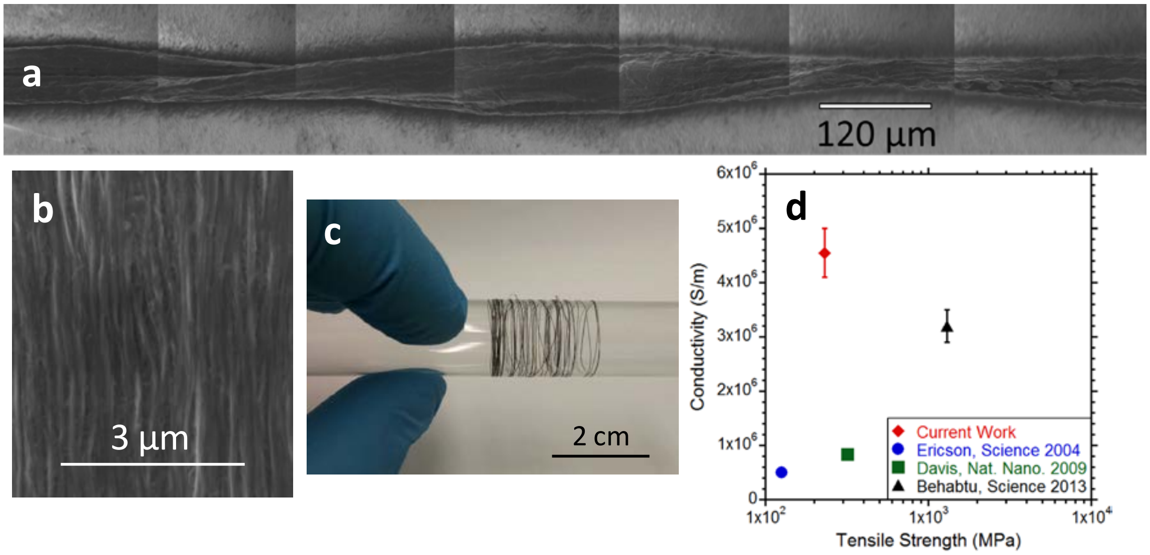

Figure 16. (a) SEM image of wire extruded into 30 cm deep, room temperature acetone bath and then mechanically strained while drying which yielded a conductivity of 4.1-5.0×10^6 S/m. (b) Higher magnification SEM image showing the aligned nature of SWCNT bundles on the surface of the wire in (a). (c) Spool of several continuous meters of wire in (a). (d) Comparison of the electrical and mechanical properties of wires extruded from purified laser SWCNTs to other CNT wires produced from similar wet-spinning techniques used in [47], [52], [53].

3.5 Extruded Laser-Vaporized SWCNT Wire Conclusions

Bulk wires of pure SWCNTs produced by laser vaporization were successfully fabricated using a CSA dispersion and extrusion technique. Extrusions were conducted from CSA-SWCNT dispersions made using either AP-SWCNT material directly from the reactor or purified SWCNT material. Wires made using the purified SWCNT material had specific conductivities two orders of magnitude higher than those made from AP-SWCNTs indicating that the purity of SWCNT material used greatly impacts the resulting wire performance due to impurities preventing coagulation of crystalline bundles of SWCNTs. Different liquids were surveyed for their use as coagulants in the extrusion process with each coagulant yielding unique wire morphologies. Coagulants such as acetone and acetonitrile, which yielded highly uniform wires with visibly aligned bundles on their surface, resulted in the highest mechanical and electrical properties. In addition to the choice of coagulant bath composition having a direct impact on the resulting wire performance, an increase in the depth of the coagulant bath used in the vertical extrusion setup was found to influence the resulting wires properties. Increased coagulant bath depth induced greater mechanical tension on the CSA-SWCNT dispersion as it coagulated and formed more uniform, higher specific conductivity wires. Mechanical straining of the wire segments prior to the coagulant evaporating resulted in wires with the highest room temperature, CSA-doped conductivity to date. Greater understanding of the coagulation factors impacting SWCNT coagulation and ordering will allow for design and engineering of CNT wires, which may replace metal conductors for power and data cable applications.

Chapter 4. Engineering Factors Influencing Extruded Wire Fabrication

4.1 Introduction to Additional Factors Available

Tasks:

- Compare the performance of extruded laser-SWCNT wires to extruded wires made from other CNT types.
- Investigate and optimize blends of multiple CNT types in CSA dispersions for improved wire multifunctionality.
- Study how modified laser synthesis parameters impact extruded wire properties.
- Demonstrate the effects of varying extrusion parameters on the performance of extruded SWCNT wires.

As depicted in Figure 6, there are a number of factors in the wire extrusion process available for modification. In the previous chapter, high-conductivity CNT wires were fabricated by using high-purity SWCNTs from laser vaporization, tailoring the coagulant composition and temperature, and introducing in-situ and post-processing tension to impact the uniformity of and alignment in the extruded wire. Several additional factors were investigated and results are presented in this chapter (Figure 17). These factors include the type of CNT material used for dispersion and extrusion to evaluate the performance of commercially available CNT materials and factors that impact the dynamics of the CNT-CSA dispersion as it is introduced into the coagulant bath. It is instructive to conduct these optimizations one at a time due to the variability involved which can render designed experiments with insufficient replicates inconclusive.

Factors that impact the dynamics of the CNT-CSA dispersion introduction into the coagulant bath include the syringe needle diameter. The diameter of the extrusion spinneret opening influences the volume of dispersion entering the coagulant. Larger volumes may experience different coagulation dynamics due to greater distances required for CSA/coagulant diffusion or more uniform flow in the interior volume of extruded dispersion. This diameter is controlled by selecting different gauge syringe needles for extrusion. Adjustment of the extrusion rate, in terms of the volume of dispersion introduced into the coagulant bath per unit time, may alter resulting wire properties. This is an important factor to study to determine if extrusions conducted by hand using a syringe, which may have small variations in extrusion rate, could have confounded the results of other studies. Extrusion rate will be controlled though the use of a mechanized syringe pump. The syringe needle length is also varied by cutting syringe needles to various lengths, and extrusion through polytetrafluoroethylene spinnerets are conducted. Extrusions conducted through an air-gap between the syringe needle opening and the coagulant bath surface are conducted in an effort to introduce greater in-situ wire tensioning.

Concentric coagulant flow is experimented with by using coaxial syringe needles that allow for coagulant to be pumped through an outer outlet while the SWCNT-CSA dispersion is pumped through the inner outlet. Multiple coagulant flow rates are investigated as are various diameter coaxial syringes. Coagulant bath temperature is investigated again using a one-factor-at-a-time approach and temperatures below 0 °C are achieved using dry ice baths. Factors which strongly influence extruded wire performance are selected and high conductivity wires are fabricated using these conditions. Calendering is employed to densify the resulting wires.

Finally, this chapter concludes with the construction of an automated extrusion apparatus. The apparatus is designed and built to accommodate improvements and interchange between extrusion processing conditions easily. The modular design of the apparatus is a feature meant to easily incorporate the results of future studies that identify in-line processes that impact wire performance.

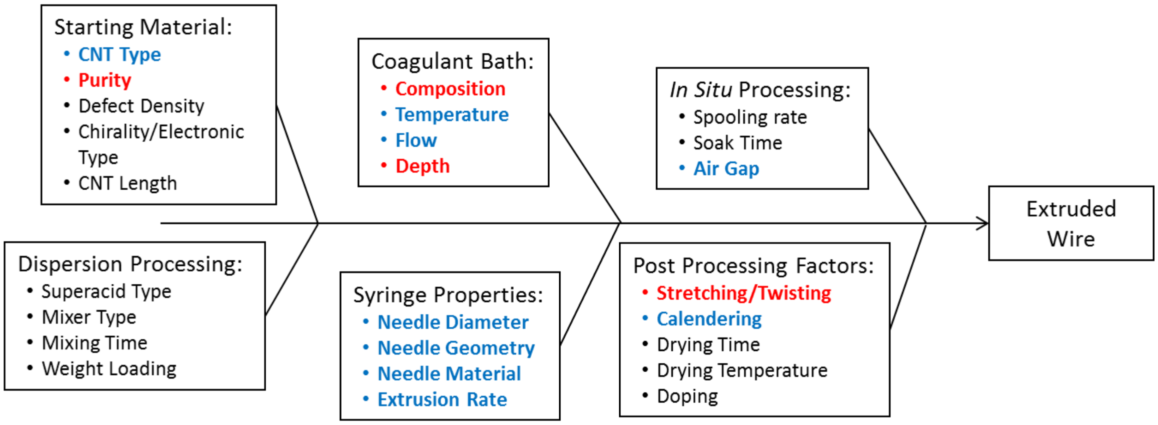

Figure 17. Process diagram of factors impacting extruded wire performance, with factors investigated in this chapter highlighted in blue, and factors investigated in Chapter 3 highlighted in red.

4.2 Carbon Nanotube Types for Extruded Wires

4.2.1 Commercially-Sourced Carbon Nanotube Materials

In the previous chapter, laser vaporization SWCNTs were explored due to their high conductivity and the lack of existing data on extruded wires of this type. Many other types of CNTs exist, as discussed in Chapter 1, which may be suitable for CSA dispersion and extrusion. Benefits of optimizing the extrusion process with other CNT types may include reduced costs, commercial availability, and increased tensile strength. CNT types of interest for experimentation with extrusion include arc SWCNTs and CVD SWCNTs of varying length, diameter, and number of walls.

Extrusions were conducted from dispersions of purified HiPco SWCNTs (which have been explored in refs [47], [52]) for comparison to laser SWCNT extruded wires, with the resulting wires shown in Figure 18. The HiPco SWCNT extruded wires had lower specific conductivity and tensile strength than the laser SWCNT wires extruded under the same conditions (Figure 19). Because the performance of the HiPco extruded wires did not match that of HiPco extruded wires in refs [47], [52], it is likely the extrusion set up used can be further improved.

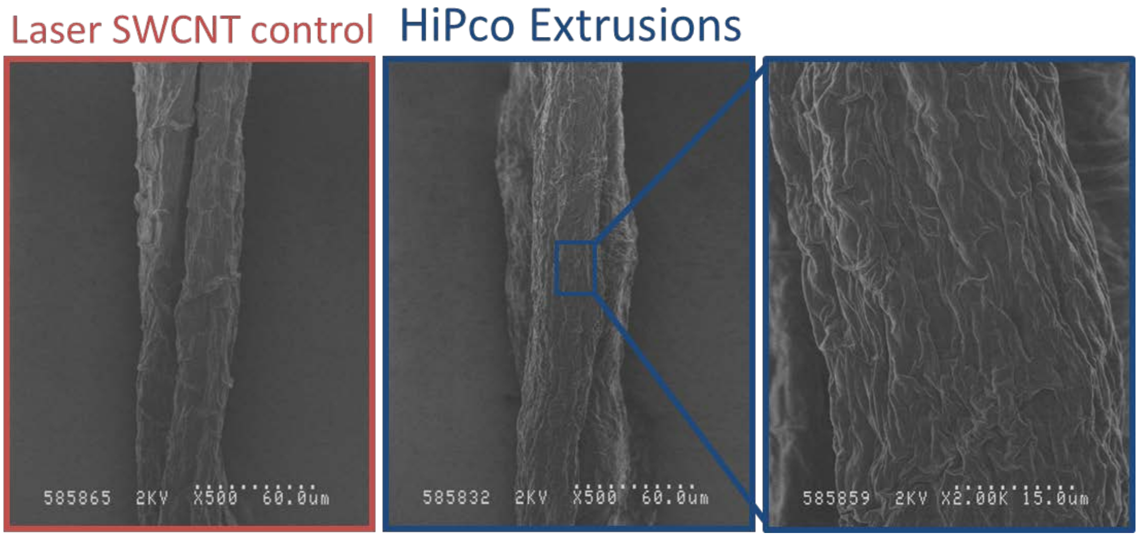

Figure 18. SEM images of (a) extruded wire made from purified laser SWCNT-CSA dispersion, and (b) extruded wire made from purified HiPco SWCNT-CSA

dispersion under the same extrusion conditions. (c) higher magnification image of the surface of the wire in (b).

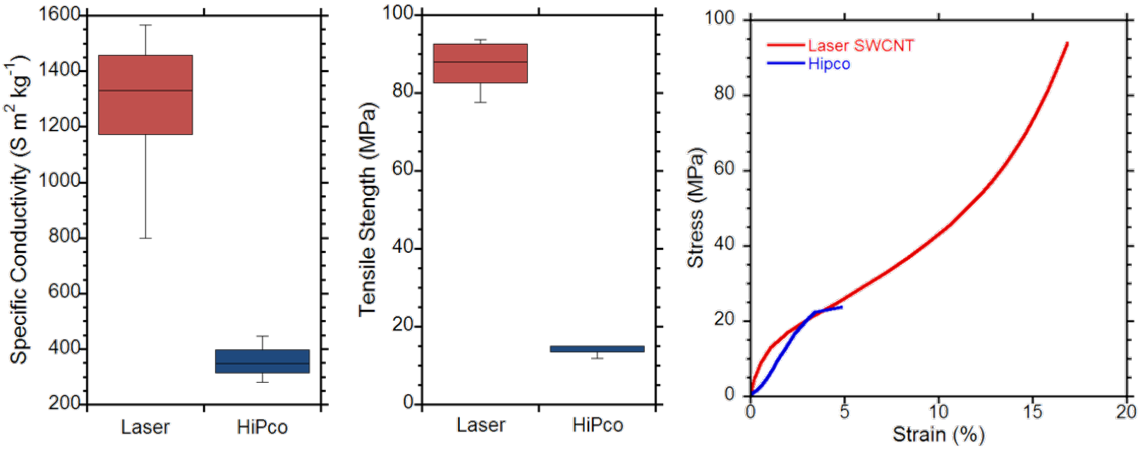

Figure 19. (a) Boxplot of 5 specific conductivity measurements from laser and HiPco SWCNT extruded wires. (b) Boxplot of 5 tensile strength measurements from laser and HiPco SWCNT extruded wires. (c) Representative Stress-Strain curves for HiPco and laser SWCNT extruded wires.

Another CNT material of interest is the commercially available NCTI CNT sheet material. As a preliminary study, this sheet material was purified with a 560 °C thermal oxidation, concentrated HCl rinse, and subsequent 560 °C thermal oxidation. 5 mg of the purified NCTI material per ml of CSA was then added to a 35 mg/ml laser SWCNT in CSA dispersion. The resulting wires can be seen in panels a and b of Figure 20, displaying the width and thickness of these ribbon-like wires respectively. The specific conductivity and specific strength of the hybrid wires was lower than that of wires extruded from a dispersion of 40 mg/ml laser SWCNTs (Figure 20c and d respectively). This may be due to poor dispersion of the NCTI CNTs, since it is difficult to assess material breakup with pre-dispersed material in the CSA. Future studies of hybrid dispersions will thus combine multiple dispersions for better determination of dispersion homogeneity.

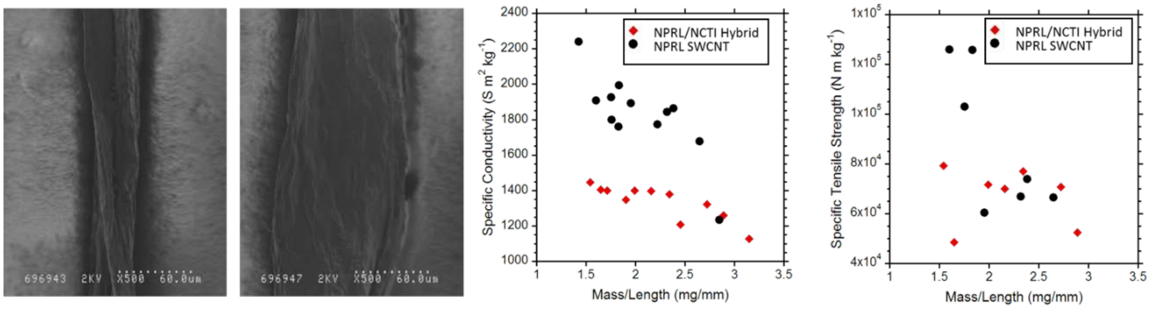

Figure 20. (a) and (b) SEM images of extruded wires made from a dispersion containing both purified laser SWCNTs and purified NCTI CNTs. (c) Specific conductivity measurements on these wires and extruded wires of only purified laser SWCNTs as a control. (d) Specific tensile strength measurements on these wires and extruded wires of only purified laser SWCNTs as a control.

Fabrication of CNT wires using double-walled carbon nanotubes (DWCNTs) was tested since the concentric format of the DWCNTs may allow for an increase in the number of SWCNT conductors without increasing the bundle size. To test this hypothesis, DWCNTs were purchased from SkySpring Nanomaterials. An SEM image of the as-purchased DWCNT material can be seen in Figure 21a. The as-purchased DWCNT material was purified by a 520 °C thermal oxidation at a 10 °C/min ramp rate, followed by mixing the resulting powder material into concentrated HCl and filtering and rinsing with deionized water. This thermal oxidation and acid treatment was repeated a second time on the resulting filter cake. An SEM of the resulting material can be seen in Figure 21b, and some impurities can still be observed. The purified DWCNT material was then dispersed in CSA at a weight loading of 67.9 mg/mL, a concentration which provided a similar level of viscosity as a 40-50 mg/mL dispersion of SWCNTs from laser vaporization synthesis in CSA. The DWCNT-CSA dispersion was extruded through a 20 Ga syringe needle at 0.1 mL/min into the top of a 2 °C acetone bath 28 cm deep. Upon loading the syringe with DWCNT-CSA dispersion, a much greater tendency to form long liquid strands as it spilled over from a microspoon. Depression of the syringe plunger was also noted to require much greater force than typically required when the syringe is loaded with a SWCNT-CSA dispersion. The resulting DWCNT wires were uniform as seen in the side-on SEM image in Figure 21c. The resulting specific conductivity was on average 1100 S m^2 kg^{-1}. The low specific conductivity of these wires may be due to the presence of impurities in these wires, preventing ideal packing and alignment of the DWCNTs as seen in the side-on SEM in Figure 21d. Cross-sectional SEM images of laser-cut wire segments such as those displayed in Figure 21e and f show that these wires have the same layered morphology of SWCNT extruded wires and were used to determine the wire cross-sectional area and calculate an average conductivity of 1.4 MS/m. High conductivities have been achieved in DWCNT extrusions in the literature [53]. Conductivity improvements in the extruded DWCNT wires presented here will likely come from improved purification techniques for these materials and optimization of the type (diameter, length, defect density) of the constituent DWCNTs.

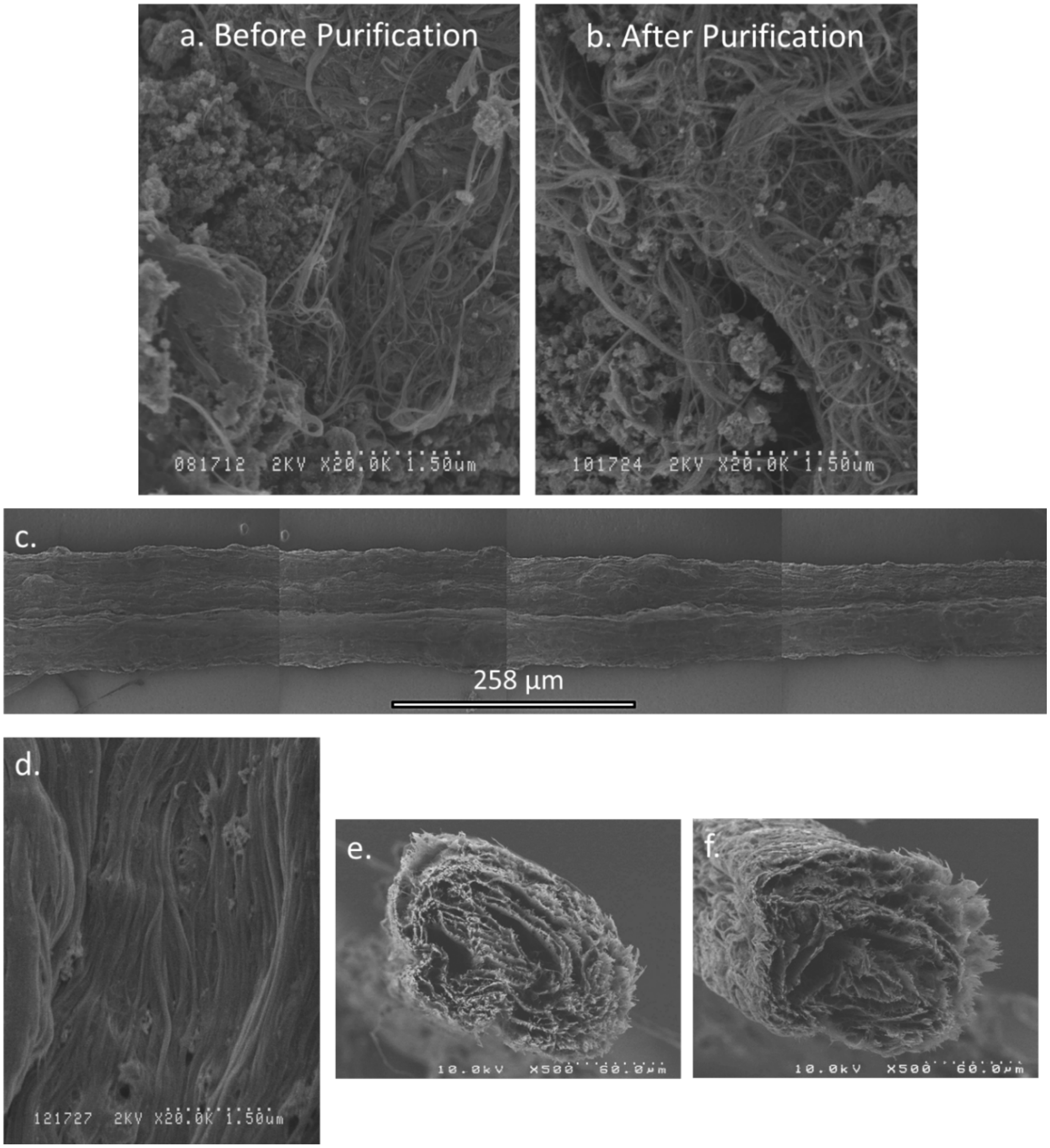

Figure 21. Characterization of DWCNTs and DWCNT extruded wires. a. SEM image of powdered, as-purchased DWCNTs. b. SEM image of DWCNTs after 560 °C thermal oxidation, HCl treatment, a second 560 °C thermal oxidation, and a second HCl treatment. c. Multiple SEM images stitched together of an extruded wire made from purified DWCNTs. d. High-magnification SEM image of DWCNT

extruded wire with the wire axis mounted vertically. e and f. Cross-sectional SEM images of two laser-cut DWCNT extruded wire segments.

4.2.2 Modified Laser Synthesis Parameters

Modification of the temperature, pressure, and carrier gas during laser SWCNT synthesis impacts physical properties of the resulting CNTs and provides a different distribution of SWCNT diameters [22]. This fact can be used to obtain laser SWCNT samples with different properties which can be purified and dispersed in CSA. Wires can be extruded from these dispersions to determine the effect of diameter distribution on the electrical and mechanical properties of CNT structures.

Figure 22a shows historical data of the radial breathing modes of SWCNT samples synthesized via laser vaporization under the specified ambient gasses at 1150 °C and 900 °C. The peak positions in the RBMs can be used to quantify the diameter ranges for SWCNTs in the sample using the relationship in equation (6), where ω_r is the wavenumber of a peak in the RBMs (in cm^{-1}), and d is the SWCNT diameter in nm [61].

$$\omega_r = \frac{223.75}{d} \tag{6}$$

The diameter of a SWCNT impacts its conductivity in the axial direction by reducing its cross-sectional area while theoretically maintaining its quantized conductance [74], [75]. Figure 22b demonstrates the effect of this principle, by plotting the conductivity of a SWCNT bundle versus the diameter of the constituent SWCNTs. Overlaid in this figure are the potential ranges of SWCNT diameters that can be produced from the use of nitrogen and argon carrier gasses during laser vaporization synthesis.

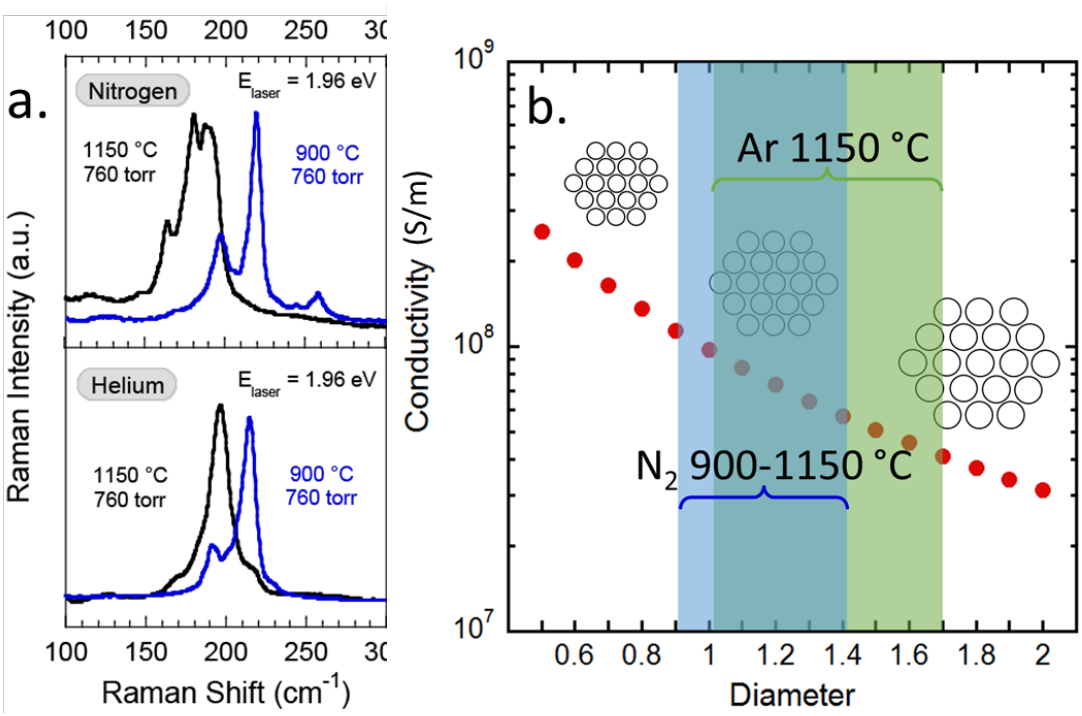

Figure 22. a. Raman spectroscopy of products of SWCNT synthesis run at 1150 (black) and 900 °C (blue) in nitrogen (top) and 1150 (black) and 900 °C (blue) in helium (bottom). b. plot of SWCNT diameter and the conductivity of an ideal bundle of SWCNTs with that diameter (red data points). Inset diagrams demonstrate the effect of SWCNT diameter on bundle size. Blue and green bands demonstrate the diameter ranges possible from SWCNT synthesis under nitrogen at 900-1150 °C and Argon at 1150 °C, respectively.

Experimental work was conducted to determine the practical effects of changing carrier gas type and temperature on the conductivity of extruded SWCNT wires. Nitrogen was selected as a carrier gas for comparison to the standard argon-synthesized SWCNTs. SWCNTs were synthesized at 900, 1000, and 1100 °C under nitrogen and refluxed overnight using the standard procedure for argon-synthesized SWCNTs. SEMs of the resulting SWCNT papers from filtration and rinsing of the refluxed synthesis products can be seen in Figure 23 panels a, b, and c. After refluxing, few SWCNTs were visible in the sample synthesized at 900 °C in panel a. TGA was conducted on these samples and the % weight loss per degree C is shown in Figure 23d. A double peak in this derivative is visible for the samples synthesized at 1000 and 1100 °C, while only a single peak in seen at ~540 °C for the sample synthesized at 900 °C. The absence of a second peak in the TGA data and the low-visibility of SWCNT content in the SEMs indicate that the sample synthesized at 900 °C is of insufficient purity for further purification and use in extruded wire fabrication. Raman spectroscopy analysis of the samples synthesized at 1000 and 1100 °C in nitrogen was also conducted and the RBMs are displayed in Figure 23e along with the RBM Raman spectra from a sample of purified SWCNTs synthesized in 1125 °C argon for comparison. The peaks in the spectra indicate that the ranges of SWCNT diameters present in each sample are from 1.1 to 1.7 nm for SWCNTs synthesized in argon at 1120 °C, from 1.0 to 1.5 nm SWCNTs synthesized in nitrogen at 1100 °C, and from 0.9 to 1.3 nm for SWCNTs synthesized in nitrogen at 1000 °C. Therefore, SWCNTs synthesized in nitrogen at 1000 °C were selected for future study in extruded SWCNT wiring due to their sufficient purity for material handling and there greater dissimilarity in diameter range from standard SWCNTs synthesized in argon at 1125 °C than SWCNTs synthesized in nitrogen at 1100 °C.

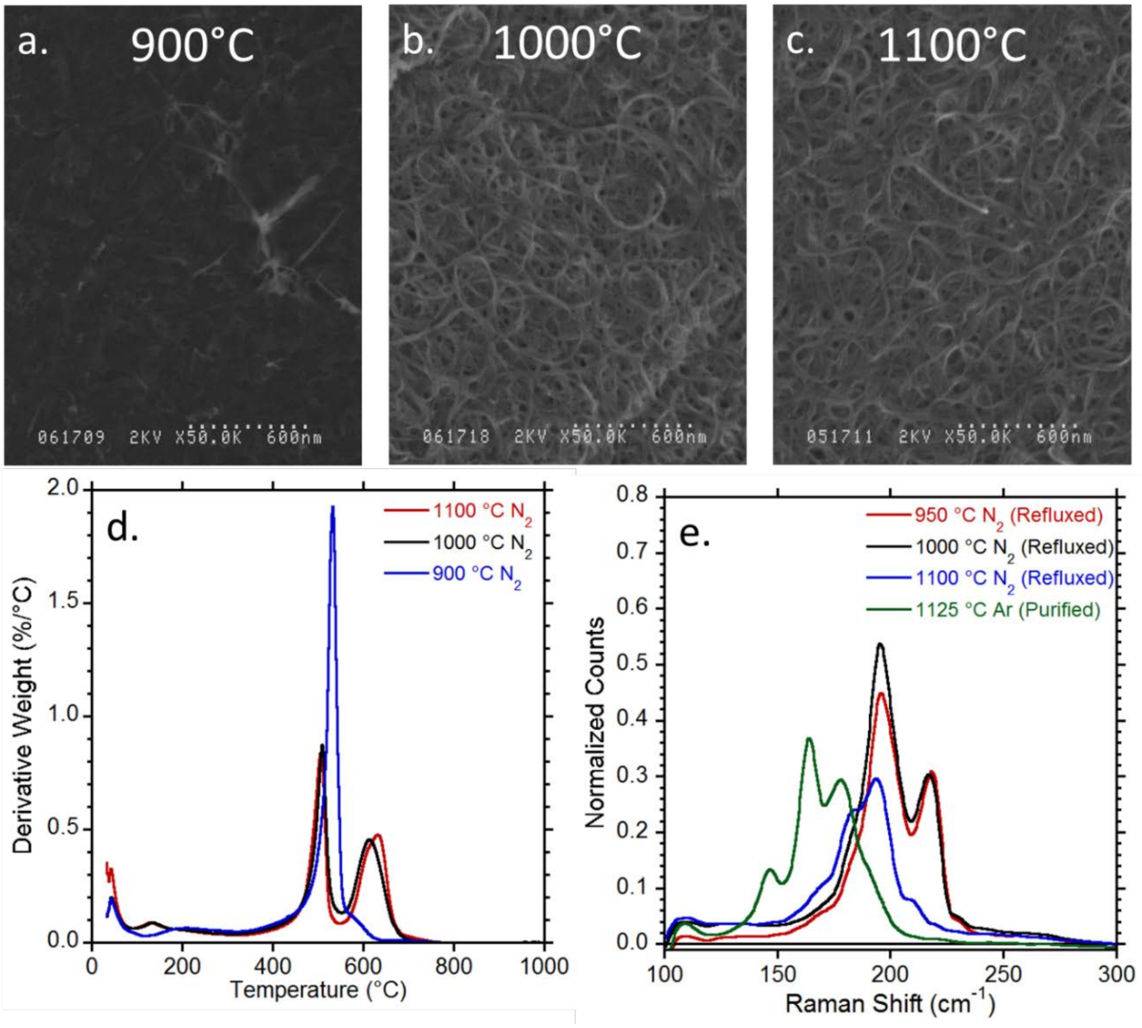

Figure 23. a, b, and c. SEM images of SWCNTs synthesized under nitrogen carrier gas at each of the labeled temperatures in a sheet format after acid refluxing. d. Derivative weight (change in mass per degree Celsius) as a function of temperature from thermogravimetric analysis of refluxed SWCNTs in sheet format synthesized under nitrogen at various temperatures. e. Raman spectroscopy of the radial breathing modes of refluxed SWCNTs in sheet format synthesized under nitrogen at various temperatures.

SWCNT samples synthesized in nitrogen at 1100 °C underwent additional purification after reflux and filtration before dispersion and extrusion. A thermal oxidation was used to remove non-SWCNT carbonaceous impurities. The temperature of this thermal oxidation was determined from the TGA data in Figure 23d where the minima between peaks occurs at ~560 °C, the same temperature used in the standard purification procedure used for SWCNTs synthesized in argon at 1125 °C. Thermal oxidation was followed by a concentrated HCl soak and deionized water rinse. The purified SWCNTs were then dried overnight in a vacuum oven before dispersing in CSA at 45 mg/ml following the standard procedure outlined in section 3.2. Extrusions of this dispersion and a 45 mg/ml dispersion of SWCNTs synthesized in argon at 1125 °C were conducted at a rate of 0.1 ml/min though 22 Ga syringe needles into -10 °C acetone baths that were 30 cm deep. The morphology of the resulting wires is compared in Figure 24. Panels a and b are stitched SEM images showing the macroscale morphology of the two wires. Both display a high degree of uniformity, and panels c and f show a high degree of alignment (wire axis is vertical in these images). Cross-sectional SEMs of laser-cut wires are shown in Figure 24d and e, and were used to calculate the cross-sectional areas of these wires. Electrical measurements and cross-sectional areas were used to calculate the conductivity of these wires and results of this characterization are catalogued in Table 1.

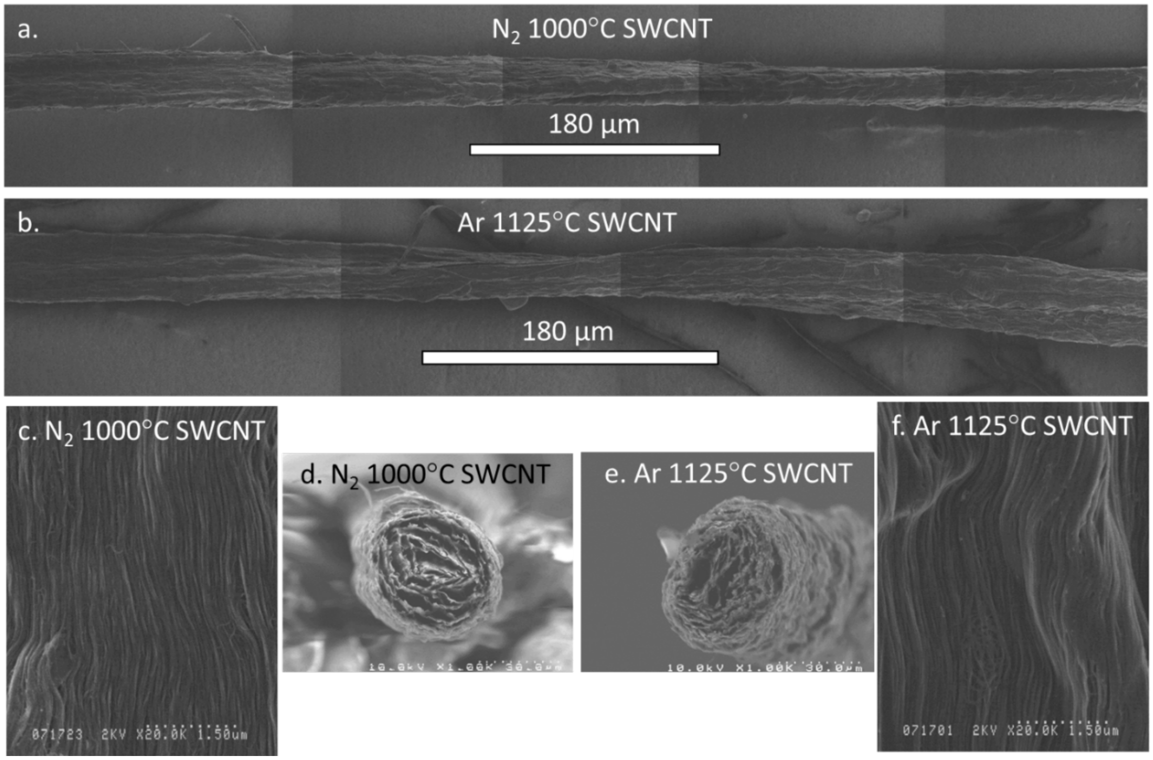

Figure 24. Characterization of wires extruded from 45 mg/mL dispersions of either purified SWCNTs synthesized under 1000 °C nitrogen or 1125 °C. a and b. Side-on SEM images with the wires mounted horizontally and with a slight twist to show all sides. c and f. High-magnification SEM images of the surfaces of both wires with the wire axis oriented vertically. d and e. Cross-sectional SEMs of laser-cut sections of each wire.

The performance of both wires fabricated from SWCNTs synthesized in nitrogen at 1000 °C and SWCNTs synthesized in argon at 1125 °C was similar, conductivities of 1.5 and 1.7 MS/m respectively. The similarity in wire performance many indicate that the differences in the diameter distributions were not large enough for the smaller diameters of SWCNTs synthesized in nitrogen at 1000 °C to significantly enhance conductivity, or that the purification procedure is more effective for the larger diameter SWCNTs synthesized in argon at 1125 °C.

SWCNT Type	**Resistance (Ω/m)**	**Linear Density (mg/m)**	**Specific Conductivity (S m^2/kg)**	**Cross-sectional area (μm^2)**	**Conductivity (MS/m)**
N_2 1000°C	424	1.2	2050	1600	1.5
Ar 1125°C	268	1.7	2220	2200	1.7

Table 1. Electrical properties of wires extruded using SWCNTs synthesized in either nitrogen or argon at 1000 °C or 1125 °C, respectively.

4.3 Extrusion Process Factors Influencing Dispersion Coagulation

Several extrusion design factors influence the dynamics of dispersion coagulation during extrusion. One such factor is the diameter of the syringe needle used. The diameter of the syringe needle determines the diameter of the extruded cylinder of SWCNT-CSA dispersion as it enters the coagulant. This diameter affects the distance the coagulant and the CSA must diffuse in order for solidification to take place. The syringe needle diameter also influence the flow dynamics of the dispersion as it enters the coagulant bath. A series of SWCNT wires were extruded to determine the practical effect of syringe needle diameter on extruded wire specific conductivity. A 40 mg/mL purified SWCNT in CSA dispersion was extruded through 33, 24, and 22 Ga syringe needles (inner diameters 110, 310, and 410 µm, respectively) into a 30 cm deep acetone coagulant bath at room temperature. The resulting wires were characterized and the specific conductivities measured can be seen in Figure 25 as a function of the syringe needle inner diameter used to create them. It is evident that larger diameter syringe needles promote higher conductivity extruded wire fabrication. To determine why, SEM images of samples extruded from each diameter syringe needle are also presented in

Figure 25. From these SEM images, it is apparent that samples extruded from smaller diameter syringe needles contain more void space in their interiors than samples extruded from the larger diameter syringe needles. Void space may be an effect of greater non-uniformities in the dispersion flow, which would also impact alignment of SWCNTs in the wire and reduce specific conductivity.

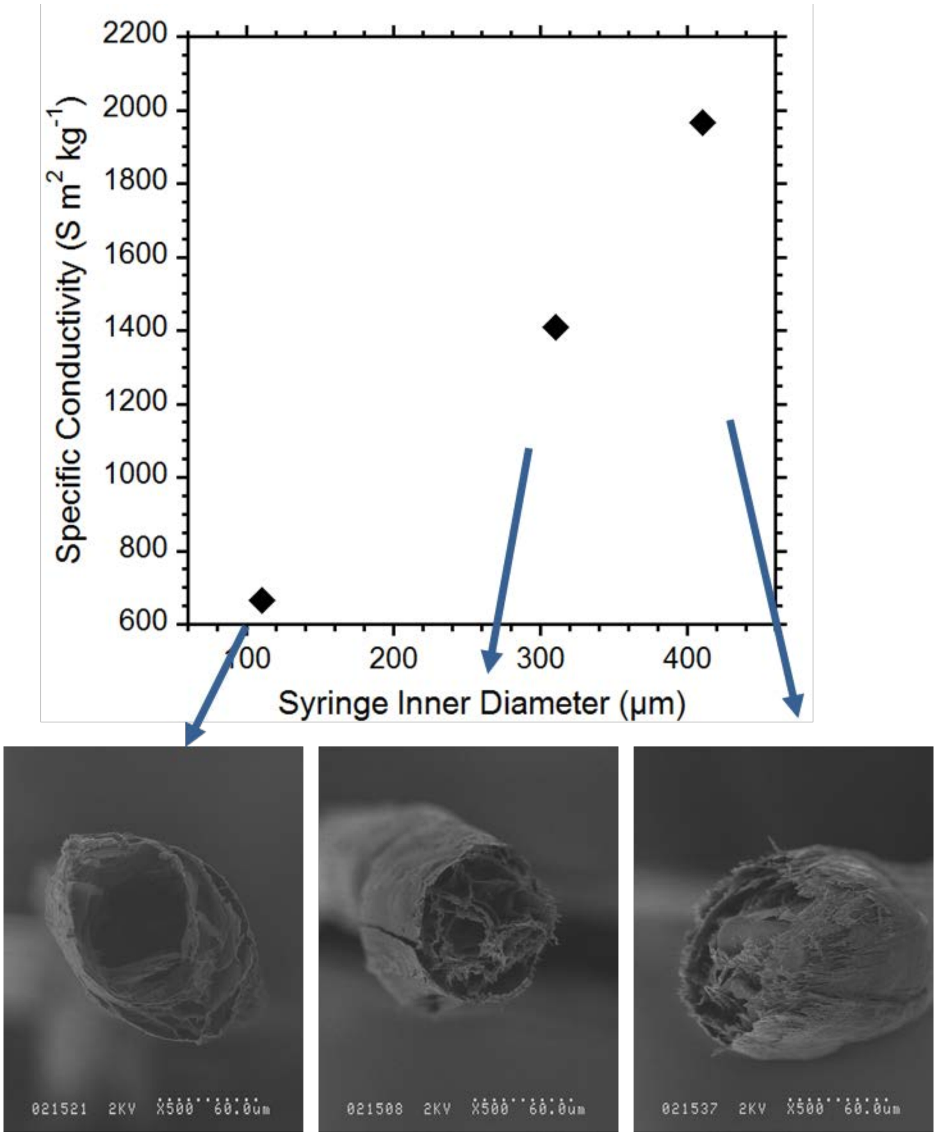

Figure 25. Dependence of wire specific conductivity on syringe diameter with cross-section SEMs of laser-cut samples from each extrusion.

In previous studies, the rate of extrusion was manually controlled by hand. This introduces small variations between sample sets, so if wire performance is sensitive to extrusion rate, this could invalidate previous sample sets. For this study, wires were extruded through a 24 ga syringe into room temperature acetone. The extrusion rate was controlled by loading the syringe into a programmable syringe pump and the rate was varied from 0.05 0.25 ml/min for successive runs. As displayed in Figure 26, the specific conductivity of three replicates at each rate was measured and found to be independent of the extrusion rate, validating previous studies conducted by hand. It was noted however, that the wires extruded by the syringe pump were of higher uniformity than those conducted by hand (as determined by optical microscopy), likely due to the higher uniformity of the extrusion rate when conducted by the pump. This indicates extrusions performed by an automated system when scaled industrially may be of even higher performance than those characterized in 3.4.

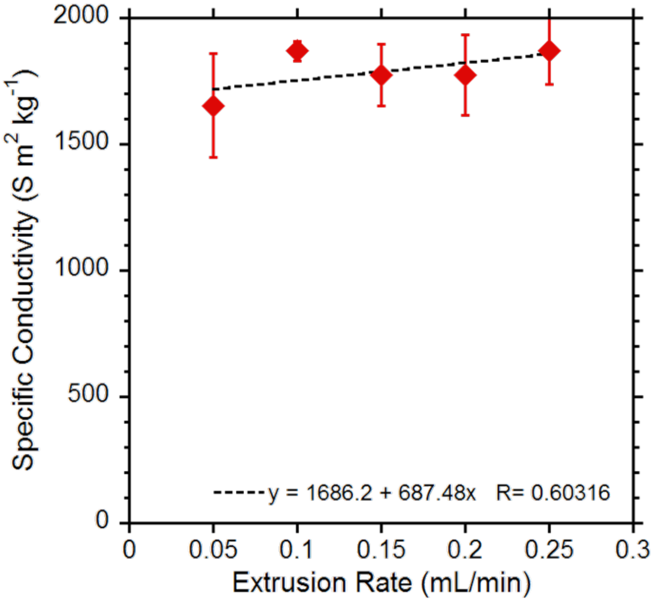

Figure 26. Specific conductivity of extruded SWCNT wires while varying the extrusion rate.

Another property of the syringe that influences coagulation of the dispersion is the length of the syringe needle. Shear and surface forces from the sidewalls of the syringe needle impact the flow of the viscous SWCNT dispersion during extrusion, either aligning the dispersed SWCNTs or causing flow non-uniformities. To determine the effects of syringe needle length, three 22 Ga syringe needles were cut to 1, 16, and 32 mm lengths by threading them with copper wire to prevent deformation and cutting them with a pair of diagonal pliers. The cut tips were gently filed to remove any burring. A 50 mg/ml dispersion of purified SWCNTs in CSA was extruded though each cut syringe needle into a 30 cm deep bath of 12 °C acetone at a rate of 0.1 mL/min. Wires were then stretched and dried under tension. Characterization of the resulting wires can be found in Figure 27. The mass per length and resistance per length of extruded wires depended on the length of the syringe needle used to fabricate them (Figure 27a). Shorter syringe needles produced wires with greater linear density and lower resistance per length than longer syringe needles did. These properties effectively canceled out and yielded wires with specific conductivities independent of syringe needle length as seen in Figure 27b. Tensile properties of these wires were also determined and are presented in Figure 27c. From these stress-strain curves it is apparent that most samples failed between 1 – 3 % strain and the breaking force required increased with decreasing syringe needle length, which is expected as the mass per length also increases with decreasing syringe needle length. The specific conductivities measured in this study were on par with extrusions made from similar conditions with uncut syringe needles, and the conductivities calculated from laser cutting and cross-sectional SEM imaging were similar, with a highest attained value of 3.6 MS/m. These results indicate that high-conductivity extruded SWCNT wires can be produced for any syringe needle length in the rage tested.

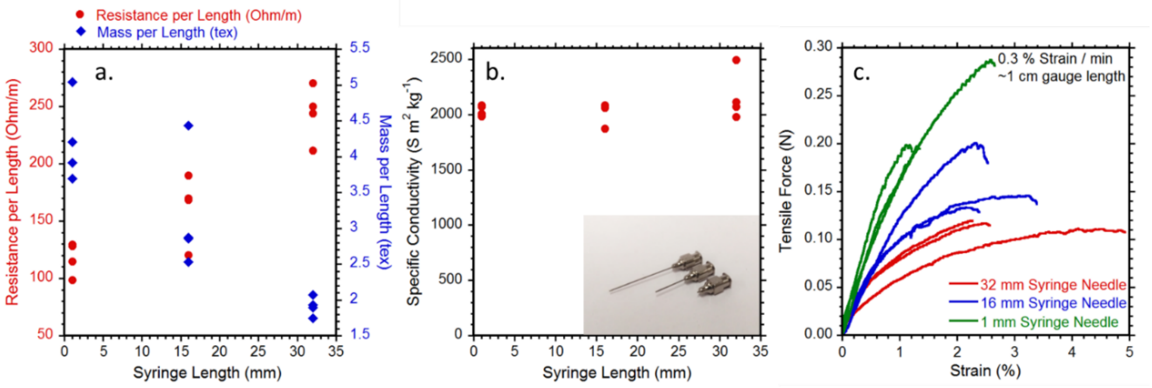

Figure 27. Characterization of wires extruded through 22 Ga syringe needles cut to various lengths. a. Resistance per length (left axis and red circle data points) and linear mass density (right axis and blue diamond data points) of wires extruded from various length syringe needles. b. specific conductivity of the same samples. d. Tensile force as a function of applied strain from 3 replicate samples extruded from each length syringe needle.

While the length of the syringe needle was not found to have a significant effect in the range of the lengths tested, the syringe needle material may play a significant role in alignment of SWCNTs in dispersion during coagulation, impacting wire conductivity. The syringe needle material in all studies thus far has been stainless steel, which has displayed good stability in the presence of CSA. Alternative materials would have different interfacial forces with the SWCNT-CSA dispersion, causing differences in dispersion flow dynamics. To test the effects of this difference, polytetrafluoroethylene (PTFE) tubing was purchased with an inner diameter of ~720 µm. An 8 cm segment of tubing was cut and fitted over a 3.8 cm long stainless steel syringe needle with a ~720 µm outer diameter so that 4.2 cm of tubing extended over the end of the stainless steel syringe needle, as seen in Figure 28a. SWCNT wires were extruded from a 48 mg/mL dispersion of purified SWCNTs in CSA into the top of a 0 °C acetone coagulant bath that was 22 cm deep at a rate of 0.1 ml/min. Wires were then stretched and dried under tension. Optical microscopy of two replicates of the resulting wires can be seen in Figure 28b and c, and displays greater non-uniformity than typically seen in wires extruded without the PTFE tubing in place over the syringe needle. Similarly, an average specific conductivity of 1100 S m^2 kg^{-1} is lower than typically achieved without the PTFE tubing, and lower than the 2040 S m^2 kg^{-1} measured average of control samples produced under the same conditions without the PTFE tubing in place. Laser-cutting and cross-sectional SEM imaging were also conducted and the resulting SEM images can be seen in Figure 28d, e, f, and g. The conductivity calculated from cross-sectional area measurements from these images was on average 0.5 MS/m, only 20% of the conductivity achieved by the control samples fabricated using the same conditions without the PTFE tubing. The low conductivity and specific conductivity of SWCNT wires extruded through PTFE tubing is likely due to the non-uniformity and void space in them. The non-uniformities may be due to the flow dynamics induced from surface interactions between the SWCNT-CSA dispersion and the PTFE tubing, or it may be that the integration of the tubing into the experimental set up hinders the wire uniformity. Flow non-uniformities may be induced at the point where flow expands from the stainless steel syringe with an inner diameter of 410 µm to the inner diameter of the PTFE tubing. Future studies on syringe needle material should employ complete syringe needle replacements to avoid junctions like that previously described in this experiment and should test a wider range of materials. All future extrusion experiments discussed in this document use stainless steel syringe needles without the use of PTFE tubing.

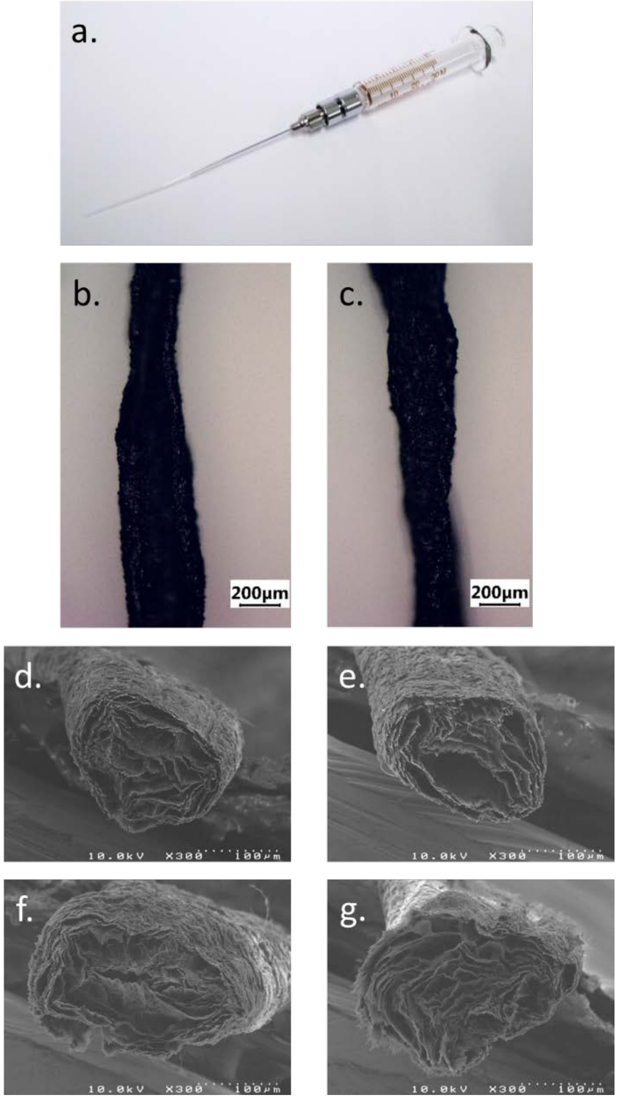

Figure 28. a. Photograph of a glass syringe with a 22 Ga stainless steel syringe needle inserted into 8 cm of PTFE tubing. b and c. Optical microscopy images of two replicate samples extruded using the syringe in panel a. d-g. Cross-sectional SEM images of laser-cut wire segments extruded using the syringe in panel a.

Inducing tension on the wire during coagulation was found to have a substantial effect on the uniformity and conductivity of extruded SWCNT wires in Section 3.4.1. To further increase the elongation of the dispersion during coagulation, an experiment was designed where an air-gap was introduced between the syringe needle and the coagulant bath, as opposed to the standard experimental setup, which places the tip of the syringe needle just below (1-3 mm) the surface of the coagulant (as seen in the “Standard” case in Figure 29a). The hypothesis was that this air gap would allow for the dispersion to thin and elongate and induce alignment in the SWCNTs as it fell from the syringe needle opening, possibly also reducing wire diameter and increasing density as seen in the “Goal” scenario of Figure 29a. To test the hypothesis, a 50 mg/ml dispersion of purified SWCNTs in CSA was extruded through a 22 Ga syringe needle into a 20 cm deep column of room-temperature acetone, either with the syringe needle submerged 1-3 mm into the coagulant bath (“submerged”) or held 1-2 mm above it (“air gap”). Initially these experiments were conducted in an open laboratory hood, but concerns of dispersion coagulation due to interaction with humidity in the room caused the results presented here to be conducted in a dehumidified dry room at 0.1 % residual humidity. In both cases, fumes were observed to be emitted from the SWCNT-CSA dispersion when there was an air gap, and the dispersion flowed through this gap non-uniformly. While a continuous stream of dispersion was noted, there was also a “dripping” effect where droplets formed regularly at the tip of the syringe needle which fell down the continuous dispersion stream as depicted in the “Observed” schematic in Figure 29a. As a result, wires formed with the submerged syringe needle were highly uniform while those extruded through the dehumidified air gap had highly-nonuniform morphology with alternating regions of small and large diameter as seen in the optical microscopy images in Figure 29b. The electrical characteristics of wires extruded through the dehumidified air gap suffered as an effect of this nonuniformity. Greater linear densities were observed with lower specific conductivities and greater variation in these metrics in wires extruded through the dehumidified air gap than in wire extruded with the submerged syringe tip. Lower specific conductivities observed in this study for both sets of wires than in previous best-practices studies are likely a result of the use of room-temperature acetone baths (as opposed to chilled) and shallower coagulant baths (20 cm as opposed to 30 cm deep). In conclusion, it was determined that the CSA dispersion is best kept within the syringe and syringe needle until it is introduced into the coagulant bath. Future work may have success using an air gap if faster extrusion rates are employed.

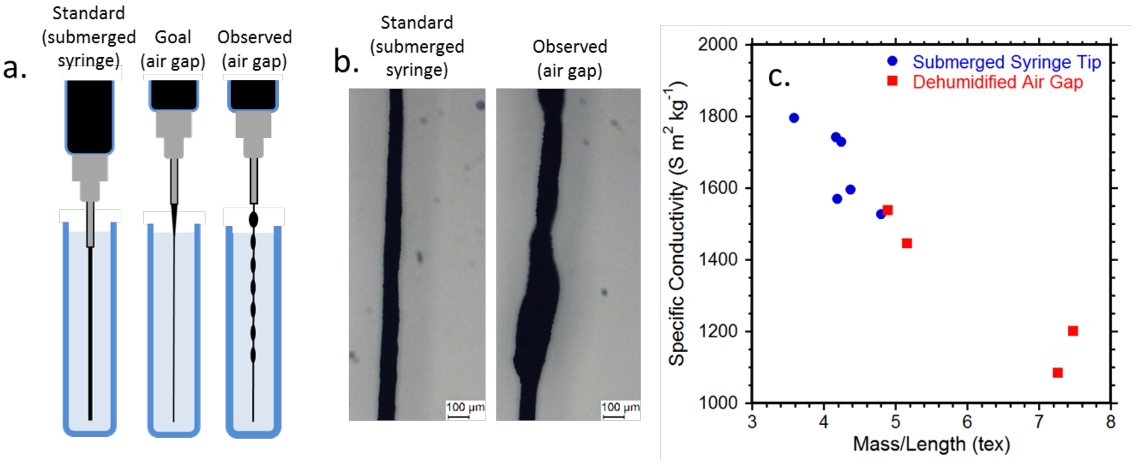

Figure 29. a. Schematics of the standard extrusion setup which involves a syringe needle with the tip submerged into the coagulant bath, the desired goal scenario of an air-gap extrusion in which the syringe needle is elevated above the surface of the coagulant bath and the stream of extruded dispersion uniformly thins before entering the coagulant bath, and the observed air-gap scenario in which droplets form in the air gap and prevent the resulting wire from having a high degree of uniformity. b. optical microscopy images of a wire extruded with a submerged syringe needle (left) and of a wire extruded with a dehumidified air-gap (right). c. Specific conductivities of wires extruded using the standard setup (blue circle data points) and with a dehumidified air-gap (red square data points) as a function of their linear mass density.

An additional method for inducing elongation in the coagulating SWCNT-CSA dispersion during wire extrusion is through coaxial coagulant flow. Flowing coagulant in the direction of dispersion causes elongation and thinning of the coagulating SWCNT-CSA dispersion which may induce greater alignment than extruding wires into a stagnant coagulant bath [44]. To test the performance of extruded SWCNT wires fabricated with coaxial coagulant flow, coaxial syringe needles (Figure 30a) were purchased from ramé-hartwith a variety of inner and outer syringe needle diameters. An initial study used a 52 mg/mL purified SWCNT in CSA dispersion into a stagnant ~0 °C acetone coagulant bath 20 cm deep extruded at a rate of 0.1 mL/min (6 mL/hr). A coaxial syringe needle was selected with a 22 Ga inner syringe and an 18 Ga outer syringe (18/22) and ~10 °C acetone was flowed through the outer syringe at varying rates. A vertical extrusion set up was used so that gravity was allowed to tension the wire as it entered the stagnant coagulant bath. The tip coaxial syringe needle was held 1-3 mm beneath the surface of the stagnant coagulant bath for all trials after attempts to introduce a 1-2 mm gap between the coaxial syringe needle and the stagnant coagulant bath resulted in segmented wire formation. Electrical results from wires extruded using this setup and four different coaxial acetone flow rates (0, 1000, 2000, and 3000 mL/hr) are presented in Figure 30b. These results demonstrate that at 0 mL/hr coaxial acetone flow rate, lower specific conductivities are attained using this setup than with a standard single-outlet syringe needle. This may be due in part to the syringe needle outlet preventing complete submersion of the SWCNT dispersion outlet into the coagulant bath or from the decreased bath depth. Increasing coaxial coagulant flow rates produced wires with higher specific conductivities, with a maximum value for this study being 2400 S m^2 k^{-1}, higher than using previous best practices. Despite the high specific conductivities observed in this study, conductivity values in Figure 30b are all below 1 MS/m. The reason for the lack of high conductivities in this study is apparent when considering the morphology of the wire cross sections, as exemplified in the laser-cut cross-section SEM image in Figure 30c. While the coaxial flow has enhanced specific conductivity through enhanced alignment on the surface of SWCNT extruded wires, the flow has caused substantial void space in the interior of the wire, reducing the cross-section dependent conductivity. Further work with coaxial syringes is needed to optimize the proper ratio of sizes and geometry of inner and outer syringe and the relative flow rates of dispersion and coagulant in order to reduce void space inside wires extruded with coaxial flow.

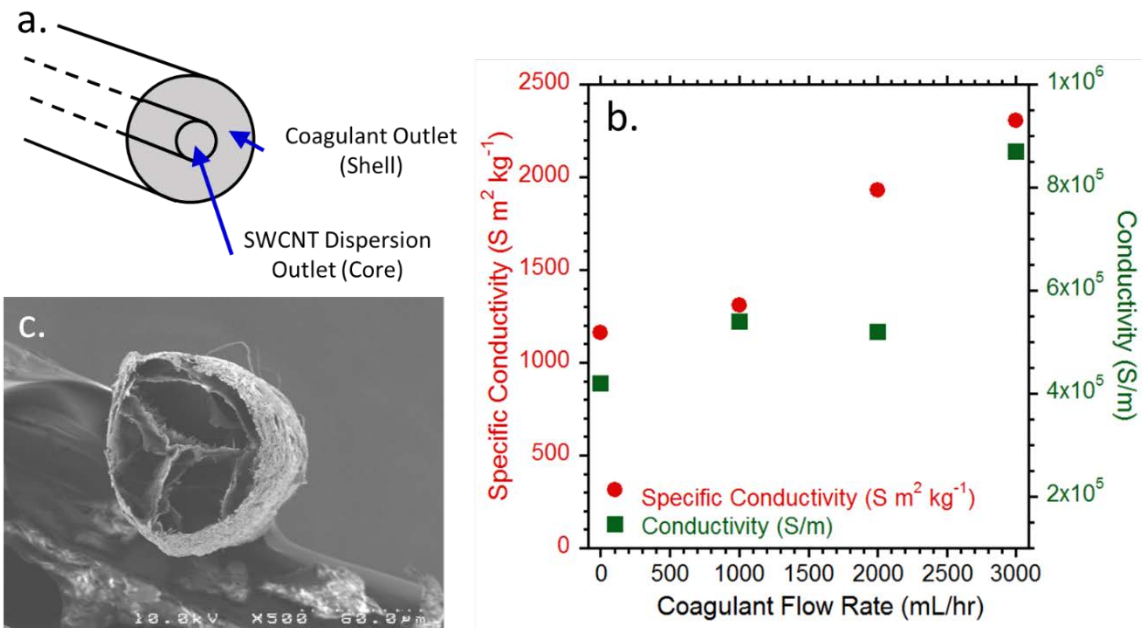

Figure 30. a. Schematic of the opening of a coaxial syringe needle. b. Specific conductivity (left axis and red circle data points) and conductivity (right axis and

green square data points) of wires extruded using a 18/22 Ga coaxial syringe needle with various rates of coagulant flow through the outer (18 Ga) syringe opening.

An additional study using coaxial syringe needles to deliver coagulant flow during wire extrusion was conducted to assess the impacts of coaxial syringe needle size. For this study, one coaxial syringe needle with a 14 Ga outer syringe needle and a 18 Ga inner syringe needle (14/18) was compared to a coaxial syringe needle with an 18 Ga outer syringe needle and an 22 Ga inner syringe needle (18/22 - the same size as used in the previous study). Wires were extruded from a 50 mg/mL dispersion of purified SWCNTs in CSA at a rate of 0.1 mL/min (6 mL/hr) into a 5 °C stagnant bath of acetone 28 cm deep. The coaxial flow rate was chosen to be 3000 ml/hr due to the high specific conductivities attained with this flow rate in the previous study. Optical images of both sets of extruded wires can be seen in Figure 31a and b. Despite the larger size of the 14/18 Ga syringe needle, the wires produced from this coaxial syringe needle were of smaller diameter and mass per length (1.2 tex) than those produced from the smaller 18/22 Ga coaxial syringe needle (3.4 tex). However, both sets of wires had similar specific conductivities; the average specific conductivity of the wires extruded from the 14/18 Ga syringe needle was 1500 S m^2 kg^{-1}, and the average specific conductivity of wires extruded from the 18/22 Ga syringe needle was 1700 S m^2 kg^{-1}. Representative cross-sectional SEMs of laser-cut wire segments can be seen in Figure 31c and d. The smaller cross section of the wires extruded from the larger 14/18 Ga syringe needle lead to a higher conductivity of 1.3 MS/m than the wires extruded from the smaller 18/22 Ga coaxial syringe needle, which had a conductivity of 0.8 MS/m. Future studies using coaxial syringe needles for wire extrusion should take into account the relative rates of flow between the dispersion and the coagulant bath, as well as the flow rate of the individual flows.

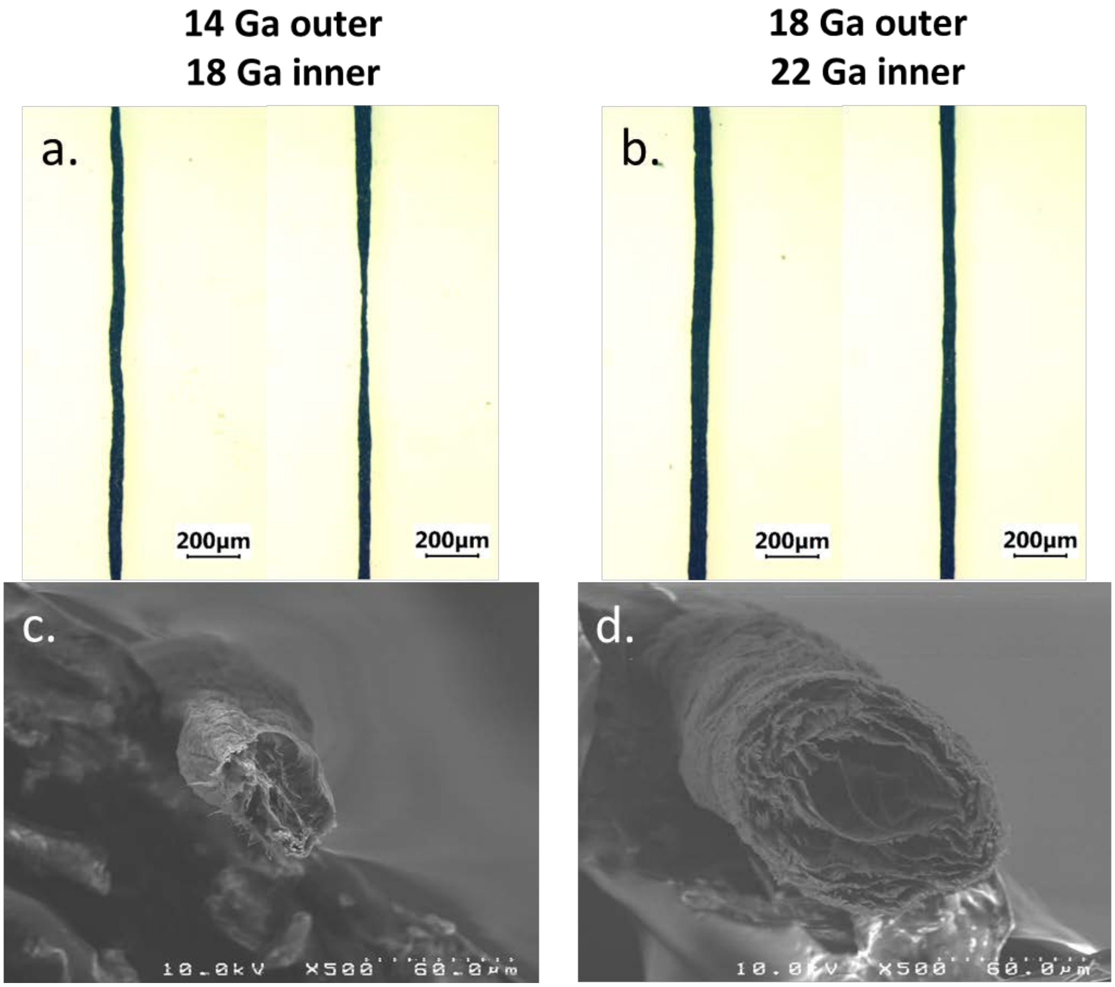

Figure 31. Characterization of wires extruded using coaxial syringes. a. Optical microscopy images of two replicate wire segments extruded from the 14/18 Ga coaxial syringe needle. b. Optical microscopy images of two replicate wire segments extruded from the 18/22 Ga coaxial syringe needle. c. Cross-sectional SEM of a wire extruded through the 14/18 Ga coaxial syringe needle. d. Cross-sectional SEM of a wire extruded through the 18/22 Ga coaxial syringe needle.

Influencing the rate of coagulation of SWCNT-CSA dispersion during extrusion is of interest because an ideal coagulation rate allows for the solidifying dispersion to stretch and reorient its constituent SWCNTs into alignment in the wires axial direction but does not coagulate so slowly that the wire breaks under its own weight. One method of controlling coagulation rate is by controlling the thermal energy available in the coagulant bath. The coagulant bath temperature can be controlled by immersing the coagulant vessel in a temperature-controlled bath such as a water and ice bath, acetone and dry ice bath, or a heated water bath on a hotplate. Using these temperature control techniques, extrusions were conducted using a 48 mg/mL purified SWCNT in CSA dispersion extruded through a 22 Ga syringe needle at 0.1 mL/min into a 22 cm deep acetone coagulant bath. The acetone bath temperature was held at -10 °C through the use of a dry ice and acetone bath (dry ice was introduced into the cooling bath, not the coagulant bath), 0 °C though the use of an ice and water bath, 10 °C by refrigerating the coagulant bath prior to extrusion, 20 °C by leaving the coagulant bath at room temperature, and 35 °C and 45 °C through the use of a hot plate. The average specific conductivities of wires extruded into baths held at each of these temperatures are presented in Figure 32. A clear trend is noted where decreased coagulant bath temperature produces higher specific conductivity extruded wires. This increase is expected to be due to slower rates of coagulation in colder baths, allowing greater time for the wire to stretch under its own weight in the vertical extrusion setup than in warmer baths, creating a greater degree of alignment and uniformity. The use of a dry ice and acetone bath to chill the coagulant bath can offer temperatures as low as -78 °C. The main challenge in using < -10 °C coagulant baths are maintaining the uniformity of the bath temperature so that the top of the bath is not significantly warmer than the bottom, and preventing boiling of the chilled acetone which disrupts uniform wire coagulation.

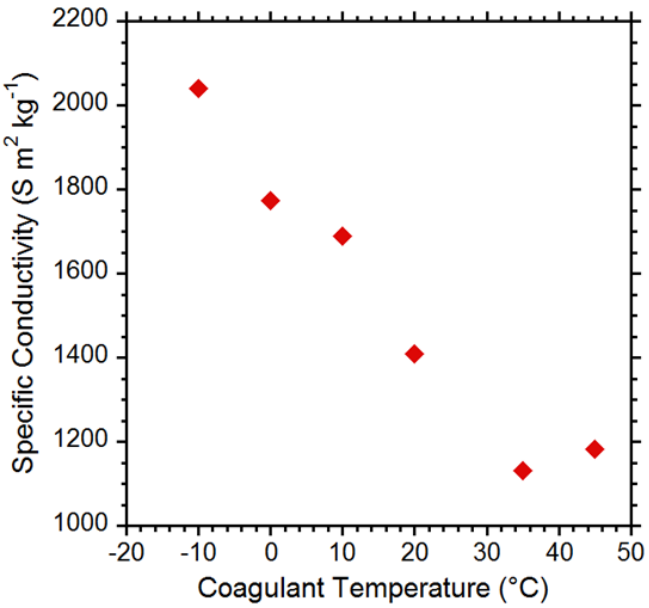

Figure 32. Specific conductivities of extruded SWCNT wires extruded into acetone baths of various temperatures.

4.4 Extrusion of SWCNT Wires using Best-Practices

Using acetone baths chilled to -10 °C, wires were extruded using the best practices determined throughout the present work. A 66 cm deep coagulant vessel was used (a burette), which could not be fully immersed in a dry ice and acetone bath. Instead, the acetone coagulant was chilled in a beaker partially submerged in a dry ice and acetone bath and then poured into the burette. Challenges in using this system were in keeping the coagulant bath cold and in preventing the sinking extruded wire from contacting the sides of the vessel. A high weight loading of 61 mg/mL purified SWCNT in CSA was used for the dispersion, which was extruded though a 22 Ga syringe needle at 0.1 mL/min. The resulting wires were stretched and dried under tension prior to characterization and achieved specific conductivities as high as 2200 S m^2 k^{-1}. A representative optical microscopy image is included in Figure 33a, which demonstrates the highly uniform nature of the resulting wires. High-magnification SEM images in Figure 33b and c show the high degree of alignment present. The cross-sectional images of laser-cut wires sections in Figure 33d-g show these wires have the typical layered morphology of extruded SWCNT wires. These cross-sectional images combined with width and thickness measurements from the side-on SEM image of a twisted wire (Figure 33h) were used to calculate a conductivity of 5.1 MS/m, indicating that this wire has the conductivity of the most conductive wire regions from the best practices extruded wires from Section 3.4.2.

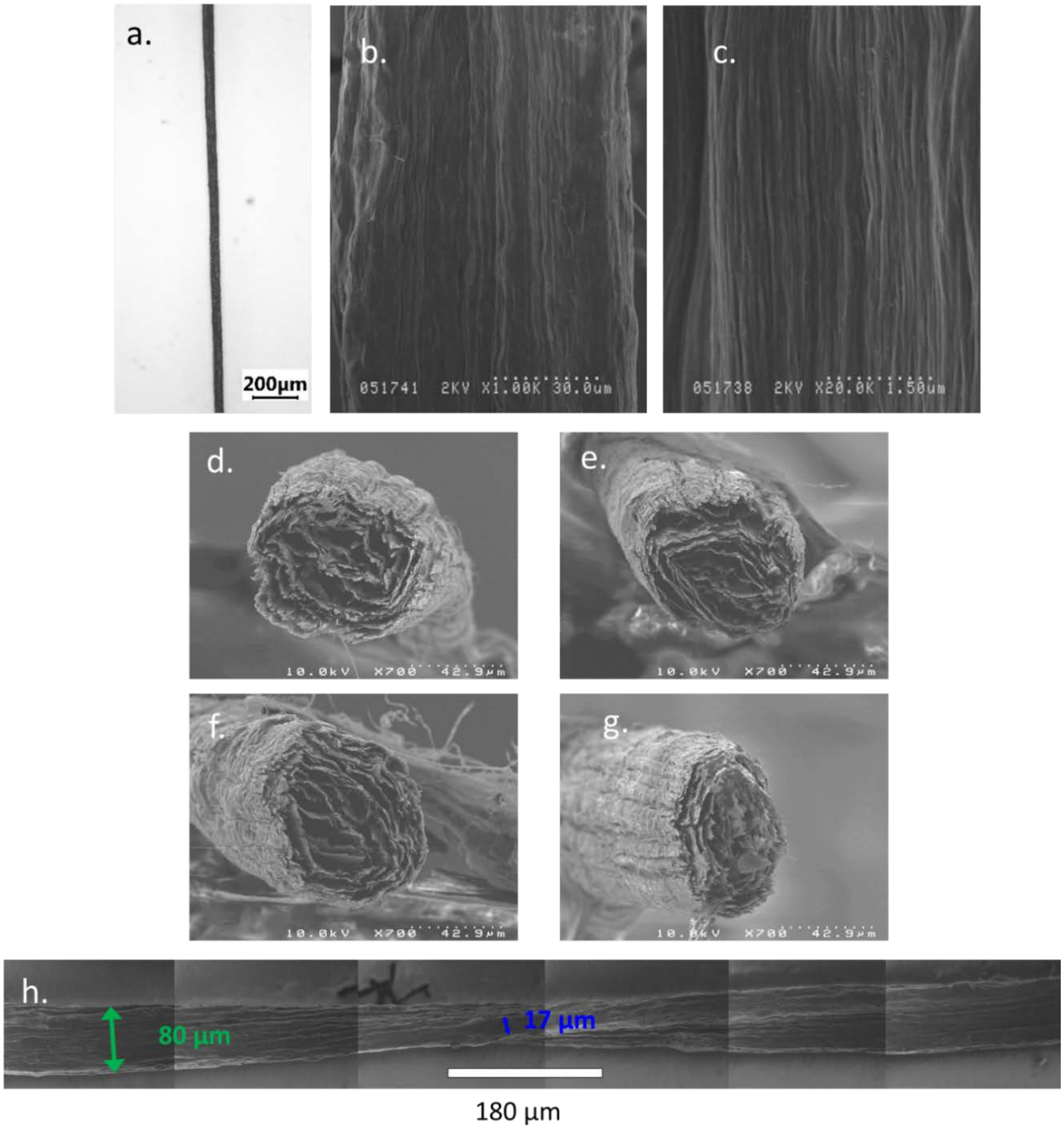

Figure 33. Characterization of wires extruded into a -10 °C, 66 cm deep acetone bath from a 61 mg/mL weight loading dispersion. a. Optical microscopy image. b and c. Side-on SEM images of the wire, with the wire axis oriented vertically. d-g. Cross-sectional SEM images of wire segments cut with a laser cutter. h. Side-on SEM image of a wire mounted with a slight twist. Width and thickness measurements are superimposed.

Due to the presence of void space in the wires from Figure 33 and other extruded CNT wires, experiments with wire calendering were conducted. Calendering involves pressing a sample between two rollers which are spun in opposite directions to facilitate the sample pressing without causing shear forces on the sample surface. This treatment is of interest for removing the void spaces inside extruded wires and providing an estimate of the conductivity attainable through current extrusion methods if less void space was created during extrusion. Though calendering causes densification in one plane, the lack of frictional shear force on the sample and the small diameter of extruded wires makes calendering a preferable process for densifying extruded wires compared to radial densification (see Section 7.3), which requires wires to be pulled though a stationary die with a fixed diameter opening, even though radial densification preserves the cylindrical nature of a wire. Wires were extruded from a 50 mg/ml dispersion of purified SWCNTs in CSA through a 22 ga syringe tip into an 30 cm deep, 5°C acetone coagulant bath at 0.1 mL/min and the conductivity was calculated to be 5.4 MS/m using laser-cut corss-sectional SEM imaging. These wires were then subjected to calendering with the gap between the rollers kept at a minimum, less than 5 µm. Wires had a tendency to stick to the steel rollers. The resulting wires were significantly flattened, increasing the ribbon-like nature of the wires, as seen in the two replicate laser-cut segments in Figure 34a and b. In these segments, laser cutting took place after the wire segments had been calendered. The flaring observed at the laser-cut ends of the wire segments in Figure 34a and b is likely a result of the laser cutting as thicker regions are not observed elsewhere in the calendered wire. These flared regions make determining the cross-sectional area from SEM imaging difficult, but upper bounds can be established and profilometry was used to confirm an approximate thickness of 11 μm. The wire was assumed to be rectangular in cross-section and a conductivity of 2.4 MS/m was calculated. The fact that calendering did not reduce the measured wire cross-sectional area indicates that cross-sectional area was overestimated in the laser-cut sections measured prior to calendering. Future work should involve calendering SWCNT wires after they are laser-cut for imaging instead of before to mitigate the effects of flaring during laser cutting, and should investigate methods for laser-cutting and cross-sectional imaging with more accuracy, even when calendering is not employed.

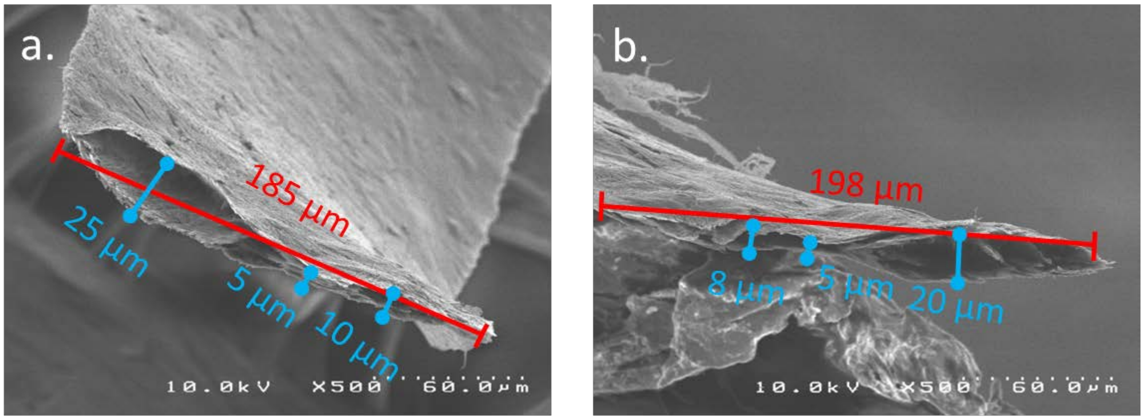

Figure 34. a. and b. SEM images of two replicate segments of extruded SWCNT wires that were calendered and then laser-cut.

4.5 Extrusion Automation and Apparatus Construction

After determining the major factors in fabricating high conductivity CNT wires, it is desirable to construct an automated system for wire production that can be optimized and easily adapted to accommodate the optimization of additional extrusion factors not yet explored. An extrusion apparatus has been built to accomplish this objective and can be seen in Figure 35a. The scaffold of the apparatus is build from slotted aluminum rail which should resist corrosion from acidic vapors from the CSA dispersion and acetone or other organic solvent vapors from an open coagulant bath. A syringe pump is mounted at a variable angle, allowing for either vertical or angled extrusion. The angle selected for use in Figure 35 allows for a horizontal extrusion. The coagulant bath can be seen in Figure 35b, with the syringe needle submerged on the left, and two custom 2 in diameter PTFE spools. The mechanized spools allow for wire tensioning during extrusion in the horizontal configuration. Extruded wire can be fed from one spool to the next so that he first spool applies tension on the wire as it coagulates and the second spool applies tension post-coagulation. The user can set the speed of the first spool and the percent difference in speed from the first spool to the second, which is equivalent to the percent elongation applied to the wire, through the use of two potentiometers and quantitative data on these two metrics is displayed on two numeric readouts on the control panel shown in Figure 35c. The spools are computer controlled by an Arduino Uno R3 which can be seen along with its wiring in Figure 35d. Instructions for use of this apparatus can be found in Appendix B.

A test run of the extrusion apparatus was conducted using a 50.1 mg/mL dispersion of purified SWCNTs in CSA. A 22 Ga syringe needle was fitted onto the extrusion apparatus and an extrusion rate of 0.1 mL/min was used. The coagulant bath was acetone at room temperature and the second spool was not used to tension the wires post-coagulation. 11 wire segments were characterized and found an average resistance per length of 101 Ω/m with a standard deviation of only 6% (compared to 10-15% standard deviation for extrusions conducted by hand), and an average linear mass density of 7.2 tex with a standard deviation of 17%. From these measurements, an average specific conductivity of 1400 S m^2 k^{-1} was calculated, with a standard deviation of 10%. Optical microscopy images of these highly-uniform wires can be seen in Figure 35e and f. Cross-sectional SEM images of laser-cut wire segments can be seen in Figure 35g-j, and were used to calculate a conductivity of 1 MS/m. These wires demonstrate that the extrusion apparatus is capable of producing highly uniform extruded SWCNT wires. Future modifications to the extrusion apparatus to enhance extruded SWCNT wire conductivity include chilling the coagulant bath and including temperature control measures (such as an integrated ice bath), using more precise motor controllers to allow for wire tensioning post-coagulation, and integrating a spooling guide to facilitate easier wire removal from the spools.

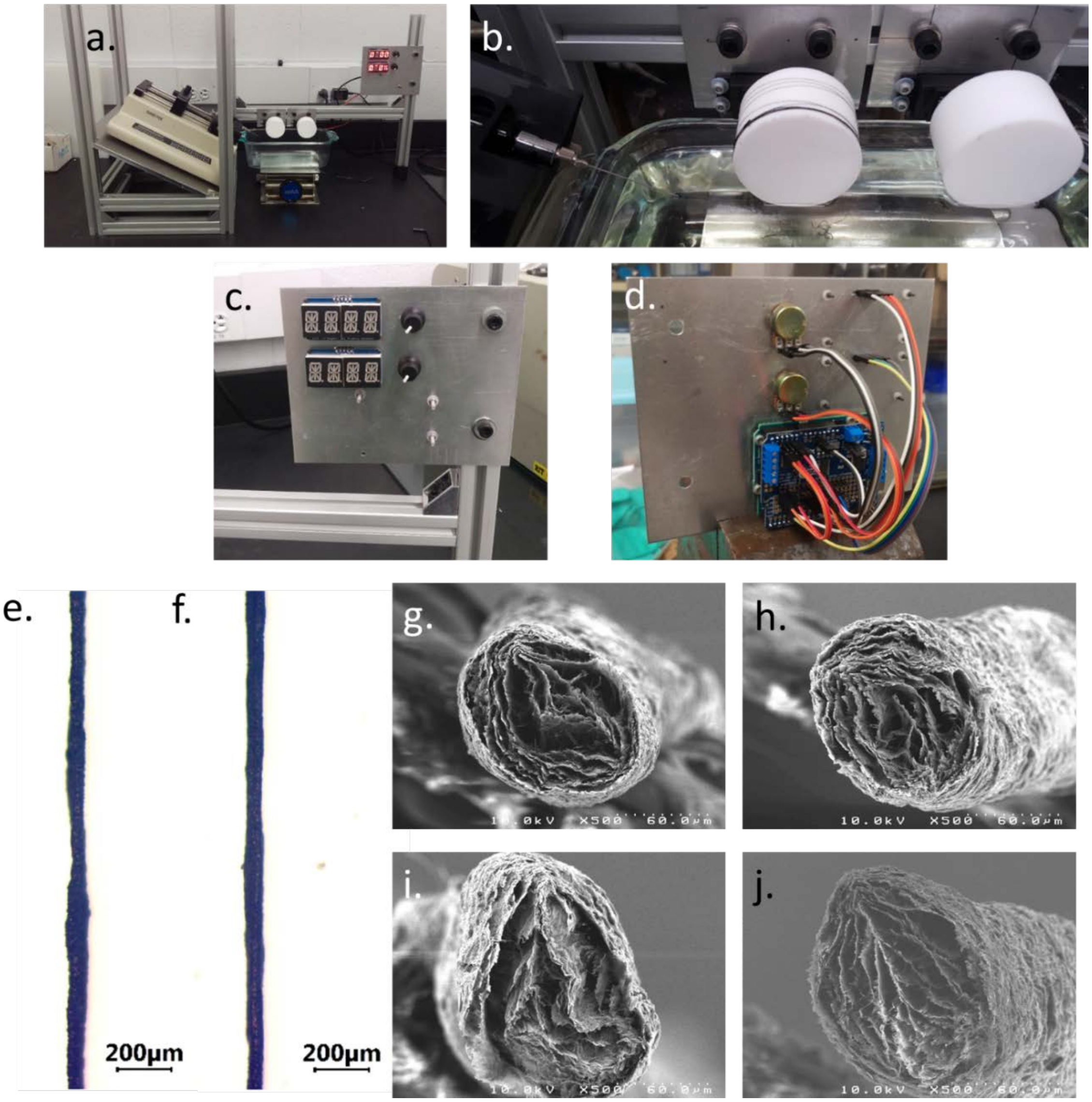

Figure 35. The extrusion apparatus and characterization of wires produced using it. a. Photograph of the extrusion apparatus. b. Close-up photograph of the coagulant bath in the extrusion apparatus, in which the submerged syringe and extruded wire can be seen on the left, and the two PTFE spools can be seen on the right. The first (leftmost) PTFE spool has extruded wire winding around it. c. Photograph of the extrusion apparatus control panel, which at this time consists of two potentiometers and two numeric display panels. d. The Arduino Uno R3 and wiring which connects and controls the components of the control panel and the spooling motors. e and f.

Optical microscopy images of two replicate wire segments extruded from the extrusion apparatus. g-j. Four replicate cross-sectional SEMs of laser-cut wire segments produced using the extrusion apparatus.

4.6 Extruded Wire Fabrication Conclusions

Several types of CNTs are employed for CSA dispersion and extrusion in the chapter, and many extrusion processing techniques are analyzed. In terms of specific conductivity, extruded wires made from laser-vaporized SWCNTs out-perform extruded wires made from HiPCO SWCNTs by 3.7x, Nanocomp MWCNT/SWCNT hybrids by 1.5x, and SSNano DWCNTs by 1.9x. Extrusions of SWCNTs synthesized using 1000 °C nitrogen carrier gas performed similarly to extruded wires made from SWCNTs synthesized using the standard 1125 °C argon carrier gas, attesting to the robust high-conductivity of laser-vaporization SWCNTs synthesized under different conditions.

Of the extrusion process variables study that influence dispersion introduction into the coagulant bath several were found to have strong effects on wire performance while others were insignificant at the values studied. High specific conductivity extruded wires were produced regardless of the length of the syringe needle and the extrusion rate used. Air gaps reduced wire uniformity and it was found that keeping the syringe needle submerged 1-3 mm below the coagulant bath surface was best for controlling wire coagulation. Changing the material of the spinneret had a significant impact on the wires extruded through it, but PTFE was not found to produce better wire than the standard stainless steel used in other studies. This effect may be a product of the non-uniform pathway the dispersion flows through as an effect of the test set up used, and not the surface forces influencing dispersion flow and alignment.

Larger diameter syringe needles promoted higher extruded wire specific conductivity, as did colder acetone coagulant baths and increased rates of coagulant flow through coaxial syringe needles. Wires extruded from a 61 mg/mL SWCNT in CSA dispersion through a 22 Ga syringe needle into a -10 °C, 66 cm deep acetone coagulant bath had uniformly high conductivities of 5.1 MS/m. A constructed extrusion apparatus was able to extrude extremely uniform SWCNT wires with 1.1 MS/m conductivity and only 6% variation.

Chapter 5. High-Current Behavior of Carbon Nanotube Yarns and Wires

5.1 Introduction to High Current Conditions

Carbon nanotube electrical wiring is of interest in power and electrical transmission applications. In certain applications such as high-power transmission lines and motor windings, the ability for wires to withstand high electrical currents is of interest. To determine the relevance of CNT wires for these applications, it is desirable to design high-current testing methodology, measure the behavior of CNT wires in high-current conditions, and to analyze the mechanisms by which CNT wires fail if exposed to very high currents. The goal of studying high-current behavior is to determine the environments and conditions that impact CNT wire high-current behavior and their high-current failure mechanisms in order to design high-ampacity CNT wires and methods of treating CNT wires, such as developing coating processes, to enhance their ampacities.

When working at high currents, traditional wiring is rated by several metrics. The **ampacity** of a conductor (in Amperes, A) is the maximum current that the conductor can continuously withstand before reaching a specified temperature. The temperatures that ampacities are given at are often insulation dependent or dependent on the maximum allowable temperatures of system components that will be located in proximity to the conductor, and the ampacity at 100 °C is frequently used [76]. The *failure current*, or fusing current, is the current expressed in Amperes at which a conductor becomes an open circuit, while the *maximum current* (also known as fusing current, expressed in Amperes) is the greatest current that a conductor can withstand [77], [78]. The maximum and failure currents may be the same for a given material, but occasionally differ as will be discussed in the case of carbon nanotubes in the following sections. Maximum and failure currents are often given as *current densities* in A/m^2, which are normalized to the cross-sectional area of the conductor.

Electromigration limits the current density of nanoscale metallic wiring and interconnects to 10 nA/nm^2, while CNTs are less sensitive to electromigration and can achieve current densities of 10 µA/nm^2, three orders of magnitude greater than metals [11], [74]. Previous experimental work determining the high current failure of individual multi-wall CNTs, CNT sheets, and double-wall CNT fibers has been conducted in the literature. In 2000, individual multi-wall carbon nanotubes (MWCNTs) were deposited onto electrical contacts and a constant voltage was driven across segments of each MWCNT [79]. Stepwise failures were observed over time, and the authors attribute these failures to individual carbon shells failing. High-current failures in air and in vacuum are compared, and higher powers were reached before breakdown in vacuum, with vacuum failures occurring 1000x more rapidly than in air. [79]

The high-current behavior and breakdown in CNT sheets and thin film transistors has also been studied [80], [81]. Studies on CNT sheets found that randomly aligned (HiPCO) SWCNT sheets failed with a current density of 6.7 MA/m^2 while those with alignment induced through high magnetic fields during filtration failed at 11 MA/m^2, indicating that sample morphology plays a strong role in the maximum current density of a CNT conductor [80]. The high-current failure of dry-spun fibers of DWCNTs with diameters of 5-20 µm has also been studied and found that the smallest diameter samples had the highest maximum current densities of 1 GA/m^2 while other samples typically measured ~490 MA/m^2 in air [82]. Current-controlled testing of the high-current failure of extruded DWCNT wires determined the maximum current density of these wires in vacuum (136 MA/m^2), argon (303 MA/m^2), nitrogen (455 MA/m^2), and air (211 MA/m^2) [83]. Larger diameter (> 1 cm) radially densified wires have demonstrated the ability to sustain > 20 A for 40 days [84]. This study correlated the maximum wire temperature during high-current testing to be equivalent to the onset of material oxidation through TGA analysis.

5.2 Current Carrying Capacity Test Conditions

In order to assess the high-current behavior or CNT wires and be able to objectively compare the performance between commercially sources CNT yarns and extruded SWCNT wires under varying ambient conditions, a test fixture was designed and built and the relevant factors in the testing procedure were evaluated.

The test fixture consisted of a chamber formed by a glass cylinder 35 cm in length and 8.5 cm in diameter with steel endcaps. One endcap included 6 mm diameter gas inlet while the other had a 6 mm diameter gas outlet. An insulated rod was fixed to one endcap so that it projected into the center of the chamber, and two copper electrical clip-type contacts were mounted to this rod using hose clamps so that the number and distance between electrical contacts could be easily adjusted. The electrical probes can be seen inside the test chamber in Figure 36. Gas flow rate to the gas inlet was regulated and measured by a Key Instruments flow meter with a range of 0.2 to 2.5 SCFH. For electrical testing, the chamber was purged for 20 min with the selected gas (either dry air, nitrogen (99.998% purity), or helium (99.999% purity), all from Airgas) for 20 min at a flow rate of 2.2 SCFH. A two point electrical test was used for the data presented here. The electrical contacts were 2 mm in width and were separated by 48 mm unless otherwise noted. The electrical contacts were connected to a Keysight N8924A high-voltage direct-current power supply.

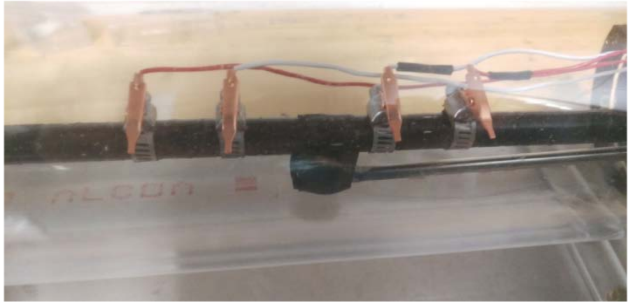

Figure 36. Photograph of 4 electrical probes mounted inside the glass cylinder test chamber.

Initial experiments on the influence of test conditions were conducted using Miralon yarn material supplied by Nanocomp Technologies, Inc., which will be referred to as “CNT yarn”. This material is made using a dry spinning technique. Two separate lots (lot #’s 60025 and 60027) of the yarn were tested with 0.5 SCFH of nitrogen flowing through the test fixture after the initial 20 minute nitrogen purge at 2.2 SCFH. All yarn segments were 7 cm long and each was loaded in the chamber individually and the applied voltage was increased by 150 mV every 30 seconds until an open circuit was obtained, and the chamber was allowed to cool for at least 10 min before loading the next sample and purging for 20 min. The current and voltage data acquired by the Keysight N8924A is plotted in Figure 37a. In the 10-15 volt range, both lots of yarn have similar behavior, but after an initial peak in measured current, the behavior between the two lots begins to differ. Samples of CNT yarn lot 60025 reach a secondary, increased maximum current while samples of CNT yarn lot 60027 begin degrading. Yarns from lot 60025 failed at ~50 V (this is the voltage where the wire becomes an open circuit) and reached maximum currents of 590 – 660 mA, while CNT yarn samples from lot 60027 failed at ~44 V and had a maximum currents of 620-640 mA. For future studies using CNT yarns, lot 60027 was selected due to this closer grouping of maximum currents.

Next, the effect of ambient gas flow rate on maximum current and the voltage required to reach maximum current was determined. Flowing gas introduces convective cooling on the wire being tested, whereas a wire without flowing gas is only subject to radiative and conductive thermal losses. Induced cooling theoretically increases the electrical current required for joule heating to reach the thermal decomposition temperature of the material in the wire. For this test, nine CNT yarn samples were subjected to 150 mV increases every 5 seconds with one of three rates of air flow. For the 0 SCFH scenario, the chamber was not purged, but closed with room air filling it. Results of this study can be seen in Figure 37b. From this plot, it can be determined that with either 0.5 SCFH or 1.0 SCFH of flowing air, both the maximum current and the voltage at which maximum current was reached are slightly increased over their values without air flow. These differences may be due to convective cooling from the airflow, or due to the differences in humidity of the room air vs the dry tank air, or likely a combination of both factors. In order for similar rates of convention between various ambient gasses, a flow rate of 0.5 SCFH was selected for future studies to maintain positive pressure in the test chamber to prevent room air from entering the chamber during a test and to minimize convective cooling to model practical application scenarios where ambient flow is not controlled.

Lastly, the dependence of failure voltage and maximum current on the rate of voltage increase during testing was evaluated. It was expected that faster voltage ramp rates would increase the maximum current due to insufficient time for heat generation from joule heating to affect wire performance. 100 mV increases were used with three equilibration times before the next increase: 15, 30, and 60 seconds. These tests were conducted in the test fixture while under 0.5 SCFH of flowing nitrogen. The measured current as a function of applied voltage from these tests can be seen in Figure 37c. The 100 mV increase every 30 seconds ramp rate (red curve) had the highest failure voltage and maximum current of 22 V and 525 mA, respectively. This was 37 % and 33 % higher than the lowest failure voltage (16 V) and maximum current (395 mA), respectively, both measured on the sample tested with a 100 mV every 60 seconds ramp rate. The lack of a strictly increasing or decreasing trend in this data may indicate that either these ramp rates are insufficiently different to cause significant differences in the data, or that the relationship between ramp rate and failure voltage and maximum current is more complex than previously theorized. While slower ramp rates allow for heat buildup, they also allow for heat dissipation from low-conductivity areas in wires, possibly presenting competing effects. Further study of this effect with additional ramp rates and multiple replicates at each rate could elucidate the reasons for the observed lack of trend in this data.

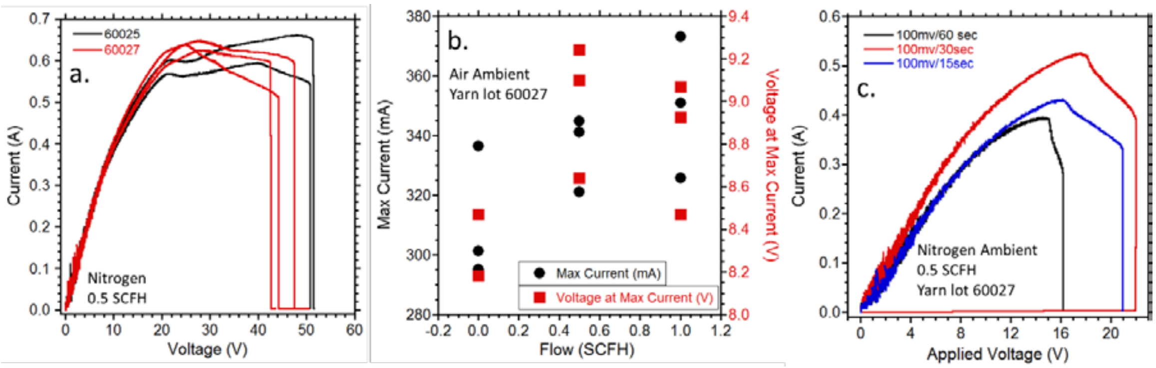

Figure 37. a. Comparision of the current-voltage characteristics of two different lots of yarn with 3 replicates from lot 60027 and two replicates from lot 60025, all tested under nitrogen flowing at 0.5 SCFH with voltage increases of 150 mV every 5 sec. b. Plot of max current (left axis, black circle datapoints) and the voltage at which maximum current was reached (right axis, red square datapoints) of nine samples of CNT yarn lot 60027 for three different flow rates of air in the test fixtrure. c. Measured current as a function of applied voltage for three segments of CNT yarn lot 60027 under 0.5 SCFH of nitrogen with the applied voltage increasing by 100 mV every 60, 30, or 15 seconds.

A major factor in testing the high current failure points of a wire is in the type of test used, which can be either a current-controlled test or a voltage-controlled test. To experimentally compare the two, six segments of CNT yarn were subjected to either a current-controlled or voltage-controlled test under 0.5 SCFH of flowing nitrogen. The ramp rates were chosen so that similar currents and voltages would be expected during the initially linear (ohmic) region of wire testing in both current- and voltage-controlled scenarios at equal times into the test. Using a resistance of 22 Ω, the current-controlled tests were performed using 5 mA increases every 30 seconds and the voltage-controlled tests were performed using 110 mV increases every 30 seconds. The measured currents from these tests as a function of applied voltage are plotted in Figure 38a. While all curves overlay for voltages below ~8 V, drastic differences can be seen in the curve shape and maximum currents attained between the data from current-controlled tests (blue curves) and voltage-controlled tests (red curves). To investigate the source of these differences, the measured current from all 6 tests is plotted as a function of the test time in Figure 38b, and the applied voltage is plotted as a function of the test time in Figure 38c. In Figure 38b, it is seen that in the current-controlled test the current increases linearly with time as expected since this is the programmed behavior of the power supply, while the measured current from the voltage-controlled tests is initially linear until approximately 35 min (300 mA) where it deviates from linearity and the rate of current increase begins to decrease. The opposite behavior is observed in Figure 38c, where the voltage over time from the voltage-controlled tests is always linear as programmed, but the rate of voltage increase in voltage applied to the current-controlled tests begins to increase after 35 min (6 V). This behavior indicates that the CNT yarns begin to change their resistances after applying 6 V or 300 mA. In the voltage-controlled tests, the resistance change means that measured current begins to increase at a lower rates and eventually becomes a current decrease. Conversely, in the current-controlled test, the increase in resistance means that the applied voltage must be applied with increasing rapidity to maintain current increases at the programmed rate.

This behavior is analogous stress-strain testing in mechanical engineering. For comparison, CNT yarns were placed in a TA Q800 Dynamic Mechanical Analyzer which induces axial strain on the CNT yarns and measures the resulting tensile force. Like the power supply, it was operated in both strain-controlled and force-controlled manners until the yarn was completely bisected. The results of applying 0.2 % strain per minute in the strain controlled scenario (red curve) and of applying 0.233 N per minute in the force controlled scenario (blue curve) are plotted with tensile force as a function of applied strain in Figure 38d. Unlike in the electrical case, both of these curves are highly similar, but a key difference is evident at ~15 % strain: the data from the strain-controlled test has a turnover point where force begins to decrease with increasing strain, similar to how current begins to decrease with increasing voltage in the voltage-controlled test. In mechanical analysis, the point at ~2 % strain and 1.8 N, when the curves are no longer linear, is known as the yield point, after this point material deformation is known as plastic deformation [85]. The data is again broken out into tensile force as a function of time and strain as a function of time in Figure 38e and f, respectively. In Figure 38e, the force in the force-controlled (blue curve) test increases linearly with time, as it is programmed to do, while the force in the strain-controlled (red curve) test deviates from linearity when it reaches 1.8 N, the yield point, after which the rate of force increase decreases. In Figure 38f, the increase in strain in the strain-controlled scenario is always linear, as it is programmed to be, while the strain in the force-controlled scenario increases at an increasing rate past the yield point of the material. This is because during plastic deformation, the sample must be strained at an increasing rate to generate the desired tensile force. For this reason, mechanical testing standards of fibers, yarns, plastics, and composites require tensile testing using a fixed strain rate or extension rate [86-89]. It is therefore selected that voltage-controlled tests will be conducted when assessing the high current behavior of CNT yarns and SWCNT wires, due to the parallel between voltage-controlled electrical tests and strain-controlled mechanical tests.

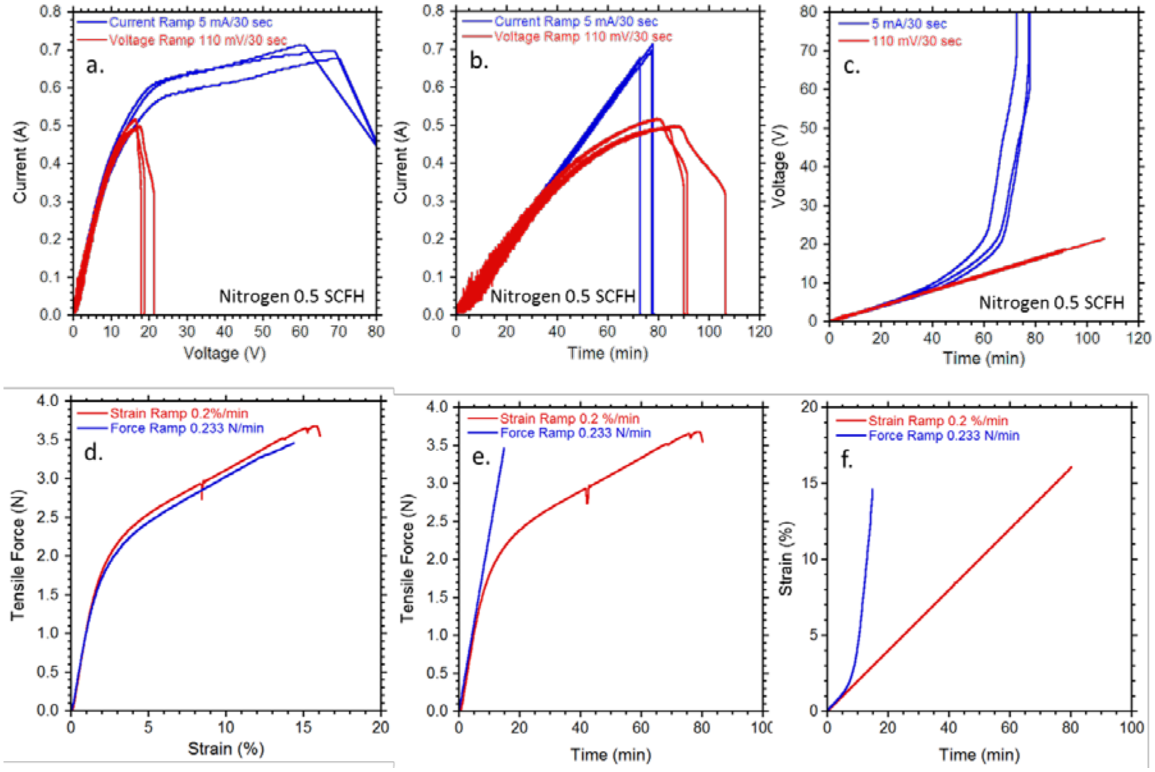

Figure 38. a. Measured current as a function of applied voltage of six CNT yarns with either a current-controlled test with 5 mA increases every thirty seconds or a voltage controlled test with 110 mV increases every 30 seconds. b. The measured current of the samples from panel a, plotted as a function of the test time. c. The applied voltage on the samples from panel a, plotted as a function of test time. d. Measured tensile force as a function of applied strain for CNT yarns with either a force-controlled test where force in increased by 0.233 N/min or a strain-controlled test where strain is increased by 0.2 %/min. e. The measured tensile force from both samples in panel d, as a function of test time. f. The applied strain from both samples in panel d, as a function of test time.

5.3 Ambient Gas Dependence of CNT Yarn and SWCNT Wire Failure

With the testing conditions determined, several CNT yarns and SWCNT wires were brought to their high-current failure points for characterization and failure analysis. The effects of three ambient gasses were determined. Air was selected as one ambient gas due to its prevalence in practical scenarios. Nitrogen gas allowed for testing in an environment with similar thermal conductivity to air but without the presence of oxygen, which can react with carbon at high temperature ("oxidation"). Finally, helium provided a second non-oxidative environment with higher thermal conductivity than nitrogen for determination of the effect of the ambient gas thermal conductivity. Three CNT yarns were brought to failure in each of these three gasses flowing at 0.5 SCFH by increasing the applied voltage (a voltage-controlled test) by 150 mV every 5 seconds. The current as a function of applied voltage from this testing is plotted in Figure 39. The three CNT yarns brought to failure in air reach an average maximum current of 330 mA and fail immediately – their maximum current and failure current are the same. The maximum current in nitrogen reached an average of 635 mA, a 94 % increase over the maximum current in air. This increase is likely due to a difference in failure modes. In air, once the CNT yarn reaches a temperature high enough for it to oxidize, the resistance rapidly increases and the wire fails abruptly. In nitrogen, oxidation of the wire is suppressed due to the lack of oxygen presence and the wire must reach a temperature high enough to thermally decompose [90]. CNT yarns in helium reach an average maximum current of 880 mA, a 38 % increase over the maximum current in nitrogen and a 138 % increase over the maximum current in air. The increase in maximum current in helium compared to nitrogen is due to the higher thermal conductivity of helium, which allows for rapid wire conductive cooling, requiring a higher current for joule heating to overcome conductive cooling and reach the thermal decomposition temperature for the CNT yarn.

Using the average cross-sectional area determined by cross-sectional SEM imaging laser-cut samples of CNT yarn lot 60027 (see Figure 40), the maximum currents recorded in each ambient gas were converted into current densities. In air, the average maximum current density reached by CNT yarns was 15 MA/m2. The average maximum current density attained in nitrogen was 30 MA/m2, 1.9x greater than attained in air. The average maximum current density measured in helium was 41 MA/m2, 1.4x greater than in nitrogen and 27x greater than in air. This data guides wire coating techniques toward materials that have high thermal conductivity to dissipate heat from the wire and have low permeability to oxygen to prevent wire oxidation at elevated temperature.

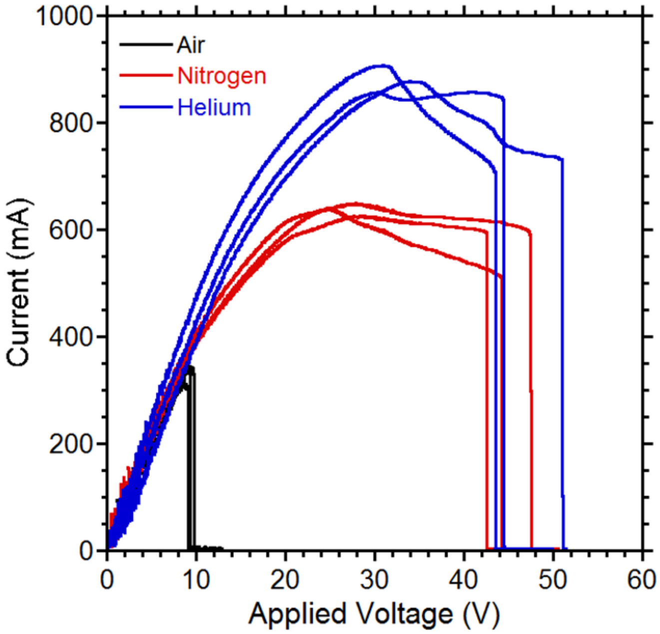

Figure 39. Measured current as a function of the applied voltage on nine CNT yarn samples in 0.5 SCFH of the specified ambient gas.

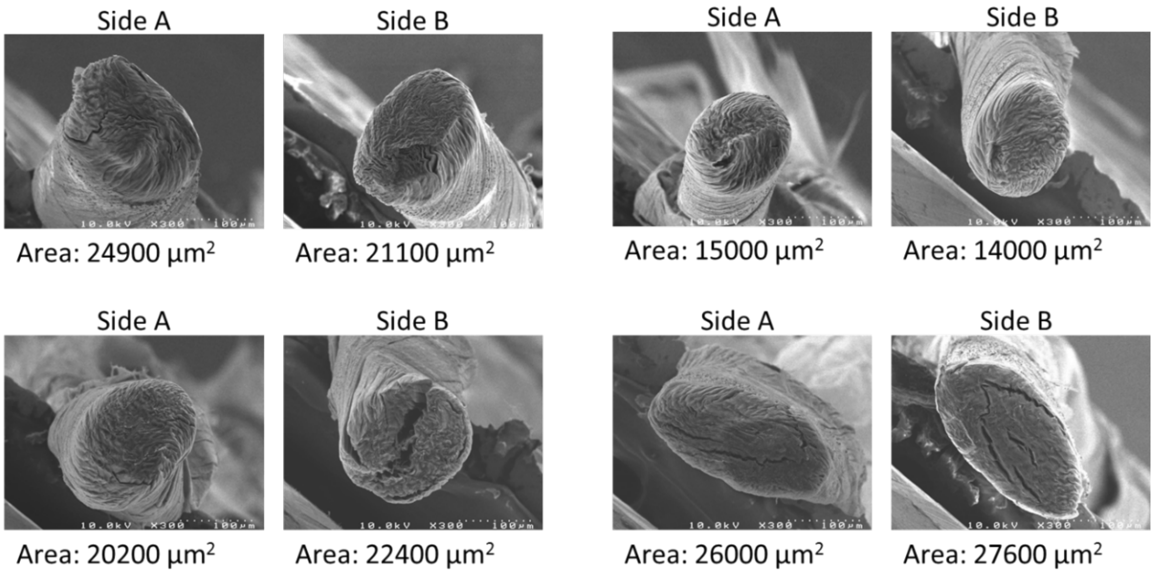

Figure 40. Cross-sectional SEM images of both sides of 4 laser-cut CNT yarn lot 60027 samples and the accompanying area measurements recorded from each image.

Optical microscopy images of the failure points of the CNT yarns tested in Figure 39 were acquired and representative images from this set can be seen in Figure 41. CNT yarns brought to failure in air had a long taper (approximately 10 mm taper on either side of the failure point) towards their failure point with several discernable regions. A coating of red material, presumably oxidized residual iron catalyst from the CNT yarn synthesis can be seen in regions approximately 5-8 mm from the failure point (Figure 41a). Closer to their failure point in air (Figure 41b), spheres of metal can be seen on the wire surface (see Figure 41c for detail). There are presumed to be ripened droplets of residual iron catalyst. Catalyst is present on the surface of the CNT yarns that failed in air since the high temperatures were able to oxidize the carbonaceous coatings on the catalyst particles, leaving them to oxidize further from the failure point or ripen into droplets closer to it. Optical microscopy images of CNT yarn failure points in nitrogen (Figure 41d) and (Figure 41e) do not display catalyst features on their surfaces and have much more abrupt failure points than the yarns that were brought to high current failure in air. This demonstrates the strong effect of oxygen presence during wire failure.

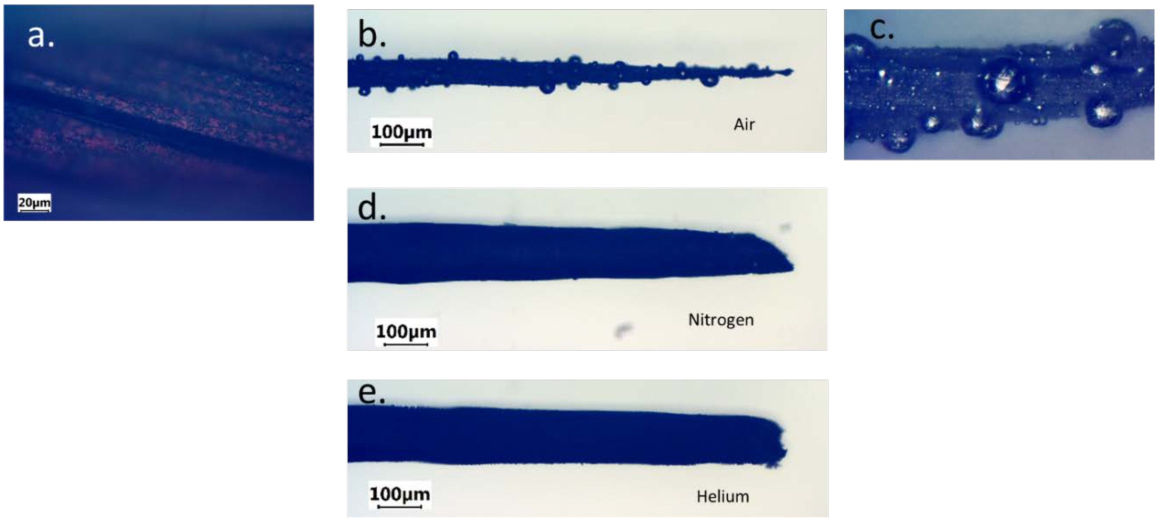

Figure 41. Optical microscopy images of CNT yarns after failure. a. ~7 mm from failure point in air. b. Failure point in air. c. ~0.5 mm from failure point in air, same scale bar as panel a. d. Failure point in nitrogen. e. Failure point in helium.

For further visual analysis of the CNT yarn failure points, the CNT yarn segments were characterized by SEM after failure. SEM images of the tip of the CNT yarn failure point in air show few CNTs with several spheres of catalyst present (Figure 42a). Approximately 1 mm from the failure point, several scattered spherical catalyst particles can be seen in the CNT network. It is important to note that while the catalyst morphology changes from a CNT yarn not exposed to high currents, the CNTs in the yarn appear largely unchanged. The application of heat essentially oxidizes the impurities near the failure point, purifying the wire. Figure 42b shows and SEM of the point of failure of a CNT yarn in nitrogen. A highly-conical failure point is not observed in this image as was in Figure 42a, instead there is a blunt failure point where the wire abruptly ends without much taper. A higher magnification SEM image of the CNT yarn in Figure 42b, approximately 1 mm from the failure point, is seen in Figure 42e. The yarn structure in this image is largely unchanged from as-received CNT yarns. SEM images of the high-current failure point of CNT yarns in helium (Figure 42c) resemble those of the high-current failure point in nitrogen – a blunt failure point without much taper in which the constituent CNTs appear unchanged from the as-received CNT yarn.

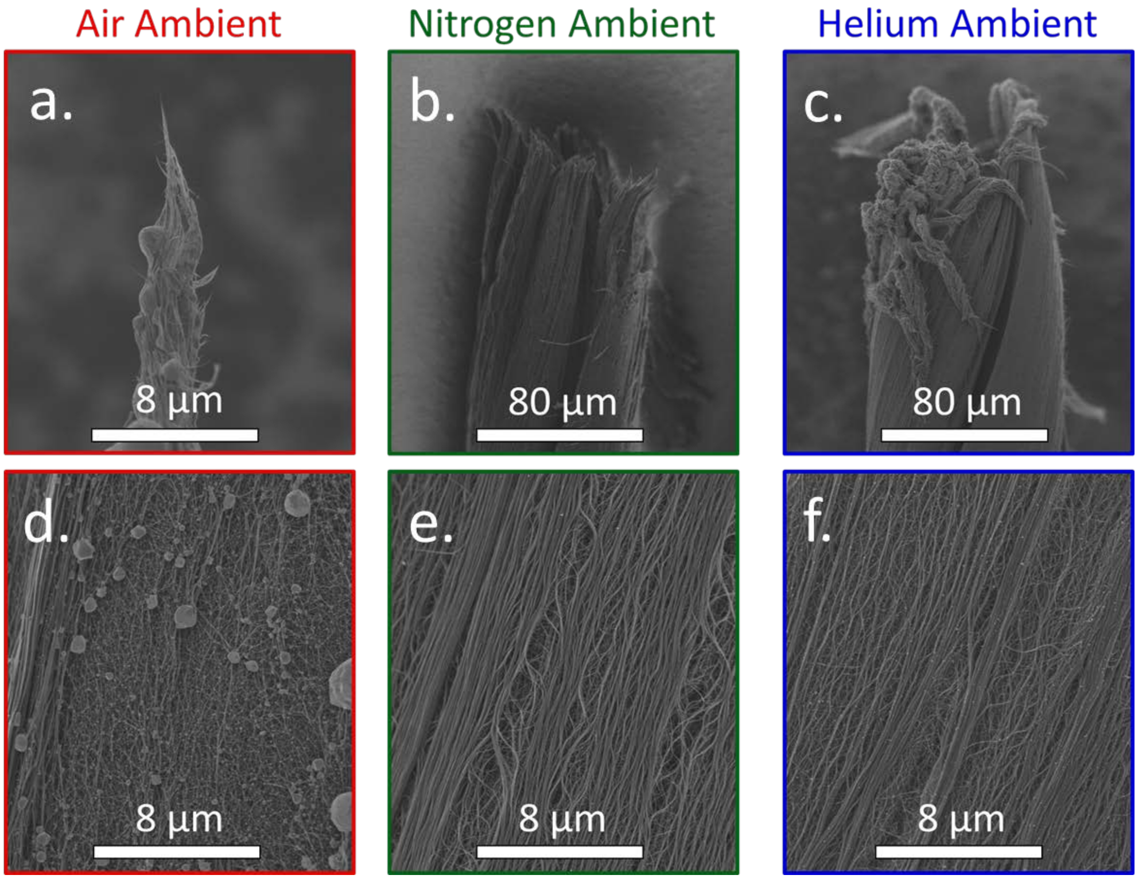

Figure 42. Top Row: SEM images of high-current failure point of a CNT yarn in: a. Air, b. Nitrogen. c. Helium. Bottom Row: SEM image of CNT yarn approximately 1 mm from high-current failure point in: d. Air, e. Nitrogen, f. Helium.

High-current failure tests were conducted with SWCNT extruded wires for comparison to CNT yarns. SWCNT wires were fabricated by dispersing purified laser-SWCNTs in CSA at a weight loading of 61 mg SWCNT per mL CSA and extruding this dispersion through a 22 Ga stainless steel syringe needle at 0.1 mL/min into a 66 cm deep cylinder of -10 °C acetone. Wires were then stretched and dried under tension before characterization (see Figure 33). Cross-sectional analysis indicates the conductivity of these wires is ~5 MS/m. Segments of extruded wire were mounted in the same test fixture as the CNT yarns for failure current measurements using two-point measurements with a probe separation of 3 cm. Applied voltage was increased by 100 mV every 2.5 seconds until wire failure. Results of this testing in three ambient gases are presented in Figure 43. In air, current increases linearly with increasing applied voltage until 240 mA of current are attained, after which there is an abrupt drop in current to ~180 mA. Thus current is sustained with increasing voltage until the wire fails at 8 V. In nitrogen, the same behavior is observed until the 8 V point, but instead of the wire failing and becoming an open circuit as in air, the current begins to increase linearly again with increasing applied voltage. This difference is due to the lack of oxygen present in the nitrogen environment. After reaching a maximum current of 360 mA (1.5x greater than the maximum in air) at 26 V, the current begins to decrease until the wire abruptly fails at 34 V. The high-current behavior of extruded SWCNT wires in helium resembles that of extruded SWCNT wires in nitrogen: there is a linear increase in current with increasing applied voltage until 440 mA is reached at 5 V followed by an abrupt drop in current to ~ 300 mA which is maintained until 18 V, when the current begins to increase linearly once again to a maximum current of 570 mA (1.6x greater than the maximum in nitrogen) at 44 V, when the current begins to decrease with additional applied voltage. To explain these multiple regimes of current increase and decrease with applied voltage, the change in resistance of the SWCNT wire is investigated in the next section.

The currents attained in the SWCNT wires are lower than those attained in the CNT yarns. For comparison to other wire types, the maximum currents have been converted to current densities. The maximum current density in air of an extruded

SWCNT wire is 180 MA/m^2, 11.5x greater than that of CNT yarns in air. The maximum current attained by extruded SWCNT wires in nitrogen was 260 MA/m2, 8.9x greater than that of CNT yarns in nitrogen. The maximum current attained by extruded SWCNT wires in helium was 420 MA/m2, 10.2x greater than that of CNT yarns in helium. Greater current densities were achieved by extruded SWCNT wire than CNT yarns likely due to the higher purity, better alignment, and smaller diameter of extruded SWCNT wires, as well as the higher conductivity of the individual SWCNTs when compared to MWCNTs.

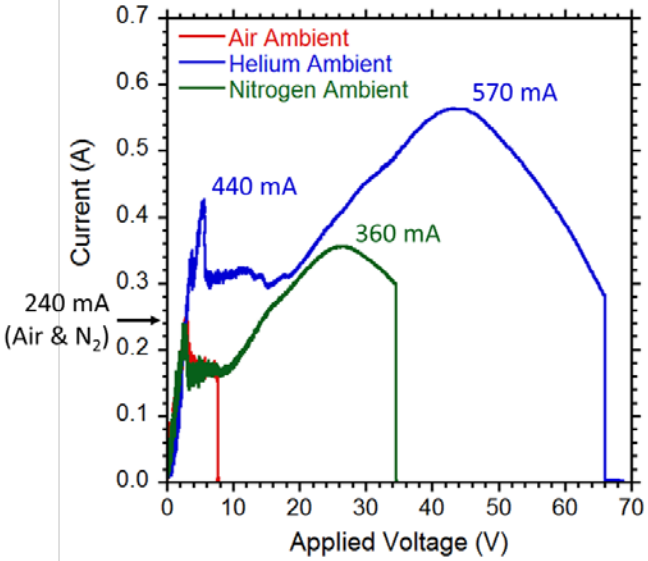

Figure 43. Measured current as a function of applied voltage for three segments of extruded SWCNT wire under three different ambient gasses.

The instantaneous resistance (applied voltage divided by measured current) from each of the tests in Figure 43 have been plotted as a function of the applied voltage in Figure 44 in order to elucidate the origin of the current-voltage behavior of SWCNT wires under high current in different ambient gasses. Extruded SWCNT wires in all three ambient gasses are constant at low voltages, but eventually the resistance begins to climb linearly with additional applied current. This explains the initially linear regions of the current-voltage curves in Figure 43, followed by the constant current regimes. After a period of linear increase in resistance, the SWCNT wire in air is generating enough heat from joule heating (since power dissipation is increasing as resistance increase since $P = I^2R$) that the oxidation takes place and the wire fails. This failure is avoided in the nitrogen and helium ambient conditions due to the lack of oxygen present. Instead, in these wires, after the resistance increases linearly for some time, it begins another region of remaining relatively constant with increasing applied voltage until the resistance begins to increase exponentially until the wire fails. The region of constant resistance with increasing voltage in Figure 44 corresponds to the second region of linear current increase in Figure 43. When the resistance begins to increase exponentially, additional applied voltage is not enough to keep the measured current rising, and this region of Figure 44 corresponds to the region of decreasing current with increasing applied voltage in the nitrogen and helium testing environments in Figure 43.

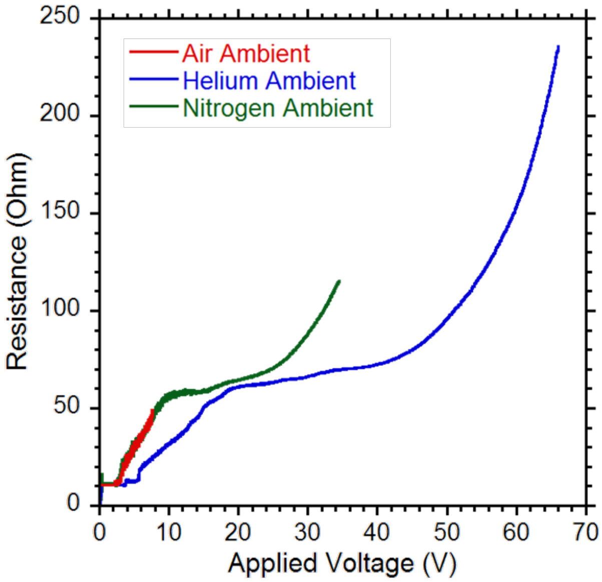

Figure 44. Instantaneous resistance (applied voltage divided by measured current) calculated from the data in Figure 43 as a function of the applied voltage.

The origin of the different regions of resistance change can be explained by oxidation, wire de-doping, and wire degradation. The region of constant resistance at low applied voltages occurs before wire temperature has reached sufficient temperatures to cause desorption of residual acid dopants, water, and oxygen. The region of linear resistance increase corresponds the de-doping region, where currents are high enough for the heat generated to cause a loss of adsorbed dopants, which causes an increase in wire resistance. Once the dopants have completely desorbed in the nitrogen and helium test scenarios, the resistance is once again constant until high enough temperatures are reached for degradation of SWCNTs in the wire to begins, and the resistance increases further due to the loss of these conductors.

These regimes of resistance change have been explored previously in the literature. In [83], similar high current tests were conducted to those used in this work.

The authors use a current-controlled test in vacuum and plot current density vs resistance relative to the initial resistance of extruded CNT fibers before high-current testing, and the results can be seen in the main panel of Figure 45b. The data from the present work on extruded SWCNT wires is plotted in Figure 45a as applied voltage vs instantaneous resistance so that the two datasets can be easily compared. The authors of [83] demonstrate the reversibility of resistance changes in the regions where resistance increases due to de-doping and degradation (labeled Regime 2 and Regime 4, respectively) and the reversibility of the current-voltage characteristics in the regions where resistance is constant (labeled Regime 1 and Regime 4, respectively).

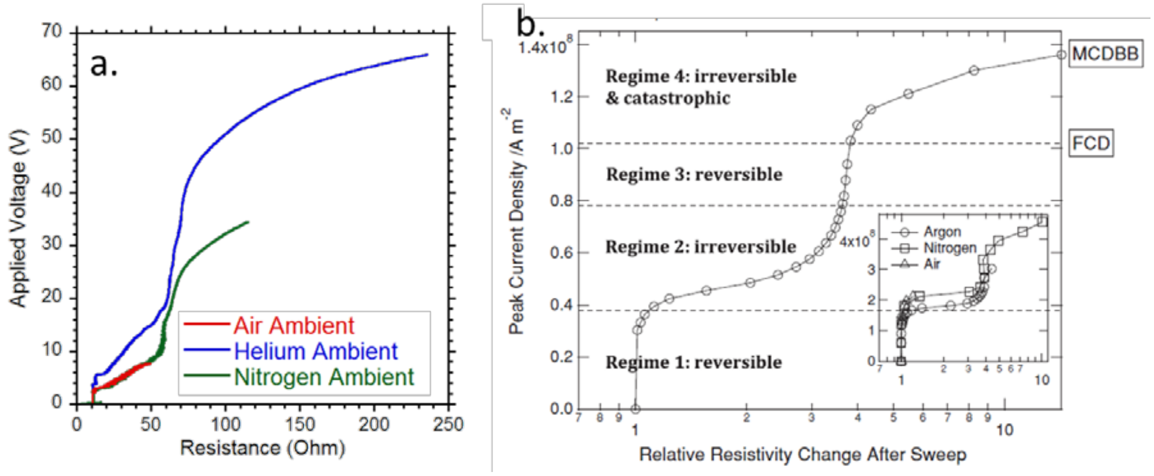

Figure 45. a. Applied voltage plotted as a function of the instantaneous resistance of extruded SWCNT wires tested in different ambient gases derived from the data in Figure 43 and Figure 44, which derive from a voltage-controlled test. b. Plot of current density as a function of relative resistance change of an extruded CNT yarn in vacuum from current-controlled testing in which repeated cycles of current were applied with each cycle reaching a new maximum value, adapted from [83].

After extruded SWCNT wire samples were brought to their high-current failure in air, nitrogen and helium, samples were subjected to SEM characterization for failure analysis. While taper in the failure point of SWCNT wires when tested in air was greatly reduced from that observed in CNT yarns brought to high-current failure in air (Figure 46a), a conical failure point is still observed. In higher-magnification SEMs of the SWCNT wire surface near (<80 µm away) the failure point in air, no metallic impurities are present and the SWCNT network is largely intact (compare to as-produced SEM images in Figure 33). The failure point of extruded SWCNT wires tested in nitrogen displays less taper than the failure point from samples tested in air (Figure 46b). In higher magnification SEMs of the SWCNT network near (<80 µm away) the failure point in nitrogen, degradation of the SWCNT network is apparent as the bundles have become shortened, porous, and fractured (Figure 46e). Similar behavior is seen in the high-current failure point in helium: a blunt failure point with very little taper (Figure 46c) and the nearby SWCNT network has become highly degraded (Figure 46f).

Comparisons between the SEMs in Figure 46 and those in Figure 42 can elucidate differences in failure between CNT yarns and SWCNT wires, and between failure modes in different ambient conditions. The change in catalyst morphology in

The SWCNT wire brought to high-current failure in air does not show network degradation because only the SWCNTs near the hottest potion of the wire oxidized. Once oxidation took place during the test, the SWCNT wire became a short and began cooling before an extended region of the wire reached high enough temperature to oxidize. In the nitrogen and helium environments, the entire region of the SWCNT wire between the electrical contacts rises in temperature (as evident from the wire glow) and so wire degradation takes place in SWCNT bundles further from the failure point.

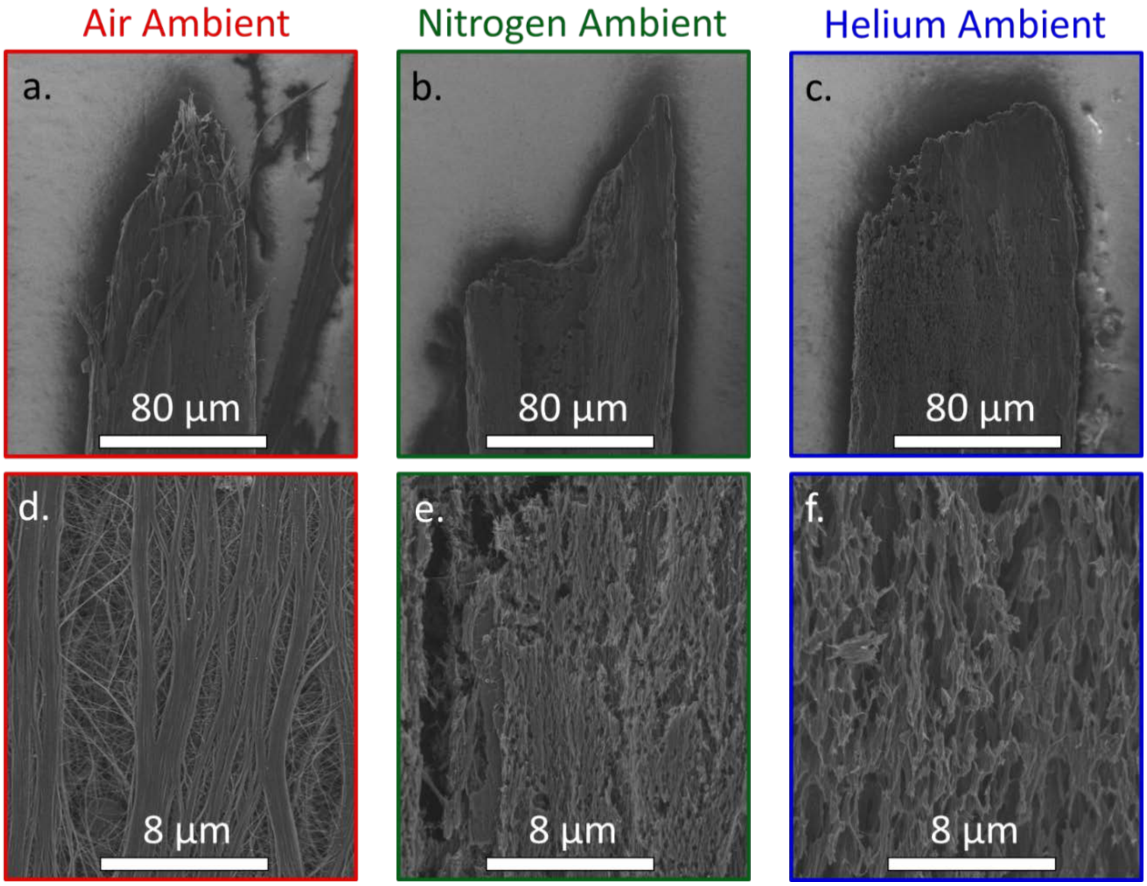

Figure 46. Top Row: SEM images of high-current failure point of extruded SWCNT wires in: a. Air, b. Nitrogen. c. Helium. Bottom Row: SEM images of extruded SWCNT wires <80 µm from their high-current failure point in: d. Air, e. Nitrogen, f. Helium.

To quantitatively assess the failures of CNT yarns and extruded SWCNT wires, Raman spectroscopy was performed at the failure points, and at 1 mm intervals from the failure point along the yarn/wire axis. In Figure 47a, the D/G ratio in the 5 mm closest to the failure point is below that of the as-received CNT yarn. This is further evidence that the high temperatures and oxidation removed carbonaceous impurities which do not have a regular structure and contribute to the D/G ratio [91]. Increased D/G ratio past the 5 mm point in this sample may be due to the presence of oxidized catalyst coating on the surface of the yarn, which becomes more continuous further from the failure point where there is insufficient thermal energy to cause droplet ripening. In extruded SWCNT wires, the catalyst particles have been removed during purification of the material prior to dispersion and extrusion, and so no decrease in the D/G ratio is observed (Figure 47b). Instead, in the sample brought tot high-current failure in air, the D/G ratio is increased due to the oxidation of SWCNTs near the failure point, but because this oxidation is localized, the D/G ratio tends back toward the D/G ration of an as-extruded sample after 3-4 mm. In contrast, the D/G ratio is elevated in the entire region measured in the SWCNT wire that was brought to high current failure in nitrogen, since the entire region of the wire between the electrical contacts was elevated in temperature.

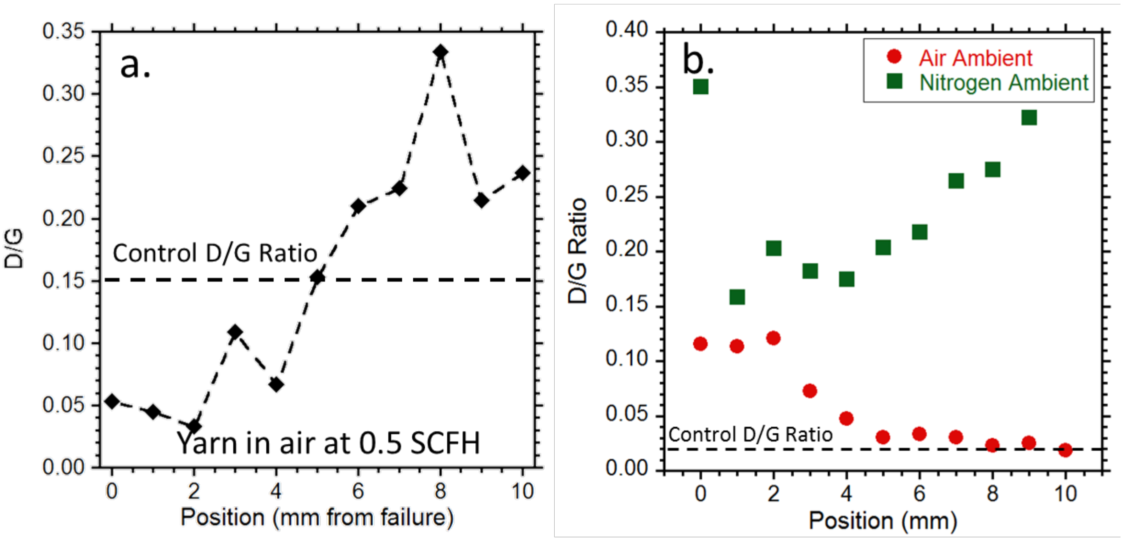

Figure 47. Raman D/G ratios as a function of distance from the high-current failure point. a. measured on a CNT yarn brought to high-current failure in air. b. Measured on extruded SWCNT wires brought to failure in air (red circle data points) and in nitrogen (green square data points).

5.4 High-Current Wire and Yarn Conclusions

The behavior of both commercially available Nanocomp Miralon CNT yarns and extruded SWCNT wires has been characterized under three different ambient gases and failure analysis has been conducted. A test chamber was constructed to allow for a DC high-voltage power supply to apply controlled currents and voltages to yarns and wires under controlled ambient conditions. High-current tests were conducted on CNT yarns in both current-controlled and voltage-controlled scenarios. The current-voltage characteristics from yarns tested under these two conditions varied greatly, and this variance was ascribed to rapid voltage increases per unit time in the current-controlled scenario. By drawing analogy to mechanical stress-strain testing, voltage-controlled testing is determined to be the more informative testing type.

CNT yarns in nitrogen and helium failed at 94 % and 169 % greater currents than those in air due to the lack of oxygen in their surroundings. Greater failure current in helium is a product of the greater thermal conductivity in helium than nitrogen or air, which increases the current required for joule heating and convective/conductive/radiative cooling to equilibrate at a high enough temperature for wire degradation to cause failure. Extruded SWCNT wires failed at current densities of 180 MA/m^2 in air, 11.5x greater than those of CNT yarns in air. Maximum current densities of 420 MA/m^2 for extruded wires were reached in helium. SEM and Raman spectroscopy failure analysis of CNT yarns and SWCNT wires demonstrated that the lack of impurities in SWCNT wires was an enabling factor in the enhancement of their maximum current over CNT yarns.

Chapter 6. Doping of Carbon Nanotube Wires for Enhanced Conductivity

Tasks:

- Identify and study chemicals species which enhance bulk CNT conductivity.
- Determine the time-dependence of CNT doping
- Utilize UV-vis spectroscopy to quantify dopant uptake on bulk CNT materials for various dopants.
- Evaluate the effects of solvent selection on conductivity enhancement and dopant adsorption amount for IBr dopant.

6.1 Chapter Abstract

Purified commercially available carbon nanotube (CNT) sheet and yarn materials have been chemically doped in solutions of IBr using varying solvents to enhance the CNT bulk electrical conductivity. Time dependent optical absorption spectroscopy was employed to quantify IBr adsorption onto the CNT samples and results correlate dopant adsorption with CNT conductivity enhancement. Two independent solvent systems were evaluated (hexanes and ethanol) leading to 40% greater conductivity for CNTs doped with IBr in hexanes compared to CNTs doped with IBr in ethanol. A comparative analysis of IBr in 9 solvents with varying polarities at 2.1 g IBr/L solvent was employed to evaluate CNT doping efficacy and supports a mechanism whereby saturated solutions in hexanes and water favor dopant-CNT interactions that shift the equilibrium in favor of dopant adsorption, and yield the highest CNT electrical conductivity. Saturated dopant solution loadings of 10-20 g IBr/L hexanes resulted in the maximum electrical conductivity of 0.85 MS/m compared to an initial CNT conductivity of 0.1 MS/m. The optimal IBr doping conditions from the work (60 minute exposure of 20.7g IBr/L hexanes) were applied to commercial CNT yarns leading to an improvement in

conductivity of 13.4× to a value of 1.4 MS/m. High voltage testing in air shows a 36% increase in maximum current carrying capacity at failure compared to as-received yarn. Thus, proper combination of dopant-solvent leads to enhanced electrical transport properties in advanced carbon conductors.

6.2 Introduction to Chemical Doping of CNTs

Bulk carbon nanotube (CNT) electrical conductors are of interest for aerospace and terrestrial electrical transmission applications due to their low density, flexure tolerance, chemical stability, and high electrical and thermal conductivities.[69], [92] A critical need for improvement of these materials is the enhancement of the electrical conductivity of bulk CNT structures towards the exceptionally high intrinsic conductivity of individual CNTs. Conductivity enhancements of CNT conductors have been obtained previously through the optimization of conductor fabrication, and by the incorporation of chemical dopants [93-95]. Several methods of dopant delivery, such as gaseous deposition and aqueous soaking, have demonstrated success depending on the specific dopant species of interest [53], [96], [97]. Promising work using I_2 and $KAuBr_4$ to achieve exceptionally high bulk CNT conductivity [53], [96], [98] motivates the study of iodine and bromine containing compounds, and recent work with interhalogen compounds, such as iodine monobromide (IBr) and iodine monochloride (ICl), [97], [99], [100] has shown an increase in the conductivity of CNT thin films and wires. Previously, these dopants have been applied to CNT materials using either water [97] or dichloromethane [100] as a solvent without explicit study of the effects of varying dopant delivery solvent. Additionally, while ICl is a liquid at room temperature, IBr is a sold.

Therefore, doping in neat IBr requires that either a solvent be used at room temperature, or that doping take place in melted IBr. Doping in melted IBr has the undesired effect of leaving a dopant "crust" on CNT samples when it returns to room temperature. Thus, there is motivation to study and refine the delivery methodology for these dopants to further enhance the electrical conductivity of doped CNTs.

Chemical doping of CNTs refers to intercalation of the dopant species into void spaces between CNT aggregates, bundles, and onto the CNT surfaces in a solid bulk structure [95], [101]. The dopant species shifts the Fermi level of individual CNTs, thereby altering their *intra*-CNT electronic properties [101]. The presence of chemical dopants also influences charge transport between individual CNTs (i.e., *inter*-CNT) in a network [102-104]. Therefore, chemical dopants can be developed and exploited to enhance the electrical conductivity of bulk CNT structures for applications such as power transmission and electrical contacts, which require high conductivity materials. Solution phase doping represents a scalable strategy to introduce many solid-phase species, but can be highly influenced by solvent selection, exposure time, and concentration [69], [98].

In the present work, a systematic study of solvent type has been conducted, and its influence on IBr adsorption and resulting bulk CNT electrical conductivity has been determined. IBr adsorption is quantified by adapting published techniques that uses optical absorption spectroscopy to monitor changes in solution concentration [105]. Additional studies investigate the effects of IBr concentration on CNT doping performance and evaluate the impact of solution concentrations exceeding the solubility limit. Overall, results show that CNT conductivity enhancement is dependent on the combined effects from the dopant-solvent, dopant-CNT, and CNT-solvent interactions. Using these results, CNT yarns were doped under determined conditions to increase conductivity more than an order of magnitude to show influence of enhanced dopant on high current carrying capacity carbon conductors.

6.3 Experimental

6.3.1 Doping Solution and CNT Preparation

IBr (98% purity) was purchased as a solid from Sigma-Aldrich. Acetone, dimethyl sulfoxide (DMSO), and isopropanol (IPA) were purchased from BHD (ACS reagent grade). Chloroform (0.5 – 1.0 % ethanol stabilizer, 99.9% purity), dimethylacetamide (DMA, >99.9% purity), ethanol (ACS reagent grade), and hexanes (mix of isomers, ACS reagent grade) were purchased from Sigma-Aldrich. Spectrophotometric grade methanol (>99.8% purity) was purchased from Alfa Aesar.

Carbon nanotube sheet material (lot # 70160) was purchased from Nanocomp Technologies, Inc. The CNT material was purified using a previously reported procedure[97] by thermal oxidation in a quartz tube furnace under flowing air by ramping from room temperature to 520 °C at 10 °C/min then immediately removing the sample from the furnace for cooling. Thermal oxidation was followed by a 30 minute soak in 37% hydrochloric acid (Sigma-Aldrich, ACS reagent grade), a 1 h dry in a vacuum oven at 80 °C, and an additional thermal oxidation from room temperature to 520 °C at 10 °C/min. The resulting purified sheet material was cut into 7 mm square samples with a razor blade for doping studies and characterization. Raman spectra were recorded from samples after purification and after doping using a JY-Horiba Labram-HR using a 633 nm excitation laser.

Doping solutions were prepared by dispensing melted IBr at 50 °C and massing the resulting aliquots in glass vials sealed with polytetrafluoroethylene-lined caps on an Ohaus EP214C Explorer Pro Analytical Balance. The appropriate volume of solvent was then added to the cooled, solid mass of IBr to create solutions of the desired concentration. All CNT doping was achieved by soaking the CNT squares in these solutions at room temperature immediately after IBr dissolution.

6.3.2 Electrical Conductivity and Optical Absorption Characterization

Electrical resistance was measured for each CNT square and CNT yarn using a four-point probe and van der Pauw method following purification and again after doping using a National Instruments NI PXI-5652 source/measure unit and an NI PXI-4071 digital multimeter at ~20°C. Electrical conductivity was computed based upon the measured resistance values and the cross-sectional area of the sheets or yarns based upon electron microscopy. All plotted electrical conductivities of CNT sheets are the averaged result of three conductivity measurements. The standard deviation in the conductivity of the starting material was 21% of the mean, while standard deviations in doped sample lots were 3 – 28% of their means.

Optical absorption studies were conducted using a Perkin-Elmer Lambda 900 spectrometer using a 1 cm path-length, quartz cuvette with a polytetrafluoroethylene stopper plug to minimize solvent evaporation. Absorption data was collected from 200 to

600 nm in 1 nm intervals using the set-up described in Figure 48, with each scan occurring every 10 min for 100 min. Beer's Law was used to relate the percent change in absorbance to percent change in concentration, which is attributed to IBr adsorption onto the CNT sample, and can be used to compare relative adsorption of IBr between solvents. The peak used in this analysis is assumed to be representative of total IBr concentration and no peak assignments have been made to particular dissolved halogen species.[106] Therefore, the amount of IBr adsorbed onto the CNT samples was calculated using the difference of relative changes in optical absorbance between a control sample and a CNT-containing sample using the equation at the same wavelength:

$$q = \left(\frac{A_{\mathrm{C}}(t)}{A_{\mathrm{C}}(0)} - \frac{A_{\mathrm{CNT}}(t)}{A_{\mathrm{CNT}}(0)}\right)\left(\frac{C_i V M}{M_{\mathrm{CNT}}}\right) \tag{7}$$

Where q is the mass of IBr adsorbed onto CNT sample per mass of CNT (expressed in this work as μg/mg), $A_C(t)$ is the optical absorbance of the control sample (IBr solution without CNT sample present) at time t, $A_{CNT}(t)$ is the optical absorbance of the IBr solution with a CNT sample present in the cuvette at time t, C_i is the initial concentration of the IBr solution that the CNT sample was immersed in (in mol/L), V is the volume of solution in the cuvette (in L), M is the molar mass of IBr (in μg/mol), and M_{CNT} is the mass of CNTs in the cuvette (in mg). All solutions were prepared immediately prior to time-dependent optical absorption studies to ensure equal solution age. The solution concentration was approximately 0.2 g/L (1 mM) and the cuvette volume was 3.2 mL for all optical absorption studies. IBr concentrations for doping studies are presented in units of mM for solutions below the solubility limit when complete dissolution of the IBr is expected (such as for spectroscopy). Additionally, concentrations are supplied in units of g/L to reflect the amount of IBr added to a given volume of solvent, which is potentially relevant in scenarios when more IBr is present than can be dissolved in a given solvent.

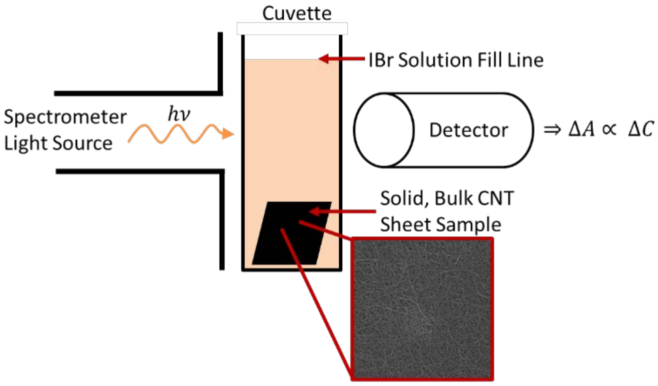

Figure 48. Schematic of optical absorbance spectroscopy experimental set up, where a solid CNT sample is present in the dopant solution within the cuvette. ΔA is the change in optical absorbance at a given wavelength between a control doping solution sample and a doping solution sample with CNTs present at a given time after solution preparation , and ΔC is the change in doping solution concentration between its as-prepared concentration and its concentration at a given time.

6.3.3 IBr Time-Dependent Conductivity Study

CNT samples were exposed to IBr in ethanol (selected as the solvent for the initial studies due to high IBr solubility) over time using two methods. The first method was an iterative approach, whereby three CNT samples were each soaked in separate 5 mL solutions of 0.2 g/L (1 mM) IBr in ethanol for ten minutes, removed from the solution, blotted dry, and electrically characterized after five minutes of drying at room temperature under ambient conditions. The CNT samples were returned after characterization to the IBr doping solution and the process was repeated 6 times for a total doping time of 60 min. The second method was a single time exposure, whereby CNT samples were immersed in an IBr solution for 30, 45, 60, or 90 minutes each before being dried and characterized in the same manner as in the first method.

6.3.4 Tensile and High-Current Characterization of CNT Yarns

The efficacy of IBr doping in high-current applications was tested on similar CNT material in a conductive yarn format. Nanocomp Miralon® yarn (lot # 60027) was used as-received, without purification. Stress-strain properties were determined using a TA Q800 Dynamic Mechanical Analizer (DMA) with a film-tension clamp and an approximately 1 cm gauge length. Mechanical testing took place by increasing the strain by 0.5 %/min until yarn failure. The high-current characteristics of both the as-received yarn and yarns treated with IBr were measured using an Arbin BT-2000 power supply by applying a constant current through two source/measure probes (separated by 25 mm of yarn), which was increased every 30 seconds by 10 mA until wire failure, similar to procedures previously used to test high-current characteristics of CNT wires and yarns.[83], [84]

6.4 Results of IBr Doping Studies

Initial studies were conducted to examine solvent effects on the bulk CNT conductivity using I_2, which is a commonly reported CNT dopant in the literature [53], [96]. Purified CNT samples (see inset of Figure 49a) with a conductivity of 1.0×10^5 S/m were exposed to 5 mM solutions of I_2 in hexanes and ethanol for 1 hour at 20°C, after which time, the samples were removed from the dopant solution and air dried for 5 min.

Figure 49a shows that the CNT samples doped with I_2 in hexanes had higher conductivities than those doped with I_2 in ethanol (3.4×10^6 S/m compared to 2.3×10^6 S/m respectively).

Optical absorption spectroscopy is used to determine dopant adsorption onto CNT samples. Figure 49b and 1c show the I_2 optical absorption peaks in ethanol and hexanes respectively, and their decay over time when CNT samples are present in the solution. Note that these peaks occur at different wavelengths (445 nm in ethanol and 520 nm in hexanes), and corresponding to different solution colors as shown in the insets of Figure 49b and c, respectively. This is due to the solvatochromic shift that I_2 experiences in solution, which indicates differing interactions between the solvents and the I_2 [107]. The black data points in Figure 49d demonstrate a less-than 1% change in the optical absorbance intensity at the I_2 peak maxima of the I_2 solutions in hexanes and ethanol without CNTs over time. Optical absorbance intensity from the hexanes and ethanol solutions with CNTs present is displayed as the red data points in Figure 49d, which indicates a significant reduction in absorbance intensity at the I_2 peak maxima over time. Figure 49e shows the mass of dopant adsorbed over time using equation (7), normalized to the mass of the CNT sample present. This figure indicates ~50% greater adsorption of I_2 onto the CNTs when using hexanes as a solvent than ethanol at 60 min doping time (38 µg I_2 / mg CNT compared to 25 µg I_2 / mg CNT, respectively). Thus, while both I_2 doping solutions increase bulk CNT conductivity, the hexanes doping solutions promotes greater I_2 adsorption onto the CNTs and therefore, a greater conductivity enhancement is observed when doping in hexanes compared to ethanol. Therefore, studying the dopant delivery solvent for novel dopants of interest, such as IBr, in addition to I_2 is important for optimizing their enhancement of CNT electrical conductivity.

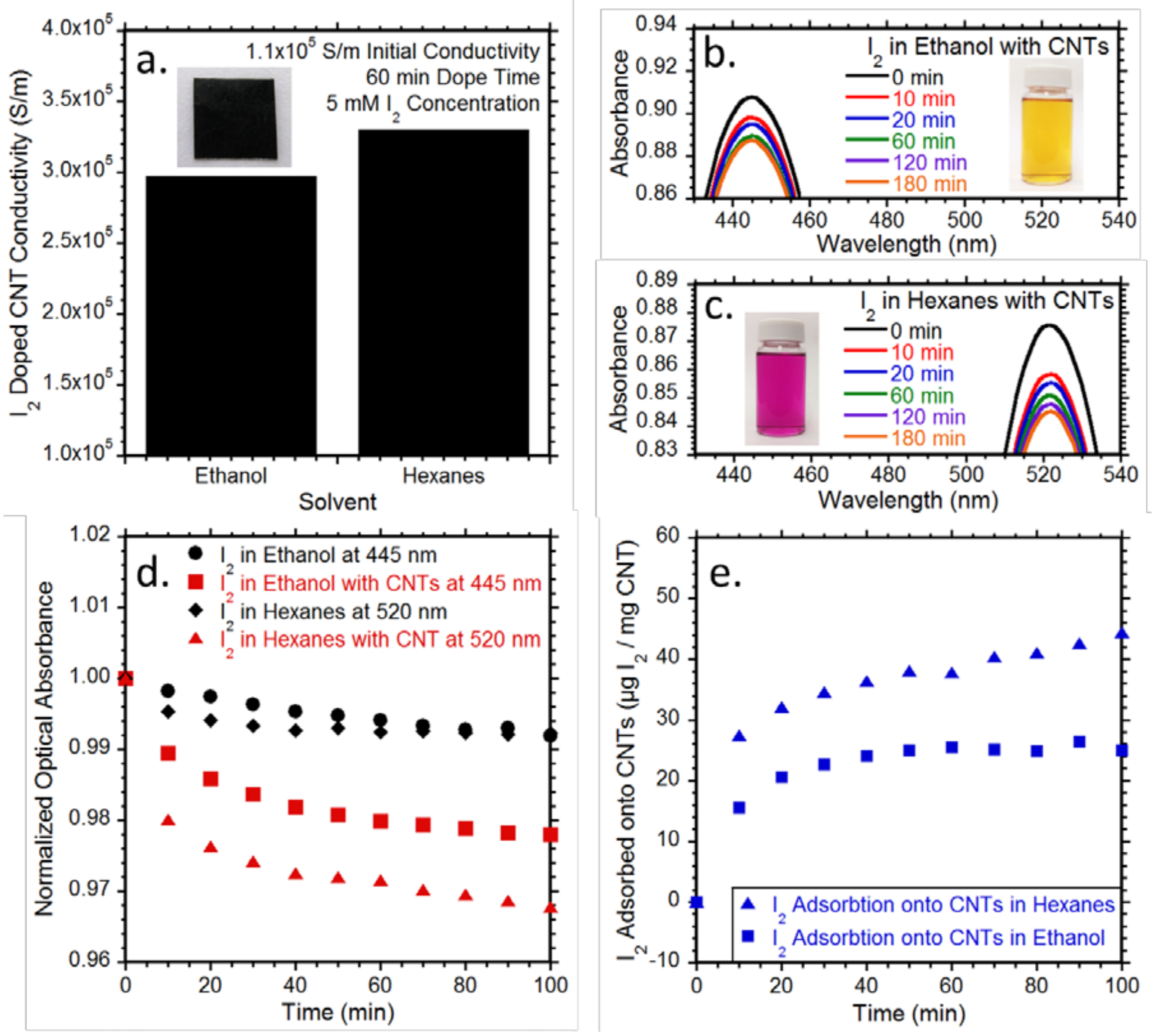

Figure 49. (a.) Conductivity of CNT samples doped with 5 mM I_2 in ethanol and hexanes for 60 min. Inset shows an example of a purified CNT sample (7 mm square) used in all following studies. (b.) Optical absorbance spectra of I_2 in ethanol at specified times after introducing a CNT sample into the cuvette. Inset shows photograph of 1 mM IBr in ethanol. (c.) Optical absorbance spectra of I_2 in hexanes at specified times after introducing a CNT sample into the cuvette. Inset shows photograph of 1 mM IBr in hexanes. (d.) Normalized absorbance intensity at peak

wavelengths over time for I_2 in ethanol and hexanes after solution preparation with and without CNTs present in the cuvette. (e.) Mass of I_2 dopant absorbed per mass of CNT sample during doping in ethanol and hexane solutions.

IBr was selected as a dopant due to its efficacy[97] and recent interest in interhalogen species.[99], [100] Purified CNT material (morphologically characterized by SEM in Figure S1) was exposed to a 0.2 g/L (1 mM) IBr doping solution in ethanol to determine the time dependency of doping using both iterative and single time exposure methods. The electrical conductivity results from both methods are compared in Figure 50a. In the case of the iterative method, a doubling in conductivity is observed after the first 10 min exposure, while the increase in conductivity thereafter is progressively less and approaches a maximum value around 60 min. In comparison, the single time exposure results for 30, 45, or 60 minutes coincide with the iterative method results, and a single exposure time of 90 min (yellow data point) shows minimal additional conductivity enhancement. Significant initial conductivity enhancement at short exposure times followed by a much lower rate of change after ~60 min is similar to results for $KAuBr_4$ (aq) doping of CNTs.[69]

The time dependence of IBr adsorption onto CNTs was measured using an optical absorption procedure for IBr solutions with CNTs present. Figure 50b shows the absorbance spectra for 0.2 g/L (1 mM) IBr in ethanol, and the suppression in the peak at 390 nm over time when CNTs are present. Figure 50c summarizes the 390 nm peak intensity over time with the CNTs present in solution (black diamond data points) compared to a control solution of 0.2 g/L (1 mM) IBr in ethanol without CNTs present (black circle data points). The IBr peak intensity of the control sample remains relatively constant over time (less than 1% change), whereas the IBr peak intensity of the sample containing CNTs decreases until approximately 60 min, after which point the rate of decrease is reduced. The amount of IBr adsorbed onto the CNT sample (normalized to the CNT sample mass) is calculated by Eq. 1 and shown as the blue square data points in Figure 50c. This data demonstrates rapid IBr adsorption that levels off at 60 minutes, which parallels the trend in conductivity enhancement observed in Figure 50a. The optical absorption data is used to determine the time-dependence of the interaction between the doping solution and the CNTs. The doping solution may contain species derivative of IBr such as I_2, Br_2, I^-, Br^-, I_3^-, etc., and the products of reactions between these species and the solvent due to the reactivity of interhalogen compounds and organic solvents.[108] The origin of the optical absorption peaks studied may be one of these derivatives or product compounds, but because the change in peak intensity is compared to a control sample without CNTs present, the computational result from Eq. 1 can be used as a metric for comparing the relative effects of CNT doping using different solvents and its time dependence. Thus, the results illustrate the strong correlation between time-dependent CNT conductivity enhancement and IBr adsorption.

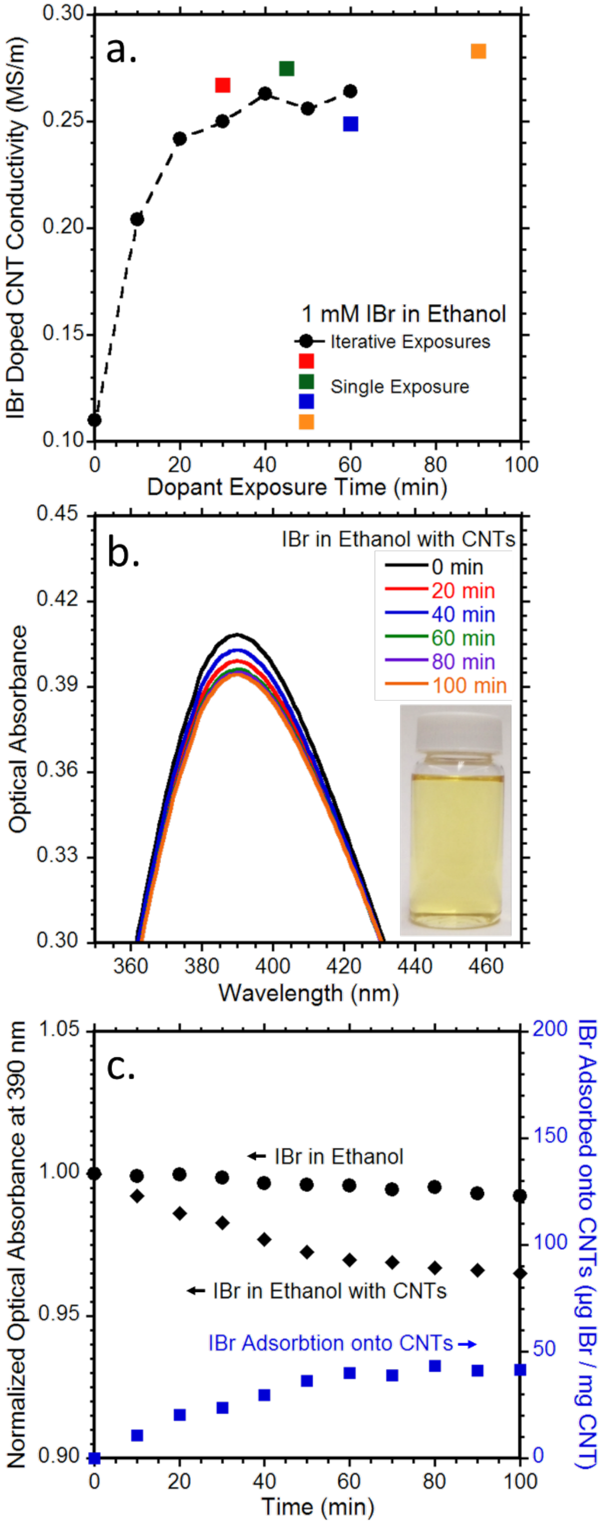
a.
IBr Doped CNT Conductivity (MS/m)
0.30
0.25
0.20
0.15
0.10
0
20
40
60
80
100
Dopant Exposure Time (min)
1 mM IBr in Ethanol
Iterative Exposures
Single Exposure
b.
IBr in Ethanol with CNTs
0 min
20 min
40 min
60 min
80 min
100 min
Optical Absorbance
0.45
0.42
0.39
0.36
0.33
0.30
360
380
400
420
440
460
Wavelength (nm)
c.
Normalized Optical Absorbance at 390 nm
1.05
1.00
0.95
0.90
IBr in Ethanol
IBr in Ethanol with CNTs
IBr Adsorbtion onto CNTs
200
150
100
50
0
IBr Adsorbed onto CNTs (µg IBr / mg CNT)
0
20
40
60
80
100
Time (min)

Figure 50. (a.) Time-dependent doping studies using 0.2 g/L (1 mM) IBr in ethanol. (b.) Optical absorbance of 0.2 g/L (1 mM) IBr in ethanol solution (data collected every 10 minutes but shown every 20 minutes for clarity) after introducing a CNT sample into the cuvette. Inset shows photograph of the 0.2 g/L (1 mM) IBr in ethanol solution. (c.) Optical absorbance values at 390 nm for a solution of 0.2 g/L (1 mM) IBr in ethanol both with (black diamond markers) and without (black circle markers) CNTs present in the cuvette over time. Optical absorbance data is normalized to absorbance at 0 min. Calculated values of the amount of IBr adsorbed onto the CNT sample are shown as blue square markers and plotted on the right y-axis over time.

Studies of IBr adsorption onto CNTs were repeated with hexanes as the dopant delivery solvent for comparison to IBr adsorption onto CNTs in ethanol to determine the effects of solvent polarity. Figure 51a shows the IBr in hexanes absorption peak at 503 nm and its decay over time when a CNT sample is present in the solution. Note that the peak absorption of IBr in hexanes occurs at a different wavelength than in ethanol (503 nm compared to 390 nm) and that the solution color differs as well (insets of Figure 50b and Figure 51a). This is due to the solvatochromic shift that halogen species exhibit in solution, which indicates differing interactions between the solvents and the IBr.[107], [109], [110] Figure 51b shows the IBr optical absorption peak intensity over time with (black diamond data points) and without (black circle data points) a CNT sample present. The amount of IBr adsorbed onto the CNT samples was calculated using Eq. 1, and the results are shown as the blue square data points on Figure 51b. For CNT samples doped with IBr in hexanes at 60 min, 129 µg IBr are adsorbed per 1 mg of CNT material present. By comparison, samples exposed to 0.2 g/L (1 mM) IBr in ethanol for 60 min yield adsorption of 40 µg IBr per 1 mg of CNT material. This implies a 3.2× increase in

IBr adsorption onto CNTs when delivered in hexanes compared to ethanol. As shown in Figure 50, the amount of IBr adsorbed onto the CNTs from an ethanol solution has been shown to correlate with the enhancement in electrical conductivity. Therefore, it is expected that the increase in IBr adsorption promoted by delivery in hexanes compared to ethanol will also lead to an increase in doped CNT electrical conductivity. Under identical doping conditions (0.2 g/L (1 mM) concentration, 60 min IBr exposure time, 5 mL IBr solution volume), doping CNT samples with IBr in ethanol yields an electrical conductivity of 0.25 MS/m, while CNT samples doped with IBr in hexanes had a conductivity of 0.35 MS/m, confirming that the greater IBr adsorption promoted by hexanes yields greater electrical conductivity enhancement.

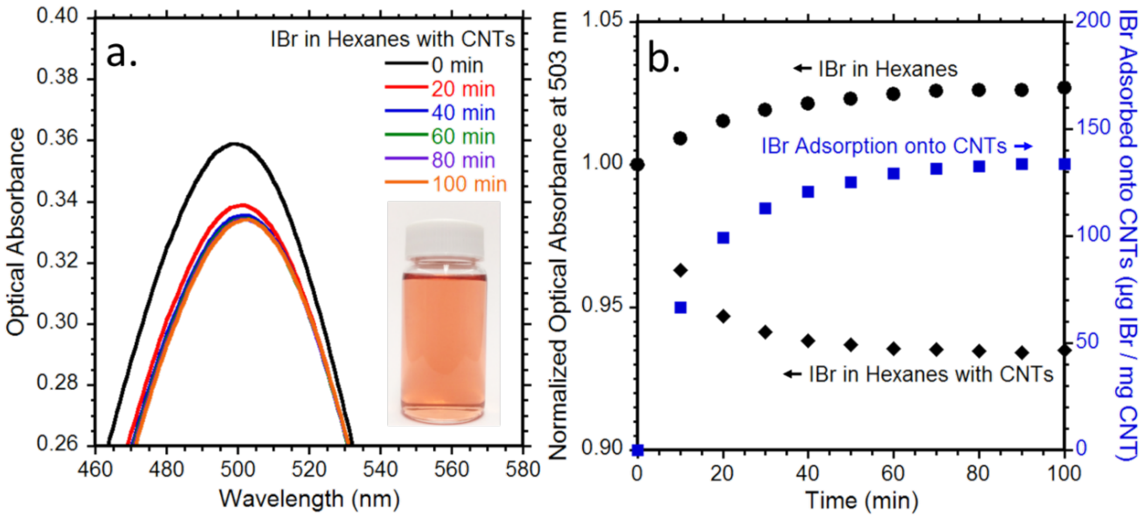

Figure 51. (a.) Optical absorbance of IBr in hexanes solution (data collected every 10 minutes but shown every 20 minutes for clarity) after introducing a CNT sample into the cuvette. Inset shows photograph of the 0.2 g/L (1 mM) IBr in hexanes solution. (b.) Optical absorbance values at 503 nm of an IBr solution in hexanes

both with (black diamond markers) and without (black circle markers) CNTs present in the cuvette over time. Optical absorbance data is normalized to absorbance at 0 min. Calculated values of the amount of IBr adsorbed onto the CNT sample are shown as blue square markers and plotted on the right y-axis over time.

While solution concentrations at this point have been 0.2 g/L (1 mM) for spectroscopy, electrical doping of CNTs typically takes place at 5-10 mM [97] and the observed effect with solvent polarity warranted a more systematic analysis of the solvent properties. At 2.1 g/L (10 mM), IBr is soluble in a variety of solvents that span the dipole moment range from ~0-4, which allows for the examination of dopant delivery solvent on CNT conductivity. CNT samples were exposed to 9 different solvents that span the range of typical solvent polarity from hexanes to dimethyl sulfoxide (DMSO) at a concentration of 2.1 g/L (10 mM) for 60 min and the results are shown in Figure 52a. In addition, IBr solutions were prepared in a DMA solvent, which is known to disperse CNTs effectively.[111] The electrical conductivity of the starting material is 0.10 MS/m, and the resulting CNT conductivity after exposure for 60 min in each doping solution shows differing enhancement by solvent type. In particular, CNTs exposed to IBr in DMSO exhibit the least improvement in conductivity, achieving only 0.18 MS/m. By comparison, doping CNTs with IBr in hexanes resulted in an electrical conductivity of 0.67 MS/m and IBr in water achieved 0.75 MS/m. There was no change in sample resistance when purified sheets were exposed to solvents without IBr present, the range of samples thicknesses were similar pre- (18 to 30 µm, median 21 µm) and post-dopant exposure (14 to 26 µm, median 20 µm), and no morphological changes were seen via SEM before and after solvent exposure (see Figure S1). While bulk CNT exposure to solvents has been demonstrated to influence CNT packing in the literature[32], [112-114], the lack of change in this study is likely due to prior solvent treatment to achieve high-density CNT structures by the manufacturer. Because the CNT starting material was the same for all IBr solutions studied, it was expected to contain similar degrees of surface functionalization so that the comparison between each doping solution's efficacy can be made. In general, a dependence on the solvent dipole moment is observed, where solvents with a lower dipole moment result in improved IBr adsorption on the CNTs and larger conductivity enhancement.

A proposed mechanism for the data in Figure 3a is explained by lower dipole moment solvents having weaker interactions with both the dopant and the CNTs, which shifts the equilibrium of dopant in solution to dopant adsorbed onto CNTs by favoring dopant-CNT interaction over dopant-solvent or CNT-solvent interactions. Therefore, when selecting a dopant delivery solvent, it is important to consider both the solvent's interactions with the dopant and with the CNTs. Weak interactions with both the solvent and CNTs are favorable for promoting high electrical conductivity. Further support for this mechanism includes DMA which has strong interactions with CNTs and the IBr dopant, and this dopant solution is observed to only minimally enhance CNT electrical conductivity. These results indicate that not all solvents in which a dopant is soluble will promote a large conductivity enhancement. Figure 52a also highlights that water as an IBr delivery solvent yields a high CNT electrical conductivity, and loosely follows the observed trend with dipole moment. The performance of water as an IBr delivery solvent fits the mechanism due to its weak interaction with IBr (low solubility) and weak interactions with CNT sheet materials, which are often hydrophobic.[115] The importance of dopant delivery mechanism for conductivity enhancement may in part explain why some species with large-magnitude redox potential are not always effective dopants.[97] Therefore, the dopant redox potential is a critical property for selection, but the data presented in this work implies that consideration for the dopant delivery methodology must also be made.

Since the results suggest an equilibrium dominated mechanism, increasing the concentration of dopant solution can drive the amount adsorbed for conductivity. Figure 52b shows the trend between the amount of IBr added to a solution of water or hexanes and the resulting CNT electrical conductivity after IBr exposure for 60 min. IBr reaches its maximum solubility at ~2.1 g/L in water and 12.4 g/L in hexanes, with additional IBr added to these solutions settling out as a solid. Raman spectra from purified CNT sheets and purified CNT sheets doped with 20.1 g/L IBr in hexanes are plotted in Figure S2, and show typical spectra of multi-walled CNTs with prominent, D-, G-, and G'-bands. [116], [117] The presence of a low frequency peak around 180-200 cm^{-1} in the doped sample spectra is attributed to the presence of some crystallized halogen species, which has been shown previously for $I_2(s)$.[118] Below the solubility limit in hexanes, increasing the IBr concentration correlates with an increase in doped CNT electrical conductivity. The samples doped in 12.4 g/L (60 mM) IBr in hexanes have the highest conductivity of 0.85 MS/m, 2.4x greater conductivity than samples doped in 0.2 g/L (1 mM) IBr in hexanes solutions. This conductivity of 0.85 MS/m from enhanced solvent delivery is a marked improvement over previously published results for IBr doped sheets which achieved 0.5

MS/m.[97] Above the solubility limit in both hexanes and water, the presence of undissolved IBr added to the doping solution does not significantly improve CNT conductivity enhancement beyond that of a saturated doping solution, indicating that doping with solutions at a saturated level provides the highest increase in conductivity. This explains how the conductivity enhancement at 2.1 g/L (10 mM) is greatest when using water as a solvent (Figure 52a), because water is fully saturated with IBr at this concentration. The trend between dopant concentration in solution and the resulting CNT electrical conductivity in Figure 52b is further evidence for an equilibrium-based mechanism, as increasing concentration yields an equilibrium shift toward an increased amount of IBr adsorbed onto CNTs and the presence of additional IBr yields no additional conductivity increase. These results motivate future studies with additional dopant systems of interest such as ICl, which can be used neat[100] or in a solvent[99].

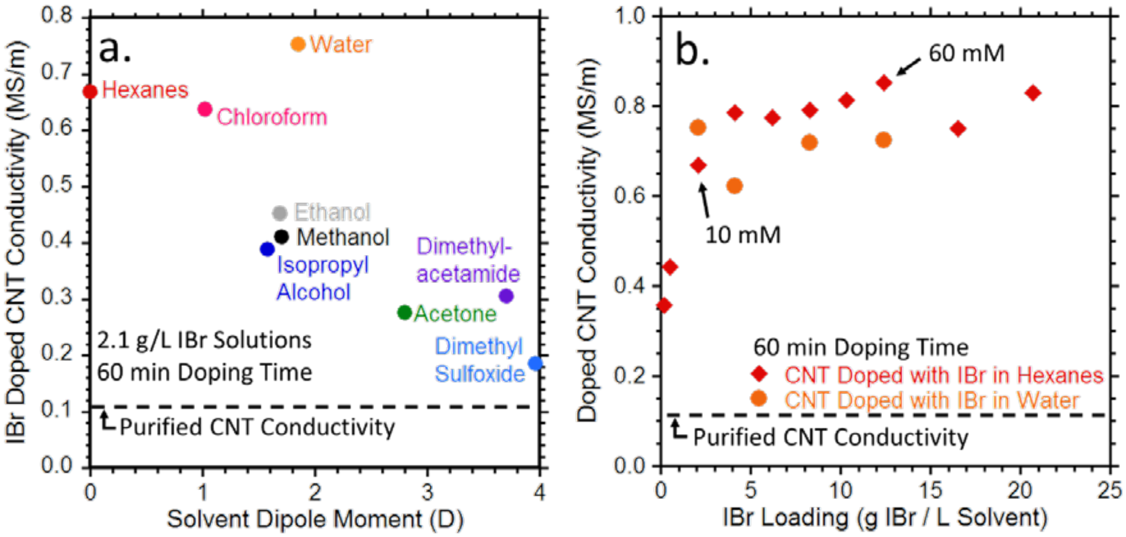

Figure 52. (a.) Conductivity of CNT samples after exposure to 2.1 g/L (10 mM) IBr for 60 min in the specified solvent versus that solvent's dipole moment. [119] (b.)

Conductivity of CNT samples doped with various solution loadings of IBr in hexanes for 60 min.

The efficacy of IBr doping in high-current applications was tested on similar CNT material in a conductive yarn format. The as-received yarn was exposed to a saturated (20.7 g/L) solution of IBr in hexanes for one hour, which did not influence the wire dimensions, as shown by optical microscopy in Figure S4. The conductivity of the as-received yarn (0.1 MS/m) increased 13.4× to 1.4 MS/m, using a cross section determined by SEM (see Figure S3). Stress-strain characteristics of the as-received yarn and doped yarn are presented in Figure 53a and demonstrate that IBr dopant exposure in hexanes does not decrease the tensile strength of CNT yarns. High-current testing of the as-received yarn and doped yarn was performed and the results of this testing are presented in Figure 53b. The maximum current sustained in a CNT yarn doped with IBr in hexanes (490 mA) is increased by 36% over the maximum current withstood an as-received yarn (360 mA) to a current density of 26.6 MA/m^2., demonstrating that proper dopant delivery can enhance the current density at failure of CNT yarns and wires without compromising their mechanical integrity.

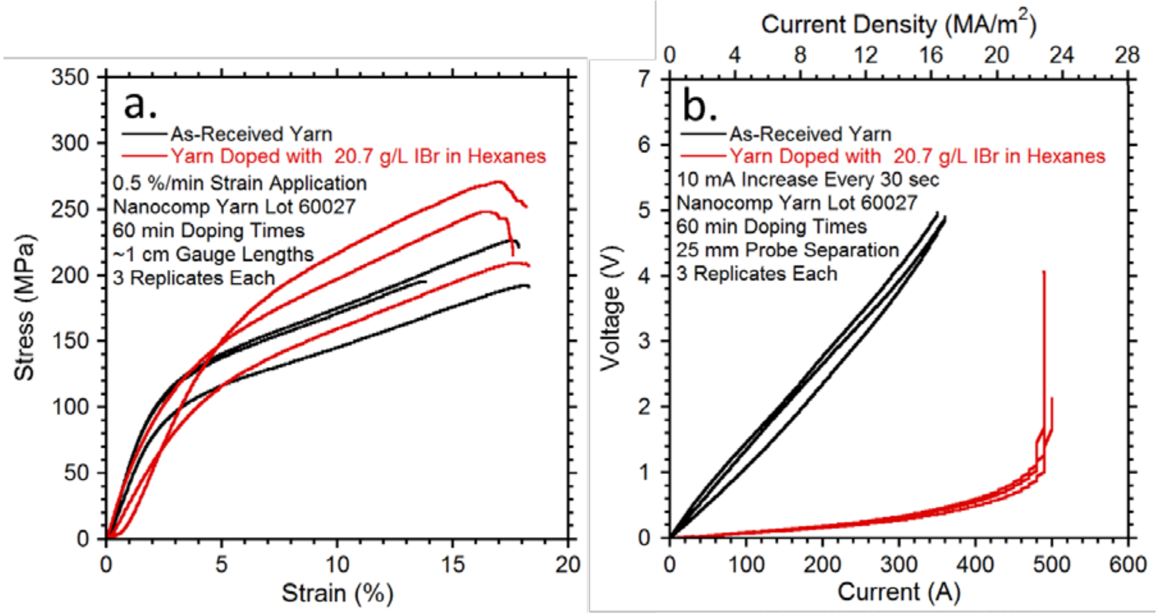

Figure 53. (a.) Stress-strain characteristics of CNT yarns with and without IBr solution doping. (b.) Current-voltage characteristics of CNT yarns with and without IBr solution doping.

It is important to note that the power at failure is reduced in the sample exposed to IBr in hexanes when compared to the as-received yarn sample. This is possibly due to changes in thermal conductivity that arise from the presence of dopants. Chemisorbed species on CNTs as well as substitutional dopants have been shown to lower CNT thermal conductivity [120], [121], while surface-adsorbed oxygen has been shown to either increase [122] thermal conductivity or have little effect [123] on it. If adsorbed halogen species lower the thermal conductivity of CNT yarns, the temperature of a doped yarn under high current could be higher than an as-received yarn for a given applied power. Thus the failure temperature for the wire could be reached with lower applied powers.

6.5 Additional Considerations for the Study of IBr Doping

The highly volatile and reactive nature of IBr created several challenges. Reactions with some of the solvents, solvatochromic shift, and the multiple forms of the dissolved IBr species (IBr, Br^-, Br_2, I_2, I^-, I_3, etc.) [106], [108] make optical absorption peak assignment difficult. As an example, I_2 and Br_2 were dissolved separately in chloroform as a solvent and their optical absorption spectra were recorded in Figure 54. The Br_2 solution (red curve) has a peak at 270 nm and a broader, less intense peak at 400 nm, while the I_2 solution (blue curve) has a single peak at 510 nm and some absorption below 250 nm. When these two solutions were combined in equal volumes, the resulting solution (black curve) had a much more intense peak in absorption at 270 nm, and the absorbance peak at 510 nm was blue-shifted to 500 nm and also decreased in intensity, indicating complex interactions between the two species when simultaneously in solution. When compared to an equal-concentration solution of IBr (green curve), similarly strong absorbance is noted at 270 nm, and the peak at 500 nm is of increased intensity. This study highlights the difficulty in assigning optical absorption peaks for solutions of IBr in different solvents to specific dissolved species, leading to the use of time-dependent optical absorption spectroscopy in previous IBr studies as a relative and qualitative technique.

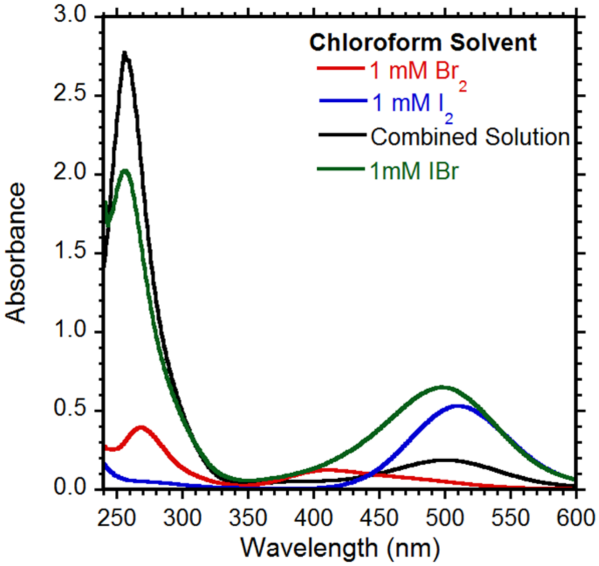

Figure 54. Optical absorption spectra of a 1 mM solution of Br_2 in chloroform (red), a 1 mM solution of I_2 in chloroform (blue), a mixture of the two previous solutions mixed in equal volumes (black) and a 1 mM solution of IBr in chloroform.

Additionally, the optical absorption spectrum of IBr in hexanes presents two peaks, one at 279 nm, and one at 503 nm. When using either peak in the spectrum, both give qualitatively similar results are obtained, as seen in Figure 55. Computing the IBr adsorption onto CNTs by assuming either peak is indicative of total IBr adsorption using equation (7) at 60 minutes yields 115 µg IBr/mg CNT when using the peak at 297 nm, and 129 µg IBr/mg CNT when using the peak at 503 nm. These two values are similar and show the same relative difference from IBr adsorption when compared to ethanol.

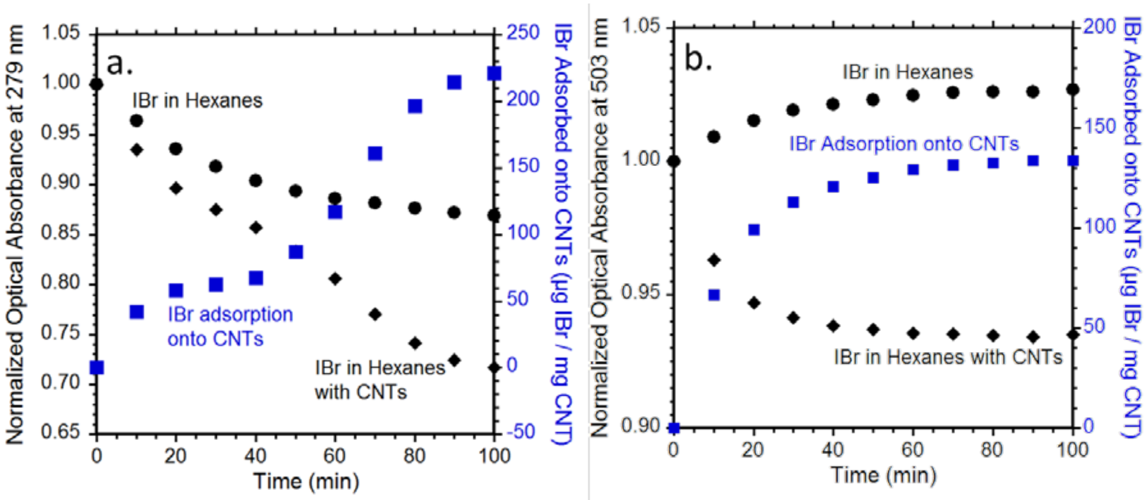

Figure 55. a. Optical absorbance (left axis) at 279 nm of a solution of IBr in hexanes (black circle datapoints) as a function of time after mixing the solution, and of a solution of IBr in hexanes with CNTs as a function of time after solution mixture and CNT addition (black diamond data points). The amount of IBr adsorbed onto the CNTs (blue square data points, right axis) calculated from the optical absorption data in this plot and equation (7). b. Optical absorbance (left axis) at 503 nm of a solution of IBr in hexanes (black circle datapoints) as a function of time after mixing the solution, and of a solution of IBr in hexanes with CNTs as a function of time after solution mixture and CNT addition (black diamond data points). The amount of IBr adsorbed onto the CNTs (blue square data points, right axis) calculated from the optical absorption data in this plot and equation (7).

Optical spectra was taken of solutions of IBr in solvents other than hexanes and ethanol as well. Figure 56a shows optical absorption spectra of a 1 mM IBr solution in chloroform with CNTs present, and two distinct peaks are visible at 256 and 503 nm. This data, along with a control study performed using a 1 mM IBr solution in chloroform without CNTs present was analyzed for use in IBr absorption calculations. The peak intensities at 256 and 503 nm are plotted for both the samples with and without CNTs in Figure 56b. The drastic difference in relative absorption change at the two peak values presented in this plot make the chloroform solvent a difficult system to determine IBr adsorption onto and was not used for further study. Similarly, Figure 56c shows optical absorption spectra of 1 mM IBr solution with CNTs present. The peak intensity is seen in increase over time, which does not fit the model of dopant absorption used in this work. In Figure 56d, it can be seen the peak intensity increased regardless of the presence of CNTs in the cuvette, and is likely due to reactions between DMSO and IBr taking place over time (strong interactions as described in section 6.6). This fact, and the lack of a distinct peak presence in the IBr in DMSO optical spectrum make this system non-ideal for dopant absorption study.

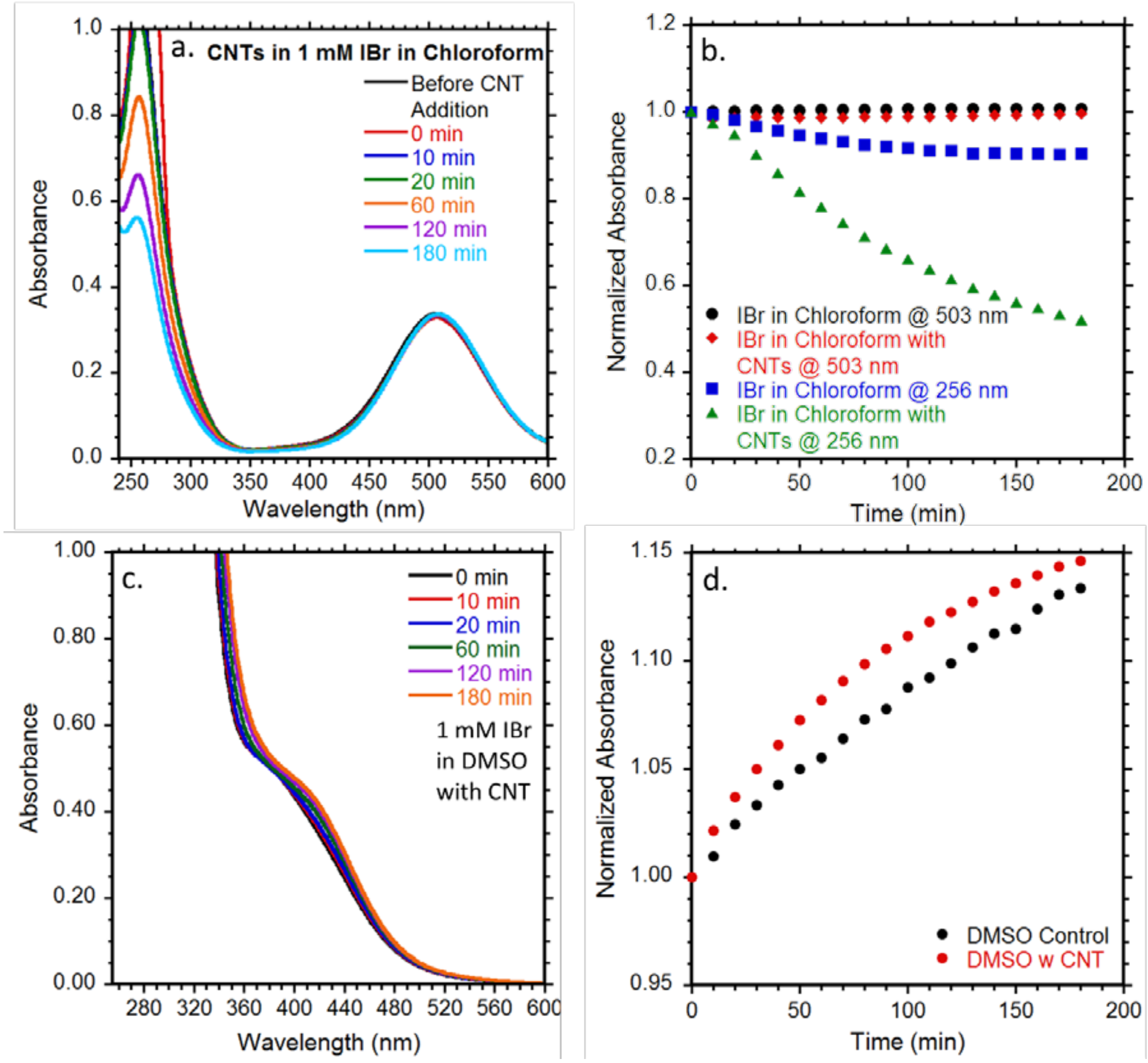

Figure 56. a. optical absorption spectra of 1 mM IBr solution in chloriform with CNTs present in the cuvette at several times after mixing. b. optical absorbance intensity at 503 and 256 nm, with and without CNTs in present in the cuvette as a function of time after mixing or mixing and CNT addition, normalized to the optical absorbance intensity at 0 min. c. optical absorption spectra of 1 mM IBr solution in DMSO with CNTs present in the cuvette at several times after mixing. d. Optical absorbance intensity at 414 nm of 1 mM IBr solutions with and without CNTs present in the cuvette as a function of time after mixing or mixing and CNT addition, normalized to the optical absorbance intensity at 0 min.

6.6 IBr Doping Conclusions

The time dependency of IBr doping was measured via electrical and optical absorbance techniques in ethanol, which demonstrated a correlation between conductivity enhancement and dopant adsorption, and established a timescale for subsequent doping studies. Dopant adsorption and electrical conductivity enhancement from IBr in hexanes and ethanol were compared, and the hexanes dopant delivery solvent promoted 40% higher doped CNT conductivity and 3.2× greater dopant adsorption, indicating that solvent selection is an important factor in solution-based CNT doping. A systematic survey of IBr delivery solvent polarity was conducted, and the data supports a proposed mechanism whereby solvent properties strongly influence the dopant-solvent and CNT-solvent interactions, which mediate the strength of the preferred dopant-CNT interaction. Thus, water and low dipole moment solvents such as hexanes have been determined as optimal dopant delivery solvents for enhancing the electrical conductivity of CNT materials using IBr. The concentration dependency of doping in hexanes and water was determined, with samples doped in 12.4 g/L (60 mM) IBr in hexanes have the highest conductivity of 0.85 MS/m, and finding that doping with solutions at a saturated level provides the highest increase in conductivity. Applying these doping conditions (20.7 g/L (100mM) IBr in hexanes for one hour) to commercially available CNT yarns resulted in a 13.4× increase in conductivity and a 36% increase in current density at failure of these yarns. The results in this work demonstrate the importance of solvent selection, doping time, and concentration to doping of CNTs in sheet and yarn format when enhancing conductivity toward practical wires for electrical and high current applications.

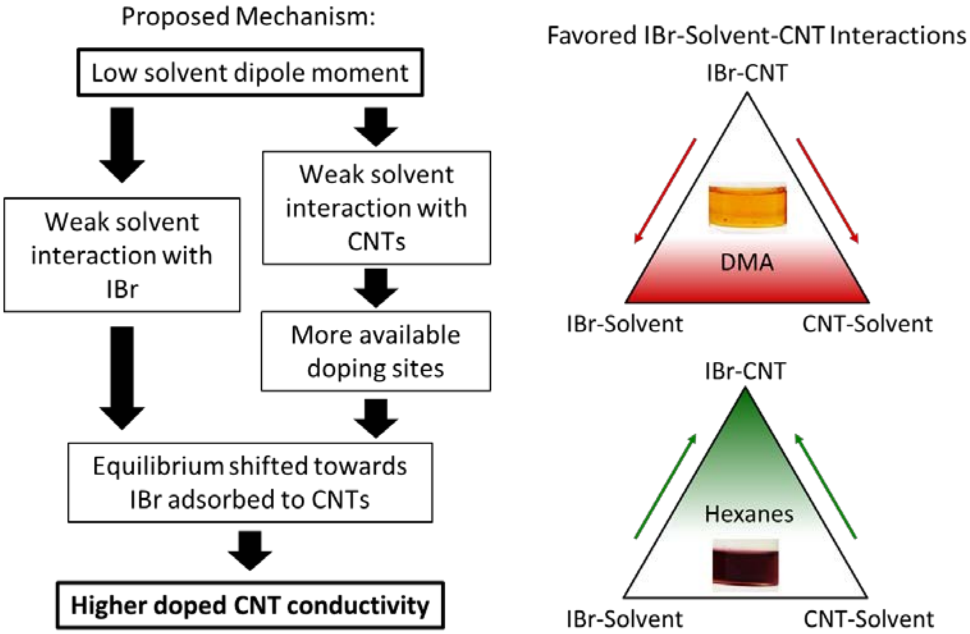

Figure 57. (left) Flow diagram of how dipole moment governs the interactions between the solvent and IBr, and the solvent and the CNTs, and how these combined interactions affect doped CNT conductivity. (right) pictoral representations of the favored interactions in the IBr-solvent-CNT system for a solvent that promoted low CNT conductivity enhancement (DMA) and a solvent which promoted high CNT conductivty (hexanes). The favored interactions are those that the arrows point to.

Chapter 7. Influence of Purification and Doping in Radial Densification of CNT Sheet Material

Tasks:

- Determine and evaluate methods for obtaining phase-pure commercially sourced CNT sheet material.
- Analyze the effect of purity on the electrical and mechanical properties of commercial CNTs.
- Apply planar or radial densification and purification techniques to commercial CNT sheet materials and optimize both properties for high strength and conductivity.
- Hybridize commercial CNT materials with metals or other nanomaterials through mechanical inclusion or chemical deposition to improve electrical, mechanical, and thermal properties.

7.1 Purification of Commercially Sourced CNT Sheet Material

NRPL has worked closely with Nanocomp Technologies Inc. (NCTI) on improving and applying their CNT materials, including both yarns and sheet materials. NCTI CNT sheets are produced in industrial quantities using a floating catalyst CVD synthesis method. The resulting product contains carbonaceous and metallic impurities from synthesis as evidenced in SEM and TGA data in Figure 58 (a) and (b) respectively.

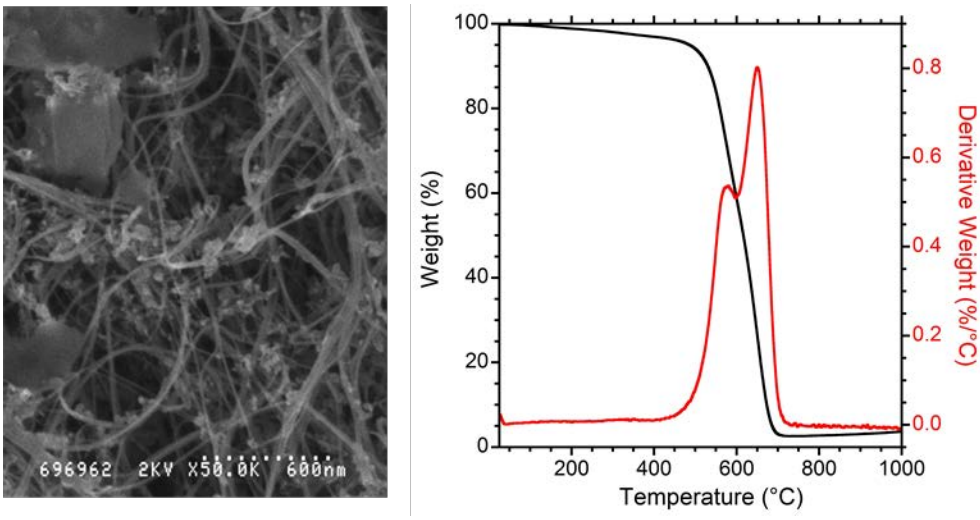

Figure 58. (a) SEM of AR NCTI CNT sheet material. (b) TGA data from oxidizing AR NCTI sheet material

Past purification techniques have utilized a thermal oxidation to remove amorphous carbons which oxidize into gaseous compounds at lower temperatures than NCTI MWCNTs. This oxidation exposes residual Fe catalyst particles that remain from synthesis. Soaking the NCTI material in HCl after oxidation solubilizes the exposed Fe as indicated by a color change in the HCl from clear to yellow. This color change does not occur when non-oxidized NCTI material is soaked in HCl, indicating that residual Fe is encapsulated in non-HCl-soluble carbon. Typically, an HCl soak is followed by a second thermal oxidation at an identical temperature to the first in order to vaporize HCl which has adsorbed onto the NCTI CNTs. The temperature of the initial oxidations limited by the formation of hot-spots, which occur due to the exothermic oxidation of Fe. It may be possible to improve purity further by increasing the temperature of the second thermal oxidation due to the reduced Fe content in a sample. The initial thermal oxidation should be optimized for maximal Fe removal, and the second oxidation optimized to remove non-MWCNT carbons. It is not clear how increased purity affects the mechanical and electrical properties of these materials.

7.2 Influence of Purity on Electrical and Mechanical Properties

Carbonaceous impurities in NCTI samples are not as conductive as the MWCNTs themselves. However, purification by thermal oxidation and HCl soaking does not drastically alter the morphology of the MWCNT network. Removing the impurities leaves microscale voids in a sample. As such, purified samples tend to have lower tensile strengths and conductivities after purification than they did prior to purification. However, purification allows chemical doping of NCTI samples to be more effective, and allows for modification of the network morphology. Thus, doping and morphology modification techniques, such as mechanical densification, is further studied in conjunction with high purity NCTI samples.

7.3 Radial Densification of Carbon Nanotube Wires

CNT wires can be fabricated from commercial sheet materials through radial densification through standard steel, tungsten carbide, or diamond drawing dies [54], [124]. Wire drawing requires that the sheet materials possess sufficient mechanical strength to withstand the frictional force generated by the drawing die. For instance, sheets provided by NCTI have been drawn into wires while those from NanoTech Labs (NTL) frequently broke during drawing and did not lead to coherent wires. While radial densification leads to cylindrical-form conductors, it is unclear if this process improves the electrical or mechanical characteristics of a wire as compared to the conductivity of its constituent sheet materials which are already highly dense. Purified NCTI materials contain a higher fraction of highly conductive MWCNTs, yet also contain voids remnant from the removal of Fe and non-MWCNT carbons from the AR material. Thus, radial densification in combination with purification may yield higher conductivities and tensile strengths than measured in AR NCTI material. Tensile testing data on densified wires made from NCTI material, AR or purified, has not been published. Electrical data from densified wires made from purified NCTI material has not been published.

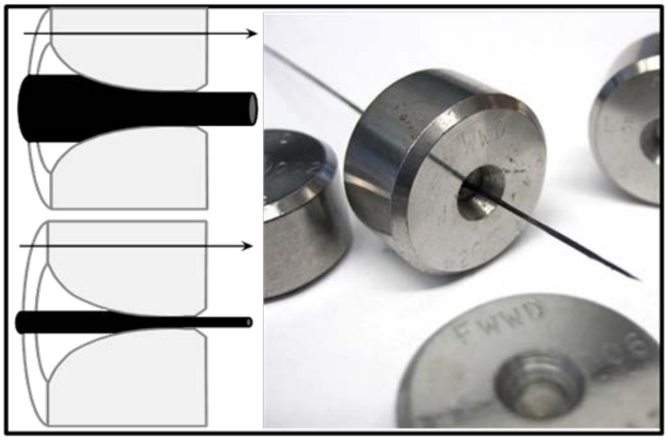

Figure 59. (left) Cross section schematic of the radial densification of CNT wires. (right) Photo of a CNT wire being densified. [98]

Preliminary experimentation on densified wires to determine the impact of thermal treatments in conjunction with doping. Thermal treatments included a 30 min, 900 °C anneal in 95 % Ar, 5 % H_2, and a purification process that consists of a thermal oxidation under flowing air at 520 °C followed by a 30 min soak in concentrated HCl and a subsequent 520 °C thermal oxidation under flowing air. Samples that were both annealed and purified were done so in two manners: purification preceding annealing, and purification subsequent to annealing. The CNT sheet material used in this study was from NCTI Lot 71244 which are ribbons of acetone-densified sheet material, 0.75 inch wide by 7 ft long. All samples were rolled and densified through drawing dies of decreasing diameter with a final die diameter of 0.7 mm. Samples were doped in either $KAuBr_4$ (aq) or IBr (dissolved in hexanes) for 30 min, or left untreated as controls. All thermal treatments were conducted prior to densification, and doping was conducted after densification.

Nine replicate samples were produced with each of the five treatments: no treatment (denoted “As-Received”), purified, annealed, purified then annealed (denoted Purified/Annealed), and annealed then purified (denoted Annealed/Purified). Three of each type were doped with each dopant or left as controls. The tensile results from this study are presented in Figure 60. From the raw, non-normalized data (Figure 60a) it can be observed that purified samples, regardless of annealing and doping, have lower tensile strengths than non-purified samples. Since all samples were densified to the same diameter and started with the same width of material, the tensile strength in N is indicative of the cross-sectional area normalized tensile strength in MPa. This is corroborated by diameter measurements via caliper. When mass-normalizing the data and observing the specific tensile strength (Figure 60b), it is apparent that $KAuBr_4$ doping increases the mass per length of a sample without increasing its tensile strength. The same effect is not observed for IBr doping. Most samples have similar specific tensile strengths, indicating the mass lost during purification makes up for the reduced tensile strength in this metric.

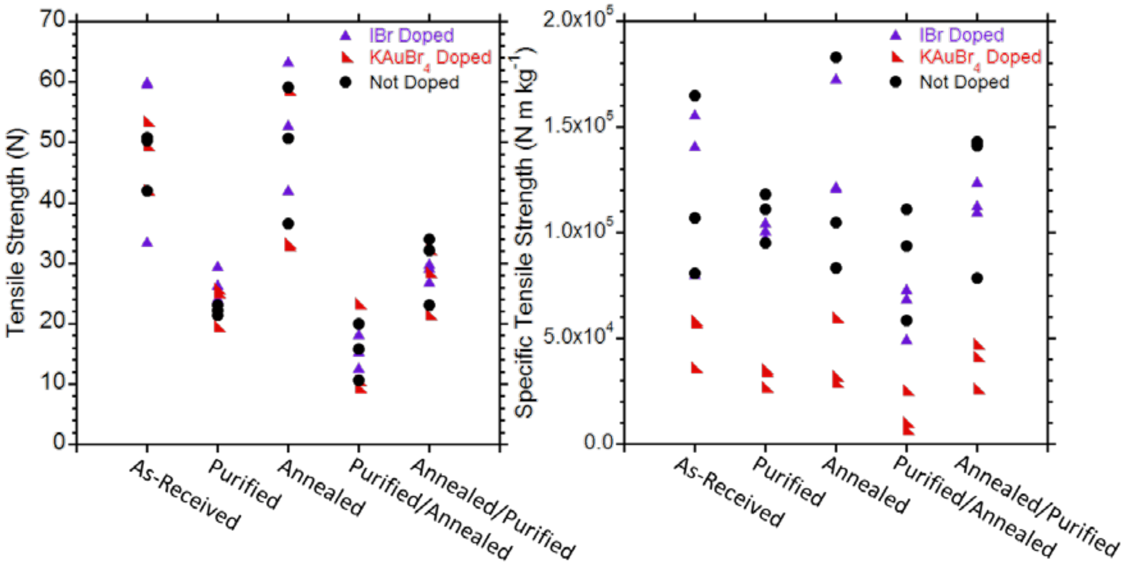

Figure 60. (a) tensile and (b) mass-normalized tensile properties of densified NCTI CNT wires made from materials with varying treatments and doped with either $KAuBr_4$ in water or IBr in hexanes.

Electrical results from this study are displayed as inverse resistance per length (Figure 61a) which is a measure of conductivity without area normalization. Area normalization is not necessary for comparison between samples in this study because all samples have similar cross-sectional area. This data demonstrates that doped samples, regardless of thermal treatment, have higher conductivity than samples that were not doped. It also shows that similar conductivities are obtained from all samples with the same doping, i.e. thermal treatments such as purification do not substantially alter the conductance of a sample. The specific conductivity of these samples (Figure 61b) is significantly improved by IBr doping, but not by $KAuBr_4$ doping. This is because of the increased mass per length of $KAuBr_4$ doped samples decreases their specific conductivity despite the conductance increase due to doping.

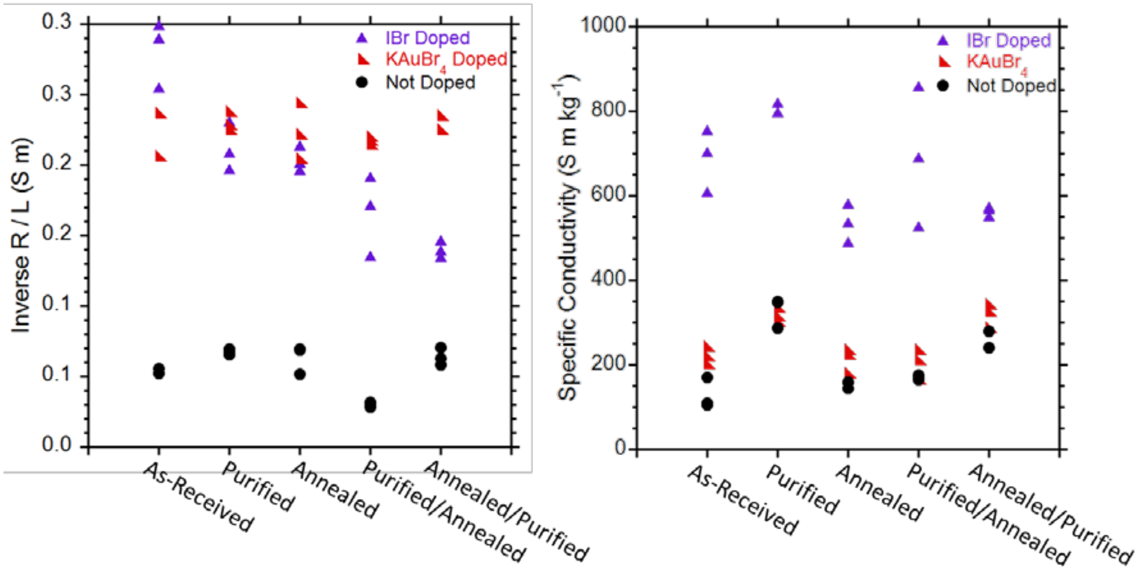

Figure 61. (a) L/R and (b) specific conductivity of densified NCTI CNT wires made from materials with varying treatments and doped with either KAuBr$_4$ in water or IBr in hexanes.

The thermally treated ribbons used in this study were characterized by Raman spectroscopy prior to densification to determine relative defect levels. Figure 62a shows representative Raman spectra of each treatment type with their intensities normalized to the G-peak max of the as-received sample. The D/G and D/G’ ratios are extracted from these spectra and shown in Figure 62b. The purified sample has the largest set of ratios likely due to defects created during oxidation. The annealed samples have lower ratios which may be attributed to defect healing at high temperatures or oxidation reduction due to the presence of H_2. The anneal especially helps to reduce the D/G and D/G’ ratios after purification where some of the defects created during purification are healed and reduced. Annealing prior to densification also helps reduce the final ratios. This may be due to a reduction in defects which would have otherwise been exacerbated through oxidation during purification.

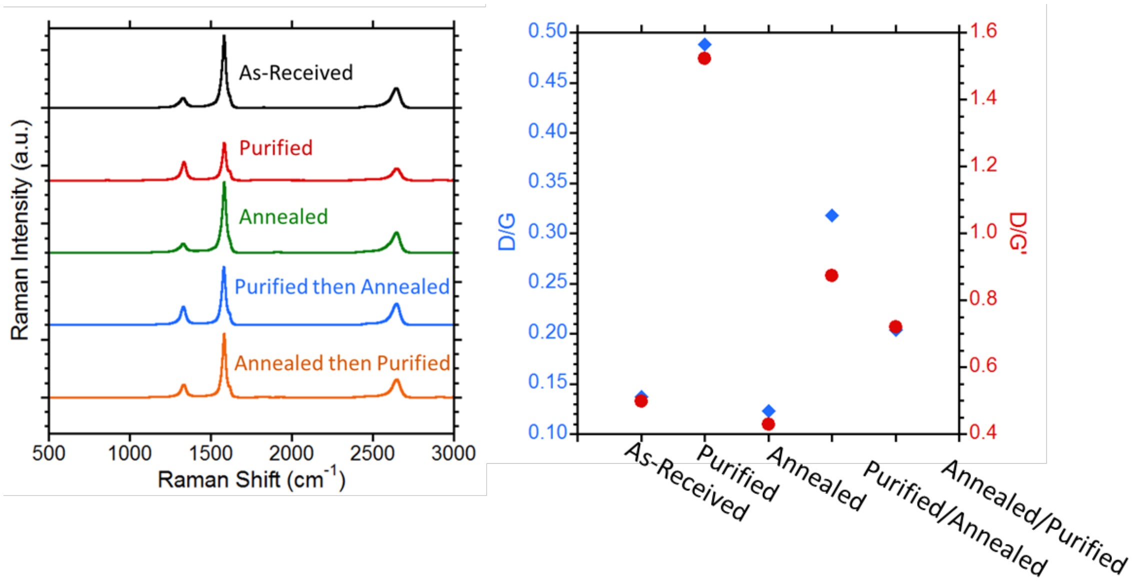

Figure 62. (a) Raman spectra of NCTI materials used to create the samples Figure 60 and Figure 61. (b) D/G and D/G' ratios calculated from the spectra in (a).

Radial densification in concert with purification may improve conductivity by eliminating carbonaceous and iron impurities that are less conductive than CNTs and removing the void space created by their elimination. The density of CNTs in sheet format cannot be improved much by mechanical densification due to mechanical pressing and solvent densification during their manufacture, so densification without purification cannot achieve a large degree of conductivity improvement. Likewise, purification without densification leaves behind a CNT network with voids that are less conductive than the impurities that were filling them, so conductivity is not increased. Figure 63 demonstrates conductivity and density improvement due to combined purification and densification. Purification in this study consisted of a thermal oxidation under flowing air to the temperature specified, flowed by a concentrated HCl rinse, and subsequent thermal oxidation at the same conditions as the initial oxidation.

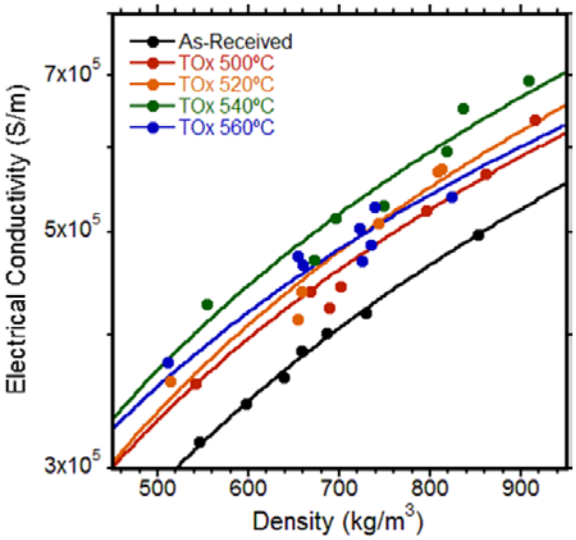

Figure 63. Electrical conductivities of densified CNT wires which have been densified to various densities and thermally oxidized at different temperatures.

Chapter 8. Dissertation Conclusions and Impact

Wires were formed from laser-vaporized SWCNTs by dispersing them in CSA and extruding the dispersion into a coagulant bath (Chapter 3). Established purification methods were employed to increase the purity of SWCNTs in dispersion, which led to a 4x improvement in extruded wire conductivity over as-produced SWCNT material. Coagulant selection was investigated using both one-factor-at-a-time and designed experiments approaches, and pure acetone was selected as the optimal solvent due to its low viscosity, which facilitates removal of acid dispersant, and high volatility, which ensures complete coagulant removal from the wire post-coagulation. Conductivity enhancements in extruded wires were developed by inducing tension on the SWCNT-CSA dispersion as it coagulated by increasing the depth of the coagulant vessel. This in-situ tensioning combined with additional tensioning applied to the wires post-extrusion led to a 2x improvement in specific conductivity over wires extruded into shallower baths without post-extrusion tensioning, due to the greater CNT alignment induced from tensioning. Overall, combination of the optimized coagulation parameters has yielded acid-doped wires with electrical conductivities of 4.1-5.0 MS/m and tensile strengths of 210-250 MPa. These conductivities are the highest reported electrical conductivities for extruded wires without additional doping reported to date, and they exceed the conductivities of any other CNT type extruded (Section 4.2).

Additional improvements to the extrusion process were developed from investigation of the coagulant bath temperature and syringe needle geometry (Section 4.3). Larger diameter syringe needles promoted higher extruded wire specific conductivity, as did colder acetone coagulant baths and increased rates of coagulant flow through coaxial syringe needles. Wires extruded from a 61 mg/mL SWCNT in CSA dispersion through a 22 Ga syringe needle into a -10 °C, 66 cm deep acetone coagulant bath had uniformly high conductivities of 5.1 MS/m. These results highlight the importance of the coagulation dynamics in the extrusion process as a major determining factor of wire uniformity and alignment, and thus electrical performance. An automated extrusion apparatus was built that extruded wires with variability in conductivity as low as 6 % (Section 4.5). This modular apparatus was designed and built to easily tailor additional extrusion factors identified to have significant influence on resulting wire properties. Process scale-up and automation, including post processing tensioning and treatment, can be achieved with this device.

Both commercial CNT yarns and extruded SWCNT wires were characterized at high applied currents (Chapter 5). By comparing current-controlled and voltage-controlled testing scenarios and drawing analogies from them to mechanical testing, voltage-controlled testing was determined to be the fitting method of characterizing CNT wires at high currents to avoid rapid voltage increases, which occur during current-controlled testing and do not allow for thermal equilibration of the wire with its surroundings or assessment of progressive wire failure. This comparison and its outcomes are useful to the CNT wire community as it informs testing standards for these materials when subjected to electrical testing. The high current failure of CNT yarns and extruded SWCNT wires was found to be dependent on the ambient gas present, with enhancements in maximum current in nitrogen due to the lack of oxygen present, and further enhancement in helium due to the lack of oxygen and the higher thermal conductivity of helium compared to air and nitrogen. Extruded SWCNT wires failed at current densities of 180 MA/m^2 in air, 11.5x greater than those of CNT yarns in air. Maximum current densities of 420 MA/m^2 for extruded wires were reached in helium. SEM and Raman spectroscopy failure analysis of CNT yarns and SWCNT wires demonstrated that the lack of impurities in SWCNT wires was an enabling factor in the enhancement of their maximum current over CNT yarns.

Finally, IBr was selected as a CNT chemical dopant for study on purified CNT sheets based on its electrochemical potential, optical properties, and recent interest in interhalogen doping compounds (Chapter 6). The time-dependence of electrical enhancement in the conductivity of CNT sheets was determined and compared to the time-dependent dopant adsorption onto CNT sheets using optical absorption spectroscopy. A correlation was found between dopant adsorption amount and electrical conductivity enhancement. Dopant adsorption and electrical conductivity enhancement from IBr in hexanes and ethanol were compared, and the hexanes dopant delivery solvent promoted 40% higher doped CNT conductivity and 3.2× greater dopant adsorption, indicating that solvent selection is an important factor in solution-based CNT doping. A study of IBr solvents for dopant delivery to CNT sheets determined that IBr low-polarity solvents promoted higher conductivity enhancement in CNT sheets exposed to them than did IBr in high-polarity solvents. Thus, water and low dipole moment solvents such as hexanes have been determined as optimal dopant delivery solvents for enhancing the electrical conductivity of CNT materials using IBr. The concentration dependency of doping in hexanes and water was determined, with samples doped in saturated solutions of IBr in hexanes having the highest conductivity of 0.85 MS/m, compared to the purified CNT sheet conductivity of 0.11 MS/m. Applying these doping conditions to CNT yarns resulted in a 13.4x increase in conductivity and a 36% increase in current density at failure.

This dissertation research demonstrates the importance of SWCNT purity and selection of coagulation conditions in promoting high-density, aligned SWCNT wires. Delivery of chemical dopants with high electrochemical potential through solvents which favor dopant-CNT interactions also enhances electrical conductivity and maximum current density, achieving CNT wires capable of competing with metal conductors for electrical transmission applications. The testing methodologies developed for both voltage-controlled high-current characterization and determination of ideal dopant delivery can be adapted for other CNT conductors and dopants of interest, respectively. This work has also provided the highest conductivity extruded CNT wires to date and an extrusion apparatus that can scale up their production and decrease their variability. This work contributes to the understanding of the factors impacting SWCNT dispersion coagulation in wire fabrication, high-current wire behavior, and chemical doping and will allow for design and engineering of CNT wires, which may replace metal conductors for power and data cable applications.

Appendix A: Dissertation Contribution Acknowledgments

- Section 1.1 – Graphene rendering in Figure 1 was provided by Andrew Merrill.
- Section 3.3.2 – Experimental design was determined in collaboration with Dr. Robert Parody, who also contributed Figure 13.
- Section 4.2.1 – DWCNT purification and SEM images in Figure 21a and b were conducted by Michael Hladky under instruction of the author.
- Section 4.2.2 – Figure 22a was provided by Brian Landi and Figure 22b was originally created by Paul Jarosz and edited by the author.
- Section 4.2.2 – Synthesis and purification of SWCNTs synthesized under nitrogen was conducted by Michael Hladky under the instruction of the author. SEM, Raman, and TGA data in Figure 23 were recorded by Michael Hladky.
- Figure 25 - SEMs were taken by Ivan Puchades.
- Figure 30 - Anthony Leggiero and Dylan McIntyre contributed to the fabrication and characterization of this sample set while analysis was performed by the author.
- Figure 35 – Heather Ursino and Martin Dann assisted the author with construction of the extrusion apparatus.
- Figure 50a and Figure 52a use data acquired by Quintina Frink and analyzed by the author.
- Figure 53 data was acquired by the author with the help of Karen Soule.

Appendix B: Wire Extrusion Standard Operating Procedure

I) Dispersion Preparation
   1) Have all CNT materials ready for dispersion (purified, dried, etc.).
   2) Mass a scintillation vial with a labeled, PTFE-lined cap on it, and record the mass. PTFE caps have a BROWN liner inside. Failure to use a PTFE will result a ruptured cap and loss of the dispersion.
   3) In the hood or acid glove box, pour CSA into scintillation vial. 2mL is a minimum so that dispersion can be scooped into the syringe for extrusion. If a specific quantity is desired, dispense the amount of water into the scintillation vial, mark the water level, and then empty and dry it before adding CSA to that mark. It is not recommended to dispense CSA using a glass pipette and bulb because the painted on graduations will decay in CSA vapor.
   4) **Be sure to wipe down the threads of both the scintillation vial and the csa container before replacing their caps**. Failure to do so will cause the sides of the cap to degrade and fail over time.
   5) Mass the vial with CSA and cap and record the mass. Calculate the exact volume of CSA by subtracting the vial & cap mass from this mass. The density of CSA is 1.753 g/mL.
   6) In a separate scintillation vial, mass out the exact amount of CNTs needed to achieve the desired weight loading. Standard weight loading for purified NPRL SWCNTs is 45 mg/mL.
   7) In the hood or acid glove box, add the CNTs into the vial containing CSA. **Be sure to wipe down the treads of the scintillation vial before replacing the PTFE cap.**
   8) Record the mass the vial with CSA, cap, and CNTs. Subtract the mass of the vial, cap, and CSA to determine the amount of CNTs added and calculate the % by mass CNT, and the mg CNT per mL CSA.
   9) Ensure the dispersion cap is on tightly, and wrap it in parafilm.
   10) Load the dispersion into the Thinky AR-100 and mix for 20 min. Make sure to set the counterweight in the Thinky to the mass of the vial plus the Thinky adapter.
   11) After Thinky mixing is complete, place the dispersion vial into the LabRAM vial holder. Make sure all the other vial slots are filled with empty vials (with PTFE caps) except for the center slot. Screw the top clamp down. If any of the blank vials are loose, unscrew its cap until tight. Set the timer on the LabRAM for 1-2 hrs. Mix at 30-50% intensity or higher.
   12) Repeat steps 10 and 11 until 4 or more rounds have occurred. Complete mixing with one or more additional 20 minute runs in the Thinky.

II) Assemble the following materials prior to extrusion:
   1) Dispersion - Dispersions are typically mixed for one 20 minute round in the Thinky immediately prior to extrusion.

2) Glass Slides - Extruded samples for characterization are mounted to 7.5 cm glass slides with double-stick tape on both ends. When preparing these slides, ensure that the tape is place precisely so that the spacing between the tape edges is exactly 5 cm.
3) Glass Syringe – Use the smallest glass syringe from Cadence that will fit the dispersion needed. Typically 2 mL syringes are used.
4) Syringe Needle – select a gauge, attach one needle to the syringe and have additional ready in case a needle change is needed.
5) Coagulant vessel – either a deep test tube or horizontal bath is needed.
6) Coagulant – select a coagulant (typically acetone) and chill or heat it to the desired temperature using ice baths, the refrigerator, or a hot plate. Remember to label all containers.
7) Pump Stand – set up the extrusion apparatus in a hood. Raise the platform for vertical extrusions (high enough for the depth of the bath + the length of the syringe needle) or lower it for horizontal, automated extrusions.
8) Syringe pump – Plug in and set the syringe pump on the pump stand. Set the rate (typically 0.1 mL/min) and the volume to dispense (typically set to 2 mL and manually started and stopped). The syringe inner diameter will need to be programmed if it is different from the last syringe used. The syringe inner diameter can be measured accurately enough from the outer diameter of the plunger.
9) Tweezers – at least two sets of high quality tweezers are needed.
10) CSA Microspoon – a dedicated stainless microspoon/spatula is available for CSA.
11) De-ionized water bath – a large beaker of DI water should be kept in the hood for disposal of materials. Be sure to label it.
12) Pliers – pliers are needed to change syringe needles during extrusion.

III) Extrusion
- 1) Load dispersion into syringe
  - i) Remove the plunger from the syringe, ensure the syringe needle is in place.
  - ii) Hold the syringe horizontally and the dispersion vial at an angle, both in your off hand.
  - iii) Use the dedicated CSA microspoon to transfer several scoops of dispersion into the syringe. Be careful to not allow the dispersion to flow into the syringe needle yet. The volume needed will depend on the length of extruded wire desired. Typically 0.5-1 mL is enough for 3-10 m.
  - iv) Place the CSA microspoon into the DI water bath.
  - v) Set the dispersion vial down.
  - vi) Place the syringe plunger into the opening in the syringe but to not depress it yet.

    - vii) Hold the syringe and plunger vertically with the needle pointing up. SLOWLY depress the plunger so that all air is removed and no bubbles form. BE CAREFUL NOT TO EJECT DISPERSION MATERIAL.
    - viii) When a small droplet of dispersion begins to emerge from the needle, all the air has been removed. Set the syringe down.
    - ix) **Wipe down the threads of the dispersion vial** and replace its cap.
- 2) Set up syringe and pump
    - i) Place the loaded syringe into the syringe pump and set the clamp to hold the syringe in place.
    - ii) Unlock the syringe pump pusher block, slide it up to the syringe plunger, and lock it in place.
- 3) Extrusion
    - i) Fill the coagulant bath with coagulant.
    - ii) For vertical extrusions:
        - (1) Tip the syringe pump onto its side and raise/lower the coagulant bath so that just the tip of the syringe needle is below the coagulant surface.
        - (2) Press the run button on the syringe pump. It may take a moment for dispersion to begin being ejected.
        - (3) When the desired length of wire has been extruded (usually serval times the depth of the coagulant bath, grab the top of the extruded wire with tweezers, stop the pump, and slowly remove the wire from the bath.
        - (4) Hand tension the extruded wire.
        - (5) Drape segments over the glass slides with double-sided tape. Press gently on the sections over the tape to adhere them. Cut multiple more segments, 5+ should fit on each slide.
    - iii) For Automated extrusions:
        - (1) Start the spoolers at a slow speed. The top knob controls the first spool, and the second knob controls the % elongation (at set point 0, the second spool runs the same speed as the first).
        - (2) Run the syringe pump.
        - (3) When wire begins extruding, feed it under the first spooler.
        - (4) Increase spooler speed to match extrusion rate.
        - (5) After wire has wrapped around the first spooler 2 or more times, feed it under the second spooler.
        - (6) Adjust spooler speeds for desired amounts of tension.
        - (7) When desired length of wire has been extruded, stop the syringe pump and allow the remaining wire to run over the first spooler and collect entirely on the second.
        - (8) Unwind the wire and section out onto glass slides with double-sided tape for characterization or wrap around a glass spool such as a test tube for storage.
- 4) Clean Up and Disposal:

i) Eject any remaining dispersion left in the syringe into a coagulant bath by hand until the syringe is empty.
ii) Remove the syringe needle using a pair of pliers and carefully drop it into the DI water bath.
iii) Remove the syringe plunger and carefully drop it into the DI water bath.
iv) Carefully drop the syringe body into the DI water bath with the open (plunger) end facing upwards.
v) Remove CNT solids from DI water bath using tweezers and retain for recycling.
vi) Neutralize the DI water bath.
vii) Remove and clean the syringe body and plunger. Dry them in the drying oven.
viii) Place the syringe needle into the sharps disposal.
ix) Discard the neutralized DI water bath as aqueous or inorganic waste.
x) Return all materials to their storage locations.
xi) Immediately characterize all wire segments.

Bibliography

[1] P. R. Wallace, "The Band Theory of Graphite," *Physical Review,* vol. 71, pp. 622-634, 05/01/ 1947.

[2] (2012). *Scientific Background on the Nobel Prize in Physics 2010: Graphene*. Available: http://www.nobelprize.org/nobel_prizes/physics/laureates/2010/advanced-physicsprize2010.pdf

[3] C. Thomsen, S. Reich, and J. Maultzsch, *Carbon Nanotubes: Basic Concepts and Physical Properties*: Wiley, 2004.

[4] M. Ouyang, J.-L. Huang, C. L. Cheung, and C. M. Lieber, "Energy Gaps in "Metallic" Single-Walled Carbon Nanotubes," *Science,* vol. 292, pp. 702-705, 2001.

[5] M. J. Biercuk, S. Ilani, C. M. Marcus, and P. L. McEuen, "Electrical Transport in Single-Wall Carbon Nanotubes," in *Carbon Nanotubes: Advanced Topics in the Synthesis, Structure, Properties and Applications*, A. Jorio, G. Dresselhaus, and M. S. Dresselhaus, Eds., ed Berlin, Heidelberg: Springer Berlin Heidelberg, 2008, pp. 455-493.

[6] S. J. Tans, M. H. Devoret, H. Dai, A. Thess, R. E. Smalley, L. J. Geerligs*, et al.*, "Individual single-wall carbon nanotubes as quantum wires," *Nature,* vol. 386, pp. 474-477, 04/03/print 1997.

[7] C. T. White and T. N. Todorov, "Carbon nanotubes as long ballistic conductors," *Nature,* vol. 393, pp. 240-242, 05/21/print 1998.

[8] *Handbook of Chemistry and Physics, 96th Edition*, 96 ed.: CRC Press, 2015-2016.

[9] Z. Zhang, J. Peng, and H. Zhang, "Low-temperature resistance of individual single-walled carbon nanotubes: A theoretical estimation," *Applied Physics Letters,* vol. 79, pp. 3515-3517, 2001.

[10] J. Kong, C. Zhou, A. Morpurgo, H. T. Soh, C. F. Quate, C. Marcus*, et al.*, "Synthesis, integration, and electrical properties of individual single-walled carbon nanotubes," *Applied Physics A,* vol. 69, pp. 305-308.

[11] Z. Yao, C. L. Kane, and C. Dekker, "High-Field Electrical Transport in Single-Wall Carbon Nanotubes," *Physical Review Letters,* vol. 84, pp. 2941-2944, 03/27/ 2000.

[12] B. Peng, M. Locascio, P. Zapol, S. Li, S. L. Mielke, G. C. Schatz*, et al.*, "Measurements of near-ultimate strength for multiwalled carbon nanotubes and irradiation-induced crosslinking improvements," *Nat Nano,* vol. 3, pp. 626-631, 10//print 2008.

[13] C.-H. Sun, G.-Q. Lu, and H.-M. Cheng, "Simple approach to estimating the van der Waals interaction between carbon nanotubes," *Physical Review B,* vol. 73, p. 195414, 05/17/ 2006.

[14] C.-H. Sun, L.-C. Yin, F. Li, G.-Q. Lu, and H.-M. Cheng, "Van der Waals interactions between two parallel infinitely long single-walled nanotubes," *Chemical Physics Letters,* vol. 403, pp. 343-346, 2/25/ 2005.

[15] P. Delaney, H. J. Choi, J. Ihm, S. G. Louie, and M. L. Cohen, "Broken symmetry and pseudogaps in ropes of carbon nanotubes," *Nature,* vol. 391, pp. 466-468, 01/29/print 1998.

[16] P. Delaney, H. Joon Choi, J. Ihm, S. G. Louie, and M. L. Cohen, "Broken symmetry and pseudogaps in ropes of carbon nanotubes," *Physical Review B,* vol. 60, pp. 7899-7904, 09/15/ 1999.

[17] P. G. Collins, K. Bradley, M. Ishigami, and A. Zettl, "Extreme Oxygen Sensitivity of Electronic Properties of Carbon Nanotubes," *Science,* vol. 287, pp. 1801-1804, 2000.

[18] C. Morgan, Z. Alemipour, and M. Baxendale, "Variable range hopping in oxygen-exposed single-wall carbon nanotube networks," *physica status solidi (a),* vol. 205, pp. 1394-1398, 2008.

[19] D. J. Mowbray, C. Morgan, and K. S. Thygesen, "Influence of O2 and N2 on the conductivity of carbon nanotube networks," *Physical Review B,* vol. 79, p. 195431, 05/22/ 2009.

[20] R. A. Bell, M. C. Payne, and A. A. Mostofi, "Does water dope carbon nanotubes?," *The Journal of Chemical Physics,* vol. 141, p. 164703, 2014.

[21] O. Yaglioglu, A. Cao, A. J. Hart, R. Martens, and A. H. Slocum, "Wide Range Control of Microstructure and Mechanical Properties of Carbon Nanotube Forests: A Comparison Between Fixed and Floating Catalyst CVD Techniques," *Advanced Functional Materials,* vol. 22, pp. 5028-5037, 2012.

[22] B. J. Landi and R. P. Raffaelle, "Effects of Carrier Gas Dynamics on Single Wall Carbon Nanotube Chiral Distributions During Laser Vaporization Synthesis," *Journal of Nanoscience and Nanotechnology,* vol. 7, pp. 883-890, // 2007.

[23] T. Guo, P. Nikolaev, A. Thess, D. T. Colbert, and R. E. Smalley, "Catalytic growth of single-walled manotubes by laser vaporization," *Chemical Physics Letters,* vol. 243, pp. 49-54, 9/8/ 1995.

[24] A. S. Wu, T.-W. Chou, J. W. Gillespie, D. Lashmore, and J. Rioux, "Electromechanical response and failure behaviour of aerogel-spun carbon nanotube fibres under tensile loading," *Journal of Materials Chemistry,* vol. 22, pp. 6792-6798, 2012.

[25] Y.-L. Li, I. A. Kinloch, and A. H. Windle, "Direct Spinning of Carbon Nanotube Fibers from Chemical Vapor Deposition Synthesis," *Science,* vol. 304, pp. 276-278, 2004.

[26] K. Koziol, J. Vilatela, A. Moisala, M. Motta, P. Cunniff, M. Sennett*, et al.*, "High-Performance Carbon Nanotube Fiber," *Science,* vol. 318, pp. 1892-1895, 2007.

[27] X.-H. Zhong, Y.-L. Li, Y.-K. Liu, X.-H. Qiao, Y. Feng, J. Liang*, et al.*, "Continuous Multilayered Carbon Nanotube Yarns," *Advanced Materials,* vol. 22, pp. 692-696, 2010.

[28] J. J. Vilatela and A. H. Windle, "Yarn-Like Carbon Nanotube Fibers," *Advanced Materials,* vol. 22, pp. 4959-4963, 2010.

[29] R. M. Sundaram, K. K. K. Koziol, and A. H. Windle, "Continuous Direct Spinning of Fibers of Single-Walled Carbon Nanotubes with Metallic Chirality," *Advanced Materials,* vol. 23, pp. 5064-5068, 2011.

[30] B. Alemán, V. Reguero, B. Mas, and J. J. Vilatela, "Strong Carbon Nanotube Fibers by Drawing Inspiration from Polymer Fiber Spinning," *ACS Nano,* vol. 9, pp. 7392-7398, 2015/07/28 2015.

[31] J. N. Wang, X. G. Luo, T. Wu, and Y. Chen, "High-Strength Carbon Nanotube Fibre-Like Ribbon with High Ductility and High Electrical Conductivity," *Nat. Commun.,* vol. 5, pp. 1-8, 06/25/online 2014.

[32] W. Xu, Y. Chen, H. Zhan, and J. N. Wang, "High-Strength Carbon Nanotube Film from Improving Alignment and Densification," *Nano Letters,* vol. 16, pp. 946-952, 2016/02/10 2016.

[33] D. Janas, A. C. Vilatela, and K. K. K. Koziol, "Performance of carbon nanotube wires in extreme conditions," *Carbon,* vol. 62, pp. 438-446, 10// 2013.

[34] A. Lekawa-Raus, P. Haladyj, and K. Koziol, "Carbon nanotube fiber-silver hybrid electrical conductors," *Materials Letters,* vol. 133, pp. 186-189, Oct 15 2014.

[35] A. Lekawa-Raus, K. Walczak, G. Kozlowski, S. C. Hopkins, M. Wozniak, B. A. Glowacki*, et al.*, "Low temperature electrical transport in modified carbon nanotube fibres," *Scripta Materialia,* vol. 106, pp. 34-37, Sep 2015.

[36] S. Boncel, R. M. Sundaram, A. H. Windle, and K. K. K. Koziol, "Enhancement of the Mechanical Properties of Directly Spun CNT Fibers by Chemical Treatment," *ACS Nano,* vol. 5, pp. 9339-9344, 2011/12/27 2011.

[37] M. Zhang, K. R. Atkinson, and R. H. Baughman, "Multifunctional Carbon Nanotube Yarns by Downsizing an Ancient Technology," *Science,* vol. 306, pp. 1358-1361, 2004.

[38] K. Jiang, Q. Li, and S. Fan, "Nanotechnology: Spinning continuous carbon nanotube yarns," *Nature,* vol. 419, pp. 801-801, 10/24/print 2002.

[39] K. Sears, C. Skourtis, K. Atkinson, N. Finn, and W. Humphries, "Focused ion beam milling of carbon nanotube yarns to study the relationship between structure and strength," *Carbon,* vol. 48, pp. 4450-4456, 12// 2010.

[40] Q. Zhang, D.-G. Wang, J.-Q. Huang, W.-P. Zhou, G.-H. Luo, W.-Z. Qian*, et al.*, "Dry spinning yarns from vertically aligned carbon nanotube arrays produced by an improved floating catalyst chemical vapor deposition method," *Carbon,* vol. 48, pp. 2855-2861, 8// 2010.

[41] Z. Daohong, Z. Yunhe, and M. Menghe, "Metallic conductivity transition of carbon nanotube yarns coated with silver particles," *Nanotechnology,* vol. 25, p. 275702, 2014.

[42] X. Zhang, K. Jiang, C. Feng, P. Liu, L. Zhang, J. Kong*, et al.*, "Spinning and Processing Continuous Yarns from 4-Inch Wafer Scale Super-Aligned Carbon Nanotube Arrays," *Advanced Materials,* vol. 18, pp. 1505-1510, 2006.

[43] B. Vigolo, A. Pénicaud, C. Coulon, C. Sauder, R. Pailler, C. Journet*, et al.*, "Macroscopic Fibers and Ribbons of Oriented Carbon Nanotubes," *Science,* vol. 290, pp. 1331-1334, November 17, 2000 2000.

[44] C. Mercader, A. Lucas, A. Derré, C. Zakri, S. Moisan, M. Maugey*, et al.*, "Kinetics of fiber solidification," *Proceedings of the National Academy of Sciences,* vol. 107, pp. 18331-18335, October 26, 2010 2010.

[45] C. Jiang, A. Saha, C. C. Young, D. P. Hashim, C. E. Ramirez, P. M. Ajayan*, et al.*, "Macroscopic Nanotube Fibers Spun from Single-Walled Carbon Nanotube Polyelectrolytes," *ACS Nano,* vol. 8, pp. 9107-9112, 2014/09/23 2014.

[46] S. Ramesh, L. M. Ericson, V. A. Davis, R. K. Saini, C. Kittrell, M. Pasquali*, et al.*, "Dissolution of Pristine Single Walled Carbon Nanotubes in Superacids by Direct Protonation," *The Journal of Physical Chemistry B,* vol. 108, pp. 8794-8798, 2004/07/01 2004.

[47] V. A. Davis, A. N. G. Parra-Vasquez, M. J. Green, P. K. Rai, N. Behabtu, V. Prieto*, et al.*, "True Solutions of Single-Walled Carbon Nanotubes for Assembly into Macroscopic Materials," *Nat. Nanotechnol.,* vol. 4, pp. 830-834, 12//print 2009.

[48] A. Windle, "Processing: Superacids offer nanotube solution," *Nat Nano,* vol. 4, pp. 800-801, 12//print 2009.

[49] V. A. Davis, L. M. Ericson, A. N. G. Parra-Vasquez, H. Fan, Y. Wang, V. Prieto*, et al.*, "Phase Behavior and Rheology of SWNTs in Superacids," *Macromolecules,* vol. 37, pp. 154-160, 2004/01/01 2004.

[50] F. Mirri, A. W. K. Ma, T. T. Hsu, N. Behabtu, S. L. Eichmann, C. C. Young*, et al.*, "High-Performance Carbon Nanotube Transparent Conductive Films by Scalable Dip Coating," *ACS Nano,* vol. 6, pp. 9737-9744, 2012/11/27 2012.

[51] W. Zhou, J. Vavro, C. Guthy, K. I. Winey, J. E. Fischer, L. M. Ericson*, et al.*, "Single wall carbon nanotube fibers extruded from super-acid suspensions: Preferred orientation, electrical, and thermal transport," *Journal of Applied Physics,* vol. 95, pp. 649-655, Jan 15 2004.

[52] L. M. Ericson, H. Fan, H. Peng, V. A. Davis, W. Zhou, J. Sulpizio*, et al.*, "Macroscopic, Neat, Single-Walled Carbon Nanotube Fibers," *Science,* vol. 305, pp. 1447-1450, September 3, 2004 2004.

[53] N. Behabtu, C. C. Young, D. E. Tsentalovich, O. Kleinerman, X. Wang, A. W. K. Ma*, et al.*, "Strong, Light, Multifunctional Fibers of Carbon Nanotubes with Ultrahigh Conductivity," *Science,* vol. 339, pp. 182-186, January 11, 2013 2013.

[54] G. Liu, Y. Zhao, K. Deng, Z. Liu, W. Chu, J. Chen*, et al.*, "Highly Dense and Perfectly Aligned Single-Walled Carbon Nanotubes Fabricated by Diamond Wire Drawing Dies," *Nano Letters,* vol. 8, pp. 1071-1075, 2008/04/01 2008.

[55] D. Austin, D. A. Antonella, U. Filippo, L. Simon, and G. Randall, "Biphasic DC measurement approach for enhanced measurement stability and multi-channel sampling of self-sensing multi-functional structural materials doped with carbon-based additives," *Smart Materials and Structures,* vol. 26, p. 065008, 2017.

[56] L. van der Pauw, "A method of measuring specific resistivity and Hall effect of discs of arbitrary shape," *Philips Res. Rep.,* vol. 13, pp. 1-9, 1958.

[57] L. van der Pauw, "A method of measuring the resistivity and Hall coefficient on lamellae of arbitrary shape," *Philips technical review,* vol. 20, pp. 220-224, 1958.

[58] E. Mansfield, A. Kar, and S. A. Hooker, "Applications of TGA in quality control of SWCNTs," *Analytical and Bioanalytical Chemistry,* vol. 396, pp. 1071-1077, 2010/02/01 2010.

[59] E. Mansfield, A. Kar, C. M. Wang, and A. N. Chiaramonti, "Statistical sampling of carbon nanotube populations by thermogravimetric analysis," *Analytical and Bioanalytical Chemistry,* vol. 405, pp. 8207-8213, 2013/10/01 2013.

[60] W. Zhou, S. Xie, L. Sun, D. Tang, Y. Li, Z. Liu*, et al.*, "Raman scattering and thermogravimetric analysis of iodine-doped multiwall carbon nanotubes," *Applied Physics Letters,* vol. 80, pp. 2553-2555, 2002/04/08 2002.

[61] S. Bandow, S. Asaka, Y. Saito, A. M. Rao, L. Grigorian, E. Richter*, et al.*, "Effect of the Growth Temperature on the Diameter Distribution and Chirality of Single-Wall Carbon Nanotubes," *Physical Review Letters,* vol. 80, pp. 3779-3782, 04/27/ 1998.

[62] A. M. Rao, E. Richter, S. Bandow, B. Chase, P. C. Eklund, K. A. Williams*, et al.*, "Diameter-Selective Raman Scattering from Vibrational Modes in Carbon Nanotubes," *Science,* vol. 275, p. 187, 1997.

[63] M. S. Dresselhaus, G. Dresselhaus, R. Saito, and A. Jorio, "Raman spectroscopy of carbon nanotubes," *Physics Reports,* vol. 409, pp. 47-99, 2005/03/01/ 2005.

[64] S. D. M. Brown, A. Jorio, P. Corio, M. S. Dresselhaus, G. Dresselhaus, R. Saito*, et al.*, "Origin of the Breit-Wigner-Fano lineshape of the tangential G-band feature of metallic carbon nanotubes," *Physical Review B,* vol. 63, p. 155414, 03/29/ 2001.

[65] A. M. Rao, P. C. Eklund, S. Bandow, A. Thess, and R. E. Smalley, "Evidence for charge transfer in doped carbon nanotube bundles from Raman scattering," *Nature,* vol. 388, pp. 257-259, 07/17/print 1997.

[66] J. E. Rossi, C. D. Cress, A. Merrill, K. J. Soule, N. D. Cox, and B. J. Landi, "Intrinsic diameter dependent degradation of single-wall carbon nanotubes from ion irradiation," *Carbon,* vol. 81, pp. 488-496, 2015/01/01/ 2015.

[67] B. J. Landi, C. D. Cress, C. M. Evans, and R. P. Raffaelle, "Thermal Oxidation Profiling of Single-Walled Carbon Nanotubes," *Chem. Mater.,* vol. 17, pp. 6819-6834, 2005/12/01 2005.

[68] B. J. Landi, H. J. Ruf, C. M. Evans, C. D. Cress, and R. P. Raffaelle, "Purity Assessment of Single-Wall Carbon Nanotubes, Using Optical Absorption Spectroscopy," *J. Phys. Chem. B,* vol. 109, pp. 9952-9965, 2005/05/01 2005.

[69] P. Jarosz, C. Schauerman, J. Alvarenga, B. Moses, T. Mastrangelo, R. Raffaelle*, et al.*, "Carbon Nanotube Wires and Cables: Near-Term Applications and Future Perspectives," *Nanoscale,* vol. 3, pp. 4542-4553, 2011.

[70] C. M. Schauerman, J. Alvarenga, B. J. Landi, C. D. Cress, and R. P. Raffaelle, "Impact of Nanometal Catalysts on the Laser Vaporization Synthesis of Single Wall Carbon Nanotubes," *Carbon,* vol. 47, pp. 2431-2435, 8// 2009.

[71] B. J. Landi, H. J. Ruf, C. M. Evans, C. D. Cress, and R. P. Raffaelle, "Purity Assessment of Single-Wall Carbon Nanotubes, Using Optical Absorption Spectroscopy," *The Journal of Physical Chemistry B,* vol. 109, pp. 9952-9965, 2005/05/01 2005.

[72] B. J. Landi, C. D. Cress, C. M. Evans, and R. P. Raffaelle, "Thermal Oxidation Profiling of Single-Walled Carbon Nanotubes," *Chemistry of Materials,* vol. 17, pp. 6819-6834, 2005/12/01 2005.

[73] V. A. Davis, A. N. G. Parra-Vasquez, M. J. Green, P. K. Rai, N. Behabtu, V. Prieto*, et al.*, "True solutions of single-walled carbon nanotubes for assembly into macroscopic materials," *Nat Nano,* vol. 4, pp. 830-834, 12//print 2009.

[74] S. Frank, P. Poncharal, Z. L. Wang, and W. A. d. Heer, "Carbon Nanotube Quantum Resistors," *Science,* vol. 280, p. 1744, 1998.

[75] S. J. Tans, M. H. Devoret, H. Dai, A. Thess, R. E. Smalley, L. J. Geerligs*, et al.*, "Individual single-wall carbon nanotubes as quantum wires," *Nature,* vol. 386, p. 474, 04/03/online 1997.

[76] G. F. Moore, "Electric Cables Handbook (3rd Edition)," ed: John Wiley & Sons, p. 121.

[77] A. Mertol, "Estimation of aluminum and gold bond wire fusing current and fusing time," *IEEE Transactions on Components, Packaging, and Manufacturing Technology: Part B,* vol. 18, pp. 210-214, 1995.

[78] E. Loh, "Physical Analysis of Data on Fused-Open Bond Wires," *IEEE Transactions on Components, Hybrids, and Manufacturing Technology,* vol. 6, pp. 209-217, 1983.

[79] P. G. Collins, M. Hersam, M. Arnold, R. Martel, and P. Avouris, "Current Saturation and Electrical Breakdown in Multiwalled Carbon Nanotubes," *Physical Review Letters,* vol. 86, pp. 3128-3131, 04/02/ 2001.

[80] P. Jin Gyu, L. Shu, L. Richard, F. Xinyu, Z. Chuck, and W. Ben, "The high current-carrying capacity of various carbon nanotube-based buckypapers," *Nanotechnology,* vol. 19, p. 185710, 2008.

[81] G. Man Prakash, B. Ashkan, L. Feifei, E. David, P. Eric, and K. Satish, "High field breakdown characteristics of carbon nanotube thin film transistors," *Nanotechnology,* vol. 24, p. 405204, 2013.

[82] S. Li, T. Geza, W. Jinquan, L. Zheng, G. Wei, C. Lijie*, et al.*, "Sharp burnout failure observed in high current-carrying double-walled carbon nanotube fibers," *Nanotechnology,* vol. 23, p. 015703, 2012.

[83] X. Wang, N. Behabtu, C. C. Young, D. E. Tsentalovich, M. Pasquali, and J. Kono, "High-Ampacity Power Cables of Tightly-Packed and Aligned Carbon Nanotubes," *Advanced Functional Materials,* vol. 24, pp. 3241-3249, 2014.

[84] C. D. Cress, M. J. Ganter, C. M. Schauerman, K. Soule, J. E. Rossi, C. C. Lawlor*, et al.*, "Carbon nanotube wires with continuous current rating exceeding 20 Amperes," *Journal of Applied Physics,* vol. 122, p. 025101, 2017/07/14 2017.

[85] R. J. Naumann, *Introduction to the Physics and Chemistry of Materials*: CRC Press, 2009.

[86] "Standard Test Method for Tensile Strength and Young’s Modulus of Fibers," ed.

[87] "Standard Test Method for Tensile Properties of Plastics," ed.

[88] "Standard Test Method for Tensile Properties of Polymer Matrix Composite Materials," ed.

[89] "Standard Test Method for Tensile Properties of Single Textile Fibers," ed.

[90] A. Mahajan, A. Kingon, Á. Kukovecz, Z. Konya, and P. M. Vilarinho, "Studies on the thermal decomposition of multiwall carbon nanotubes under different atmospheres," *Materials Letters,* vol. 90, pp. 165-168, 2013/01/01/ 2013.

[91] R. A. DiLeo, B. J. Landi, and R. P. Raffaelle, "Purity assessment of multiwalled carbon nanotubes by Raman spectroscopy," *Journal of Applied Physics,* vol. 101, p. 064307, 2007/03/15 2007.

[92] A. Lekawa-Raus, L. Kurzepa, X. Y. Peng, and K. Koziol, "Towards the development of carbon nanotube based wires," *Carbon,* vol. 68, pp. 597-609, Mar 2014.

[93] A. R. Bucossi, C. D. Cress, C. M. Schauerman, J. E. Rossi, I. Puchades, and B. J. Landi, "Enhanced Electrical Conductivity in Extruded Single-Wall Carbon Nanotube Wires from Modified Coagulation Parameters and Mechanical Processing," *ACS Applied Materials & Interfaces,* vol. 7, pp. 27299-27305, 2015/12/16 2015.

[94] R. S. Lee, H. J. Kim, J. E. Fischer, A. Thess, and R. E. Smalley, "Conductivity enhancement in single-walled carbon nanotube bundles doped with K and Br," *Nature,* vol. 388, pp. 255-257, 07/17/print 1997.

[95] L. Duclaux, "Review of the doping of carbon nanotubes (multiwalled and single-walled)," *Carbon,* vol. 40, pp. 1751-1764, 8// 2002.

[96] Y. Zhao, J. Wei, R. Vajtai, P. M. Ajayan, and E. V. Barrera, "Iodine Doped Carbon Nanotube Cables Exceeding Specific Electrical Conductivity of Metals," *Sci. Rep.,* vol. 1, pp. 1-5, 09/06/online 2011.

[97] I. Puchades, C. C. Lawlor, C. M. Schauerman, A. R. Bucossi, J. E. Rossi, N. D. Cox*, et al.*, "Mechanism of chemical doping in electronic-type-separated single wall carbon nanotubes towards high electrical conductivity," *Journal of Materials Chemistry C,* vol. 3, pp. 10256-10266, 2015.

[98] J. Alvarenga, P. R. Jarosz, C. M. Schauerman, B. T. Moses, B. J. Landi, C. D. Cress*, et al.*, "High Conductivity Carbon Nanotube Wires From Radial Densification and Ionic Doping," *Appl. Phys. Lett.,* vol. 97, p. 182106, 2010.

[99] D. Janas, A. P. Herman, S. Boncel, and K. K. K. Koziol, "Iodine monochloride as a powerful enhancer of electrical conductivity of carbon nanotube wires," *Carbon,* vol. 73, pp. 225-233, 7// 2014.

[100] D. Janas, K. Z. Milowska, P. D. Bristowe, and K. K. K. Koziol, "Improving the electrical properties of carbon nanotubes with interhalogen compounds," *Nanoscale,* vol. 9, pp. 3212-3221, 2017.

[101] J. E. Fischer, "Chemical Doping of Single-Wall Carbon Nanotubes," *Accounts of Chemical Research,* vol. 35, pp. 1079-1086, 2002/12/01 2002.

[102] T. M. Barnes, J. L. Blackburn, J. van de Lagemaat, T. J. Coutts, and M. J. Heben, "Reversibility, Dopant Desorption, and Tunneling in the Temperature-Dependent Conductivity of Type-Separated, Conductive Carbon Nanotube Networks," *ACS Nano,* vol. 2, pp. 1968-1976, 2008/09/23 2008.

[103] J. L. Blackburn, T. M. Barnes, M. C. Beard, Y.-H. Kim, R. C. Tenent, T. J. McDonald*, et al.*, "Transparent Conductive Single-Walled Carbon Nanotube Networks with Precisely Tunable Ratios of Semiconducting and Metallic Nanotubes," *ACS Nano,* vol. 2, pp. 1266-1274, 2008/06/01 2008.

[104] P. N. Nirmalraj, P. E. Lyons, S. De, J. N. Coleman, and J. J. Boland, "Electrical Connectivity in Single-Walled Carbon Nanotube Networks," *Nano Letters,* vol. 9, pp. 3890-3895, 2009/11/11 2009.

[105] R. E. Rogers, T. I. Bardsley, S. J. Weinstein, and B. J. Landi, "Solution-phase adsorption of 1-pyrenebutyric acid using single-wall carbon nanotubes," *Chemical Engineering Journal,* vol. 173, pp. 486-493, 9/15/ 2011.

[106] M. Afrooz and H. Dehghani, "Effects of triphenyl phosphate as an inexpensive additive on the photovoltaic performance of dye-sensitized nanocrystalline TiO2 solar cells," *RSC Advances,* vol. 5, pp. 50483-50493, 2015.

[107] N. Middendorf, K. Krause, and S. Höfener, "Solvatochromic shifts of Br2 and I2 in water cages of type 512, 51262, 51263, and 51264," *Journal of Computational Chemistry,* vol. 36, pp. 853-860, 2015.

[108] P. Wei, D. Zhang, Z. Gao, W. Cai, W. Xu, L. Tang*, et al.*, "Iodine Monochloride (ICl) as a Highly Efficient, Green Oxidant for the Oxidation of Alcohols to Corresponding Carbonyl Compounds," *Synthetic Communications,* vol. 45, pp. 1457-1470, 2015/06/18 2015.

[109] M. I. Bernal-Uruchurtu, G. Kerenskaya, and K. C. Janda, "Structure, spectroscopy and dynamics of halogen molecules interacting with water," *International Reviews in Physical Chemistry,* vol. 28, pp. 223-265, 2009/04/01 2009.

[110] P. Suppan, "Invited review solvatochromic shifts: The influence of the medium on the energy of electronic states," *Journal of Photochemistry and Photobiology A: Chemistry,* vol. 50, pp. 293-330, 1990/01/01 1990.

[111] B. J. Landi, H. J. Ruf, J. J. Worman, and R. P. Raffaelle, "Effects of Alkyl Amide Solvents on the Dispersion of Single-Wall Carbon Nanotubes," *The Journal of Physical Chemistry B,* vol. 108, pp. 17089-17095, 2004/11/01 2004.

[112] G. Zhong, J. H. Warner, M. Fouquet, A. W. Robertson, B. Chen, and J. Robertson, "Growth of Ultrahigh Density Single-Walled Carbon Nanotube Forests by Improved Catalyst Design," *ACS Nano,* vol. 6, pp. 2893-2903, 2012/04/24 2012.

[113] D. N. Futaba, K. Hata, T. Yamada, T. Hiraoka, Y. Hayamizu, Y. Kakudate*, et al.*, "Shape-engineerable and highly densely packed single-walled carbon nanotubes and their application as super-capacitor electrodes," *Nature Materials,* vol. 5, p. 987, 11/26/online 2006.

[114] Z. Liu, N. Bajwa, L. Ci, S. H. Lee, S. Kar, P. M. Ajayan*, et al.*, "Densification of Carbon Nanotube Bundles for Interconnect Application," in *2007 IEEE International Interconnect Technology Conferencee*, 2007, pp. 201-203.

[115] B. A. Kakade and V. K. Pillai, "Tuning the Wetting Properties of Multiwalled Carbon Nanotubes by Surface Functionalization," *The Journal of Physical Chemistry C,* vol. 112, pp. 3183-3186, 2008/03/01 2008.

[116] M. Zdrojek, W. Gebicki, C. Jastrzebski, T. Melin, and A. Huczko, "Studies of Multiwall Carbon Nanotubes Using Raman Spectroscopy and Atomic Force Microscopy," *Solid State Phenomena,* vol. 99-100, pp. 265-268, 2004.

[117] N. Hiroyuki, S. Yoshiyuki, N. Hamazo, and K. Atsuhiro, "Influence of Diameter on the Raman Spectra of Multi-Walled Carbon Nanotubes," *Applied Physics Express,* vol. 1, p. 064005, 2008.

[118] A. Congeduti, M. Nardone, and P. Postorino, "Polarized Raman spectra of a single crystal of iodine," *Chemical Physics,* vol. 256, pp. 117-123, 2000/05/15/ 2000.

[119] (2017). *CRC Handbook of Chemistry and Physics (97 ed.)*.

[120] C. W. Padgett and D. W. Brenner, "Influence of Chemisorption on the Thermal Conductivity of Single-Wall Carbon Nanotubes," *Nano Letters,* vol. 4, pp. 1051-1053, 2004/06/01 2004.

[121] W. Yu, L. Wang, Y. Qi, L. Chen, L. Wang, and H. Xie, "The influence of nitrogen doping on thermal conductivity of carbon nanotubes," *Thermochimica Acta,* vol. 617, pp. 163-168, 2015/10/10/ 2015.

[122] E. Brown, L. Hao, J. C. Gallop, J. C. Macfarlane, P. W. Josephs-Franks, and L. F. Cohen, "The effect of molecular oxygen on the thermal conductance of multi-walled nanotubes – a preliminary investigation," *physica status solidi (b),* vol. 243, pp. 3380-3384, 2006.

[123] M. Yarali, J. Hao, M. Khodadadi, H. Brahmi, S. Chen, V. G. Hadjiev*, et al.*, "Physisorbed versus chemisorbed oxygen effect on thermoelectric properties of highly organized single walled carbon nanotube nanofilms," *RSC Advances,* vol. 7, pp. 14078-14087, 2017.

[124] J. Alvarenga, P. R. Jarosz, C. M. Schauerman, B. T. Moses, B. J. Landi, C. D. Cress*, et al.*, "High conductivity carbon nanotube wires from radial densification and ionic doping," *Applied Physics Letters,* vol. 97, p. 182106, 2010.